COO-3130TB-248

Hadron-Deuteron Scattering at 50 GeV

by

Lorne Joel Levinson
B.Sc.(Hons), University of Manitoba, 1970

Thesis
submitted in partial fulfillment of the requirements for the
Degree of Doctor of Philosophy in the Department of
Physics at Brown University

June, 1978

DISCLAIMER

This dissertation by Lorne Joel Levinson

is accepted in its present form by the Department of

Physics as satisfying the

dissertation requirement for the degree of Doctor of Philosophy.

Date 12 May 1978

Recommended to the Graduate Council

Date 12. May. 1978

Date 15 May 1978 Donald R. Mason

Approved by the Graduate Council

Date . . . .

VITA

Lorne Joel Levinson was [redacted] He received his Bachelors Degree of Science in Physics from the University of Manitoba in May 1970 and entered the Graduate School of Brown University in September 1970.

ABSTRACT

Abstract of 'Hadron-Deuteron Scattering at 50 GeV'

by Lorne Joel Levinson, Ph. D., Brown University, June 1978

The forward scattering of π^+, π^-, and protons on deuterons and protons was measured with a single arm spectrometer at the Fermi National Accelerator Laboratory. The energy was 50 GeV and the invariant 4-momentum transfer range was $.06 < |t| < .32$ $(\mathrm{GeV}/c)^2$ for π^+ and p, and $.06 < |t| < .50$ for π^-. The missing mass, determined by the spectrometer, selected proton elastic and deuteron elastic-plus-breakup scattering, rejecting particle and resonance production events. The measured proton and deuteron differential cross-sections were analysed in the context of the Glauber Theory of deuteron elastic-plus-breakup scattering and a neutron elastic differential cross-section was extracted. The theory and analysis were tested by comparing the π^+n cross-section extracted from the π^+d and π^+p data with the π^-p data; by I-spin symmetry the π^+n cross-section must equal the π^-p. The same test was done for π^-n. The proton-neutron elastic differential cross-section was then extracted from the pd and pp data. The theory and the data were not found to be consistent within the random errors. Systematic errors are probably the cause; several possible systematic errors are discussed. The thesis also reports an attempt to use recoil particle detectors to extract the deuteron elastic and the neutron cross-sections.

Someone saw Nasrudin searching on the ground.

'What have you lost Mulla?' he asked. 'My key', said the Mulla. So they both went down on their knees and looked for it.

After a time the other man asked: 'where exactly did you drop it?'

'In my own house.'

'Then why are you looking here?'

'There is more light here than inside my own house.'

a Sufi story

ACKNOWLEDGEMENTS

Writing this thesis has been a time to pause and reflect over the previous years and appreciate those people who have enriched my carreer in Physics and my life.

The experiment described in this thesis was performed by a large collaboration. I thank all of them for their efforts on the experiment and for helping to make my 2 1/2 years at Fermilab exhilarating and enriching. I particularily thank those with whom I worked closest -- Joel Butler, Dave Gustavson, Robin Verdier, Bruce Nelson, Bernie Gittelman, Keith Rich, and Jim Fines -- for their good natures and hard work. Dave Ritson worked very hard as spokesman for the experiment; the many discussions with him, at all times of day and night, were always lively and illuminating. The companionship of Joel Butler helped make those many days building and running the experiment both enjoyable and fruitful. Mike Sogard was especially helpful in orienting me in the extensive literature on deuteron scattering theory. Bernie Gottshalk's description of his recoil detector system laid the foundations for my recoil particle studies.

I Thank the staff of the Fermi National Accelerator Laboratory, especially the Meson Lab, for their efforts in constructing and running the acclerator, beamline, and spectrometer.

At Brown University I have had numerous useful discussions with Jan Greben, Stavros Fallieros, and Dave Peaslee. An afternoon discussion with Victor Franco at Brooklyn College helped to clarify the role of the Multiple Scattering Theory when the recoil particle is detected.

The many lively discussions with Stuart Kasdan, Hashim Rizvi, Neal Snyderman, and Ron Thornton, my friends and High Energy Physics student colleagues, will always be remembered.

Special appreciation is due to Stuart Kasdan, Hashim Rizvi, Tom and Carrol Randall, Mark Passler, Steven DelSesto and Philippa Adelstein for their sincere friendship, many good times, and clear sight.

I sincerely appreciate and thank my thesis advisor, Robert Lanou, for his unfailing support, encouragement and faith in me. He has made these years, years of real personal and professional growth.

Dave Cutts and Joe Massimo have been friends, colleagues, and advisors. Their advice and suggestions, especially on the data analysis and on online computing, has been of considerable help. The company of Bob Dulude has made the data analysis stage of the thesis much more enjoyable.

I deeply thank my parents for their love and encouragement.

The continued financial support throughout my graduate carreer by the U.S. Department of Energy, contract (EY-76-C-02-3130TB), is gratefully acknowledged.

Dedicated to

Sydney Caminetsky, M.D.

compassionate, strong, and

always curious

TABLE OF CONTENTS

Appendix page

LIST OF TABLES

LIST OF FIGURES

Chapter I

INTRODUCTION

1.1 THEORETICAL AND EXPERIMENTAL PERSPECTIVE

An experiment was done in the Meson Laboratory at the Fermi National Accelerator Laboratory. The forward scattering of $\pi^{\pm}$, $k^{\pm}$, p, and $\bar{p}$ on protons at energies from 50 to 175 GeV and on deuterons at 50 and 140 GeV were measured with a single arm spectrometer. This thesis describes the experiment and reports on the analysis of π^+, π^-, and p forward scattering at 50 GeV on deuterons (and protons) over the invariant 4-momentum transfer range $.05 < |t| < .5$ for π^- and $.06 < |t| < .33$ for π^+ and p. The single arm spectrometer detected the forward scattered particle and determined the missing mass of the reaction, which was used to select elastic scattering from the proton target and elastic and breakup scattering from the deuterium target. This thesis does not include inelastic, i.e. particle or resonance production reactions.

High energy scattering of hadrons from deuterons is interesting from several points of view.

1) The role of I-spin in hadron interaction dynamics is believed to become less important as the energy increases. The comparison of proton-proton and neutron-proton interactions at high energy is therefore of interest. Experiments with neutron beams can, of

course, be done. At present no neutron beam experiment has been reported that measures the forward differential cross-section at this or higher energies. A deuterium target is the next best thing to a neutron target and also allows for the study of pion, kaon, and anti-proton reactions as well as proton-neutron reactions. The small binding energy of the nucleons in the deuteron means they are almost free nucleons. A fast beam with a wavelength much less than the deuteron radius can be considered to interact with only one of the nucleons. One can attempt, therefore, to extract hadron interactions with a <u>free</u> nucleon from deuterium and proton target scattering measurements. This is the main concern of this thesis.

2) The deuteron has I-spin = 0. If the deuteron remains in the final state, the other final state particles must be in a state with total I-spin equal to the incident particle. This allows the study of particular I-spin states, such as resonances or dissociation of the incident particle without its I-spin changing. Also for elastic deuteron scattering, in a Regge exchange picture, only I=0 Regge trajectories can be exchanged.

3) Nuclear targets are often used in High Energy Physics. The deuteron is the simplest compound nucleus and therefore understanding high energy deuteron interactions is a first step to understanding high energy hadron-nucleus interactions.

4) If the incident hadron scatters inelasticly from one constituent nucleon of the deuteron, the other nucleon may sometimes interact with the produced particles or resonance. These

'inelastic rescattering processes' probe the hadronic interaction process at short times.

The first theoretical model of scattering from deuterons is the impulse approximation. The constituent nucleons are assumed to be at rest and the scattering is by one or the other of the nucleons. Due to their confinement by the nuclear force, the nucleons are not at rest, but have a 'Fermi momentum' -- typically 50 MeV/c but with a tail extending to a few hundred MeV/c. West [1974, and Atwood 1973] has studied the effect of the 'Doppler shift' due to this Fermi momentum.

The theoretical model of deuteron scattering has evolved since 1955 when Glauber explained [Glauber 1955] why the deuteron total cross-section was less than the sum of the neutron and proton total cross-sections. Since then those basic theoretical ideas have served to describe hadron diffractive scattering by deuterons amazingly well. In fact, refinements such as correcting for inelastic screening and meson currents have often led to worse agreement with experiment.

Franco & Glauber, Harrington, and others (see Chapter 4) have evolved a theory -- the Multiple Scattering Theory or Glauber Theory -- that gives the differential cross-sections on deuterium in terms of the free nucleon differential cross-sections and the deuteron structure as summarized by its form factor. The theory gives the cross-section in terms of a single scattering amplitude, a double scattering amplitude, and their interference. In the context of this theory one can extract the free neutron cross-section from the measured deuteron and proton cross-sections and the deuteron form factor as calculated from a 'realistic' potential model[1].

The Multiple Scattering Theory yields results for elastic deuteron scattering and for breakup (also called quasi-elastic) scattering. In breakup reactions the deuteron is dissociated into neutron and proton but there is no resonance or particle production. The scatters from the constituent nucleons are assumed to be elastic scatters. This thesis is primarily concerned with the sum of the two processes, which in this range of momentum transfer is mainly breakup scattering. Investigating the sum has the advantage that no information about the recoil state (other than the absence of particle or resonance producton) is needed.

The Multiple Scatering Theory and our analysis system can be tested using I-spin symmetry and the positive and negative charged pions. By I-spin symmetry the differential elastic cross-sections for π^+n must equal π^-p and π^-n equal π^+p. [See Appendix A.] So the π^+n cross-section extracted from the π^+d and π^+p data can be compared with the π^-p data to which it must be equal. Similarly for the π^-n cross-section. A clear advantage of our experiment is that all four reactions $\pi^\pm d$ and $\pi^\pm p$, were

---

[1] The deuteron structure, e.g. form factor, is better investigated with electrons, where the interaction is known and the probing particles pointlike. Such investigations confirm fairly well the features of the form factor predicted by the 'realistic' (i.e. sophisticated) nuclear potential models.

measured with the same apparatus. Also in this experiment data is collected simultaneously for pions, kaons, and protons of one charge. Hence the extracted pn cross-section can be relied upon to the extent that the extracted π^+n cross-section agrees with the π^-p data. It is hoped that the $k^\pm d$ and pd data at 50 GeV and all particles at 140 GeV will be similarily analyzed.

A review of high energy deuteron scattering, theory and experiment, before 1973 is given in Kolybasov [1973]. Sidhu and Quigg [1973] review pion deuteron <u>elastic</u> scattering. Typical previous experiments have included:

1) proton deuteron elastic scattering at 50 to 400 GeV from a gas jet target for $t<.14$ GeV^2/c^2 by analysis of the recoil particles. [Akimov et al. 1975]

2) π^-d and pd elastic scattering from 10 to 16 GeV for $.2 < |t| < 2.4$ using counter and spark chambers. The elastic events were separated from the breakup double scattering events by using angular correlations of the forward and recoil particles. [Bradamante et al. 1971,1972]

3) pd breakup scattering at 19.2 GeV. [Allaby et al. 1969] This experiment was primarily concerned with the momentum loss spectrum of the forward particle as a means of separating breakup single from double scattering. It was an extension of the work done by Belletini et al. [1965] on pd breakup plus elastic scattering for $|t| < .2$, who also extracted the real part of the neutron scattering amplitude.

4) pd breakup scattering at 24 GeV has been studied by Amaldi et al. [1972] over the range .1 < |t| < 5.8 using a single arm spectrometer. They extracted a neutron cross-section and were also able to measure pd elastic scattering for .6 < |t| < 1.8 with the use of an additional recoil spectrometer.

5) Braun et al. have done an anti-proton deuterium bubble chamber experiment and extracted the pn cross-section from both elastic and breakup reactions.

This experiment reported in this thesis is unique in having both π^+ and π^- scattering to test the theory and the neutron extraction procedure for breakup reactions, as well as having proton, anti-proton, and kaon scattering on which to apply it.

1.2 THE SINGLE ARM SPECTROMETER GROUP COLLABORATION

The data analyzed in this thesis was part of the first experiment performed at the FNAL Single Arm Spectrometer and M6E beamline. This experiment included the design, construction, and checkout of the beamline, spectrometer, wire chambers, several Cerenkov counters, and extensive online computer software. The elastic scattering of pions, kaons, protons, and anti-protons on hydrogen has been reported in the literature [SAS Group 1977]. The members of the collaboration are:

D.S. Ayres, R. Diebold, and G.J. Maclay
Argonne National Laboratory

D. Cutts, R.E. Lanou, Jr., L.J. Levinson, and J.T. Massimo
Brown University

J. Litt and R. Meunier
CERN

M. Sogard, B. Gittelman, and E.C. Loh
Laboratory of Nuclear Studies, Cornell University

A.E. Brenner, J.E. Elias, and G. Mikenberg
Fermi National Accelerator Laboratory

L. Guerriero, P. Lavopa, G. Maggi, C. DeMarzo,
F. Posa, G. Selvaggi, P. Spinelli, and F. Waldner
Instituto Nazionale di Fisica Nucleare, Sezione di Bari

D.S. Barton, J.N. Butler, J. Fines, J.I. Friedman,
H.W. Kendall, B. Nelson, L. Rosenson, and R. Verdier
Laboratory for Nuclear Science, Massachusetts Institute of Technology

B. Gottschalk
Northeastern University

R.L. Anderson, D. Gustavson, K. Rich, D.M. Ritson, and G.A. Weitsch
Stanford Linear Accelerator Center

1.3 PLAN OF THE THESIS

Chapter 2 of this thesis describes the experimental apparatus: the beam and spectrometer optics, the detectors, the Cerenkov counters, the electronics and the online computer.

Chapter 3 describes the trajectory reconstruction, the calculation of the kinematic variables, and the calculation of the proton and deuteron cross-sections, their errors and corrections.

Chapter 4 sketches the Multiple Scattering Theory and discusses some of its features including the form of the cross-section, the momentum loss spectrum of the forward particle, the effects of the deuteron spin, and the role of the form factor. The section on the deuteron spin presents a simple, but none-the-less new result concerning the proper form factor to be used in the breakup-plus-elastic scattering case.

Chapter 5 details the method of extracting the neutron cross-section.

Chapter 6 presents the neutron, proton, and deuteron differential cross-sections for π^+, π^-, and p at 50 GeV and discusses the comparison of these results to those expected from I-spin invariance.

Appendix B reports an attempt to use the recoil particle detectors to separate elastic deuteron scattering from deuteron breakup scattering, and an alternate method of extracting the neutron cross-section by identifying proton spectator events.

1.4 KINEMATIC NOTATION

The reactions are described in terms of the relativisticly invariant kinematical variables M^2 and t, the missing mass and the 4-momentum transfer. For P_1 the incident particle 4-momentum, P_2 the target 4-momentum, P_3 the forward scattered particle 4-momentum , and P_4 the recoiling system 4-momentum

$$t = (P_1 - P_3)^2$$

$$M^2 = P_4{}^2 = (P_1 + P_2 - P_3)^2$$

Then for a target at rest and $E_1 \gg m_1$ and $E_3 \gg m_3$

$$\begin{aligned} M^2 &= (P_1 - P_3)^2 + m_2{}^2 + P_2(P_1 - P_3) \\ &= t + m_2{}^2 + 2m_2(E_1 - E_3) \\ &= -|t| + m_2{}^2 + 2m_2(P_1 - P_3) \end{aligned}$$

where P_1 and P_3 are now the 3-momentum magnitudes.

For elastic scattering, energy conservation implies the recoil kinetic energy is

$$T = E_1 - E_3 = |t|/2m_2$$

We calculate t for small angle, high energy elastic scattering as follows, for $m_2 = m_4 = m$:

$$t = (P_1 - P_3)^2$$

$$= m^2 + m^2 - 2E_1 E_3 + 2\vec{P}_1 \bullet \vec{P}_3$$

for $E^2 = P^2 + m^2 = P^2 (1 + m^2/P^2)$

$$t = 2m^2 - 2P_1 P_3 \left[\left(1 + \frac{m^2}{P_1^2}\right)^{1/2} \left(1 + \frac{m^2}{P_3^2}\right)^{1/2} - \cos\theta \right]$$

for $m << P$

$$t = 2m^2 - 2P_1 P_3 \left[\left(1 + \frac{1}{2}\frac{m^2}{P_1^2}\right) \left(1 + \frac{m^2}{2P_3^2}\right) - \cos\theta \right]$$

$$= -2P_1 P_3 (1 - \cos\theta) + m^2 (2 - P_1/P_3 - P_3/P_1)$$

$P_1 - P_3$ is small for small angle scattering, $= |t|/2m$ for elastic scattering, so the second term is very small. Also for small angles $\cos\theta = 1 + \theta^2/2$ So

$$t = -P_1 P_3 \theta^2$$

Chapter II

APPARATUS

The next section discusses general features and principles of the apparatus as a whole. Subsequent sections briefly detail the specific components. More detailed descriptions can be found in Butler [1975: ch.3] and in references mentioned below. The trajectory detectors and event reconstruction are discussed in the next chapter.

2.1 GENERAL FEATURES

To measure hadron elastic scattering cross-sections at high energy by measurements on the scattered hadron, one needs high momentum resolution in order to reject the inelastic events. This can be seen as follows: The threshold for inelastic processes is the production of one pion at rest in the laboratory. This process is separated in missing mass from elastic scattering by

$$\Delta M^2 = (m_p + m_\pi)^2 - m_p^2 = 2m_p m_\pi + m_\pi^2 \tag{1}$$

In this experiment we calculate M^2 by measuring the scattered momentum, P_3, (and scattering angle)

$$M^2 = (P_1 + P_2 - P_3)^2 = t + m_p^2 + 2m_p(P_1 - P_3) \tag{2}$$

$$\text{so,} \quad \Delta M^2 = 2m_p \Delta P_3 \tag{3}$$

(ignoring the dependence of t on P_3.)

Therefore the momentum resolution needed is atleast

$$\Delta P_3 = M^2/2m_\rho = m_\pi(1 + m_\pi/2m_\rho) = 150 \text{ MeV/c} \qquad (4)$$

or, at 50 GeV/c, $\Delta P/P = .3\%$. In fact we would like a resolution several times better.

But in order to have a reasonable number of particles to do an experiment we must accept particles in a momentum band much larger than .3%. This means the <u>beam</u> particles must have their momentum measured so that we can measure the difference, P -P , to atleast .3%. This requires a multi-stage beam transport system to collect and collimate the beam, disperse it for momentum tagging, and recombine the momenta at the target.

At high energy, moderate 4-momentum transfer, t, occurs at quite small angles. Using $t=-P_1P_3\theta^2$, $P_1-P_3 = |t|/2m$ and $P_1 = 50$ GeV/c, we find $t = .06$ at $\theta = 5$ mr. and $t = .6$ at $\theta = 15$ mr. Two consequences of this for the apparatus are:

a) The divergence of the beam at the target is .2 to .3 mr. To get good t resolution, especially at small t, we must therefore measure the incomming trajectory's angles as well as the scattered trajectory's so that the scattering angle given by their difference is accurately determined. For this purpose we have two sets of crossed hodoscopes in the beam, just before the target, to measure the incident angles for each event.

b) For such small scattering angles it was possible to fix the spectrometer axis along the beam axis and vary the scattering angle by bending the beam with magnets placed before the target. The angle was varied in the vertical plane. See figure 3.

Both the incident and scattered particles were identified as protons, kaons, or pions by Cerenkov detectors in the beam and spectrometer. This enabled data for all nine beam-spectrometer combinations of the three particles to be collected simultaneously. Comparison between the particle cross-sections could then be done with minimal systematic errors. One of the Cerenkov counters in the spectrometer was a differential counter. Its advantages are that it is relatively short compared to a threshold Cerenkov counter (reducing multiple scattering and the chance of in-flight decays of kaons), and is more selective in its identification. However, good particle identification depends on the beam being roughly parallel to the detector's axis. This requires a lens to bring the scattered particles to a parallel beam. The aperture of this lens limits the solid angle acceptance of the spectrometer. It also allows the Cerenkov and trajectory determining detectors to be placed away from the target area - reducing the background from beam halo and unscattered beam.

The momentum analysis of the scattered particle is carried out in the horizontal plane by 5 bending magnets (total length 90 feet). A second lens is placed downstream of the differential counter, resulting in a horizontal image dispersed across its image plane according to the particle's momentum [and independently of its horizontal scattering angle]. The momentum measurement can then be made (to first order) with only one position detector in this plane and another at the target.

The angles and positions at the target of the scattered particle are determined by following the trajectory in the drift space after the magnets back, through the magnets, to the target. Since the system of lenses results in a small beam profile over a long, 400 foot, length (compared with a spectrometer consisting of just a big momentum analysing bend magnet), the spectrometer could be assembled from standard laboratory beam transport magnets. These magnets have very regular fields and so the matrix theory for the beam transport could be used. Mapping the trajectory back to the target (to first order) then reduces to taking linear combinations of coordinates in the drift region. The small beam profile also allowed wire planes of smaller size and fewer elements and therefore simplified readout hardware.

The small divergence allows two of the three long (for efficiency) threshold Cerenkov detectors to be placed after the momentum focus, without needing excessive diameters. Because they are down-stream of the momentum determination, the large multiple scattering due to the gas does not degrade the momentum resolution.

The price paid for the advantages of such a focusing system was a small solid angle acceptance, 4.5×10^{-6} sterad.

2.2 BEAM

The beam used in the experiment was the high resolution secondary beam, M6E, at the FNAL Meson Laboratory. It was an unseparated beam of protons, pions, and kaons produced by bombarding a 1.5

mm. by 203. mm. beryllium wire with extracted accelerator protons. Its energy range was 20 to 200 GeV/c with typical fluxes of 5×10^6 for positive particles and 1×10^6 for negative particles in an 800 ms spill with a 30-70% duty factor. The particle mix is shown in Table 1. The beam consisted of three 'point-to-parallel-to-point' stages - each about 150 meters long. The first collected the particles scattered from the beryllium target, dispersed them by momentum and focused them on a steel slit. This variable width slit selected the momentum band for the subsequent stages; other variable slits set the initial angular acceptance. This stage is shown in figure 1. The second stage imaged the beam, still dispersed by momentum, on the P hodoscope for momentum tagging. The resolution of the tagging is .02%. The path length and a bend magnet served to clean up the halo produced by the momentum aperture slits. The third stage, shown in figure 2, recombined momenta and focused the beam on the hydrogen target. The parallel region before the last set of focusing quadrupoles was used for two differential Cerenkov counters (one a DISC counter). The beam optics also included 13 vernier magnets for steering and 2 field lenses. In the drift space just before the target, 2 sets of crossed hodoscopes (BX, BY, $B\theta$, $B\phi$) tagged the incident angle and position. Table 2 summarizes the beam optical properties.

Table 1.

Particle mix of the M6E Beam

Particle Type	M6E MOMENTUM (GeV/c) 50	70	100	140	175
π^+	.760	.650	.401	.210	.106
K^+	.025	.032	.031	.026	.016
p	.215	.318	.568	.764	.878
π^-	.939	.938	.938	.950	.962
K^-	.026	.032	.041	.041	.034
$\bar{p}$	.035	.030	.021	.009	.004

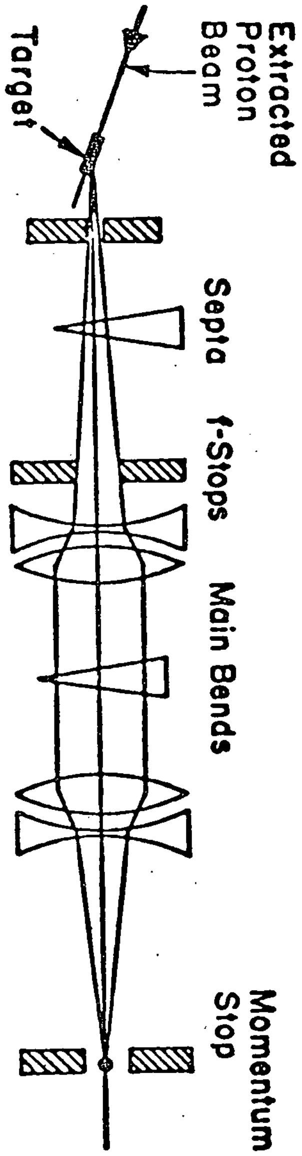

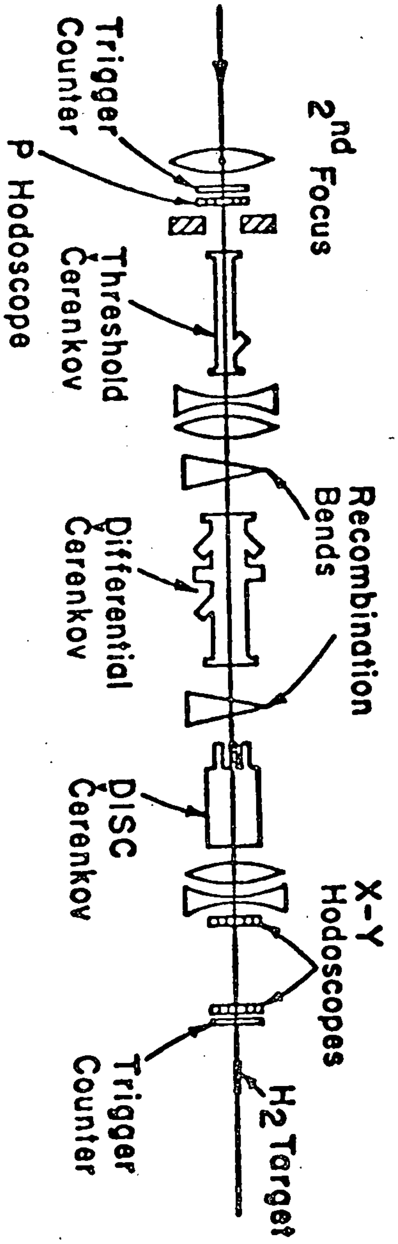

Figure 1: 1st stage of beam (horizontal-plane optics)

Figure 2: 3rd stage of beam, showing instrumentation

2.3 ANGLE VARYING BENDS

The spectrometer has a small uniform angular acceptance, ±1.5 mr. vertical by ±.75 mr. horizontal, about an axis fixed along the beam axis. To vary the scattering angle the beam was pitched up and then down (or down and then up) in such a way that its position at the target did not change but its angle could be varied from 0 to 25 mr. with respect to the spectrometer's axis. See figure 3. Three Main Ring bending magnets were used. These magnets have small apertures so the second and third had to be moved an amount depending on the pitching angle, so the beam could pass through unobstructed. The target was also tilted about its midpoint so that the beam path length in the target would not change with the angle.

The angle of pitching, called the AVB angle, ϕ_{AVB}, is proportional to $\int\vec{B}\bullet\vec{dl}/P$, P is the momentum, $\vec{B}$ is the magnetic field which is proportional to the electric current, and $\vec{l}$ is the length of the field's volume. Thus a given current sets $P\phi_{AVB}$ which is very nearly $\sqrt{t_o}$, $t_o=P_1P_3\phi^2_{AVB}$ being the central t value of the spectrometer for elastic scattering. The t scale is therefore insensitive to uncertainties in the beam momentum. Table 3 summarizes the AVB System.

The three dipoles were powered in series with a fourth (but only 3 foot long) monitor magnet whose field was monitored by a precision rotating coil gaussmeter. The excitation and $\int\vec{B}\bullet\vec{dl}$ of the dipoles were measured to ±.1% with NMR probes and flip coils and calibrated against the monitor magnet. In this way the syste-

Table 2.

Optical Properties of the M6E Beam

(Recombined mode-east branch)

Production Angle:	2.7 mr
Angle with respect to primary proton beam:	$\theta_v = 2.7$ mr $\theta_h \sim 0$
Maximum momentum:	200 GeV/c
Maximum momentum bite:	1.3%
Solid Angle:	$\Delta\theta_h = \pm .56$
	$\Delta\theta_v = \pm .76$
Total =	1.7 μster
Momentum Dispersion at momentum collimator:	6.6 cm/%
Momentum Dispersion at momentum hodoscope:	4.4 cm/%
Momentum Dispersion at hydrogen target:	0
Observed Properties at hydrogen target:*	
horizontal FWHM:	∿ 8 mm
horizontal angular divergence:	∿ .1 mr (σ)
vertical FWHM:	∿ 4 mm
vertical angular divergence:	.2-.3 mr (σ)
Angular divergence in parallel region of third stage	∿.1 mr

---

*These beam properties are energy-dependent due to multiple scattering. They also depend on collimator settings. The numbers given were typical for the beam during data taking.

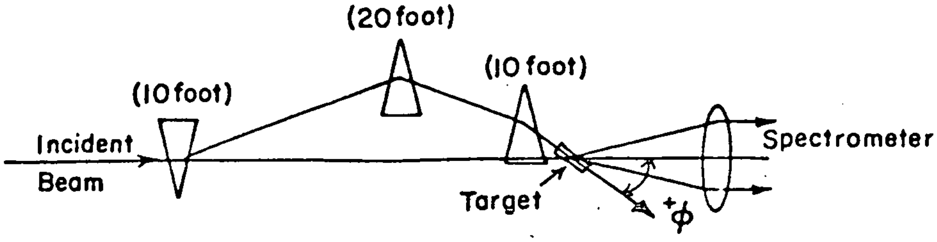

Figure 3: Variation of the scattering angle

Table 3.

Parameters of the AVB System

(ϕ = scattering angle in milliradians)

Height of AVB2	154.53 mils x ϕ
Height of AVB3 (upstream end)	121.63 mils x ϕ
Height of BX, BY hodoscopes	127 mils x ϕ
Angle of AVB3 relative to 0°	.7488 x ϕ
Beam angle at BX, BY hodoscopes	.4975 x ϕ
Power Limit: $p\phi \; \alpha \int B d\ell \; \alpha$ current	3-1/2 GeV/c
Mechanical Limit (due to maximum excursion of jacking system): maximum angle down onto target (Fig. 9a)	100 mr
Maximum angle up, onto target (Fig. 9b)	25 mr
Steering of beam spot at target:	$\sim$15 mils at ϕ = 20 mr

matic error in the central t of the spectrometer was kept to 1/2%. A similar monitoring system was used for the beam bends and again for the spectrometer bends.

2.4 SPECTROMETER

The single arm spectrometer, SAS, optics is much like a fourth stage of the beam. See figures 4 and 5.

An initial logical triplet lens brings the scattered flux to a parallel beam. A short bending magnet sweeps wrong momentum particles away and shields a hodoscope and differential Cerenkov counter. This hodoscope is at the vertical focal plane of the triplet and so a particle's displacement from the optic axis measures its vertical scattering angle. A second logical triplet brings the beam to a horizontal image plane 378 feet, and to a vertical image plane 269 feet, from the target. The main momentum analysing bend magnets are between the triplet and the vertical image plane. Proportional wire chambers are located at the entrance to the first bend magnet, at both image planes, and at the end of the spectrometer. Together with the angle hodoscope at the focal plane, they provide a redundant measurement of the scattered particle's momentum, horizontal and vertical scattering angles, and vertical position at the target. They are also used to see that all the beam passes through the narrow vertical aperture (2 inches) of the bend magnets. Three gas threshold Cerenkov counters follow the last bend magnet.

The uniform acceptance region is defined as the range of spectrometer incident angles for which <u>all</u> the particles coming from a 16 mm by 8 mm 'source' (i.e. projection of the beam on a plane at the target center) are transmitted through the spectrometer and all its detectors[1].

---

[1] For large scattering angles the target tilt results in an elon-

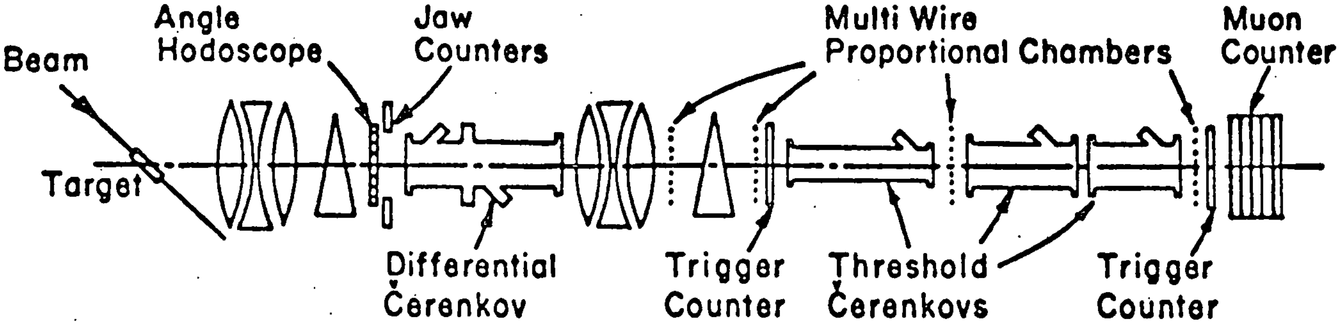

Figure 4: Spectrometer showing instrumentation

---

gated source for the spectrometer. [See Butler 1975: P.43.] This problem was avoided since the angles in this experiment were kept less than 20 mr. for a 20 inch target.

The momentum acceptance is uniform over ±2.5%. This is large enough to easily encompass elastic scattering. [For inelastic scattering experiments the central momentum of the spectrometer was lowered by scaling the magnet currents.]

The spectrometer design momentum resolution was ±.03%. Due to multiple scattering, power supply ripple, and field irregularities in the beam and spectrometer, and the beam design momentum resolution of .02%, the combined actual resolution at 50 GeV/c was .13% and at 175 GeV/c, .07% [Butler 1975: p. 105]. This is to be compared with the .3% needed to just resolve the single pion production threshold at 50 GeV/c.

The scattering angle Φ, is calculated from its horizontal and vertical components, θ and ϕ, using:

$$\Phi^2 = \theta^2 + \phi^2 \tag{5}$$

since all the angles are small. The angles θ and ϕ are given by

$$\begin{gathered} \theta = \theta s - \theta b \\ \phi = \phi_{AVG} + \phi s - \phi b \end{gathered} \tag{6}$$

where θb, ϕb are the component angles of the incident beam as measured by the two sets of crossed hodoscopes and θs, ϕs are the component angles of the scattered beam as it leaves the target. θs, ϕs are calculated from the trajectory measured in the

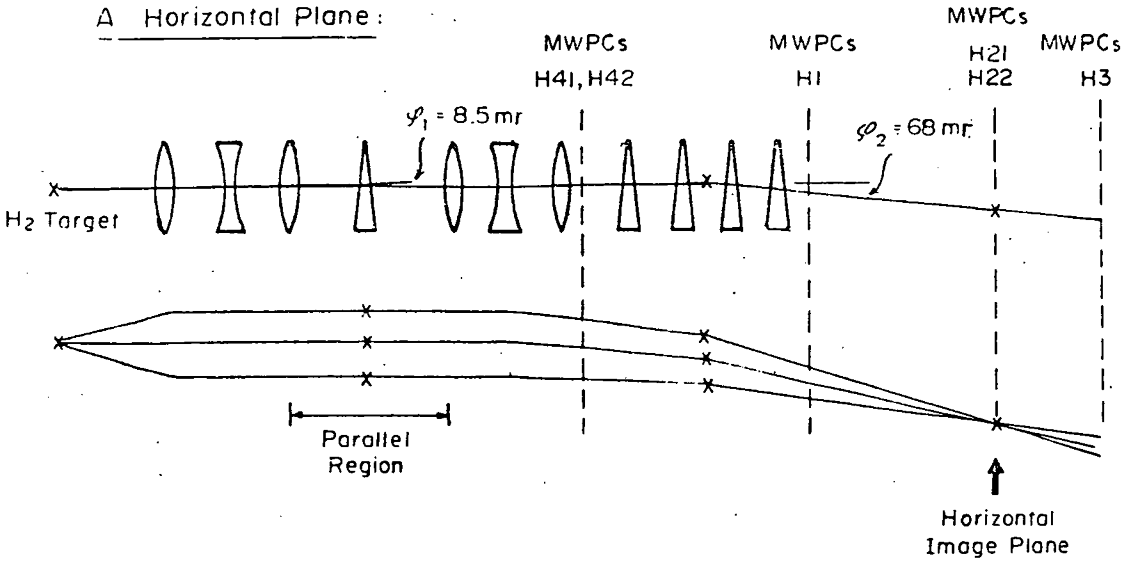

A Horizontal Plane:

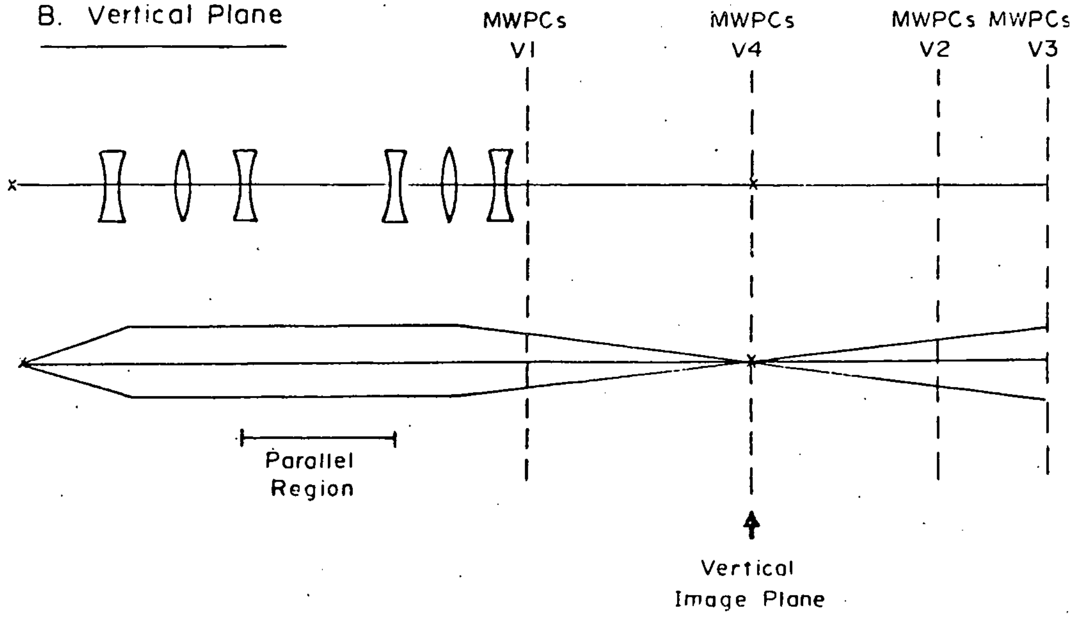

B. Vertical Plane

Figure 5: Spectrometer optics and wire planes

Table 4.

Optical Properties of the Single Arm Spectrometer

Horizontal Plane:

Focal Plane: (107.27')	angular dispersion:		2.9 cm/mr
Image Plane: (377.7')	magnification:		1.8
	momentum dispersion:	spatial:	3.7 cm/%
		angular:	0.7 mr/%

Vertical Plane:

Focal Plane: (88.06')	angular dispersion:		1.03 cm/mr
Image Plane: (269.3')	magnification:		4.08
	momentum dispersion:	spatial:	0.0
		angular:	0.0

Parallel Region:	beginning	78.5' from H_2 target
	end	135.8' from H_2 target
	length	57.3'

Spectrometer Acceptance:

Horizontal angle (uniform):	1.5 mr
Vertical angle (uniform):	3.0 mr
Momentum (uniform):	5.0%
Solid angle: (uniform)	∿ 4.5 μster
(total)	~ 7.0 μster
Vertical height at target:	at least 9 mm
Horizontal extent at target:	~ 16mm

Solid angle as a function of veto counter setting near spectrometer focal plane: $\Delta\Omega(\mu\text{ster}) = .335\ \Delta x(\text{cm})\Delta y(\text{cm})$ Δx, Δy horizontal and vertical veto counter opening resp.

spectrometer and the magnet fields. See Section 'Event Reconstruction' below. The geometry can be visualized as in Figure 6. Note that in this thesis θ, ϕ are used, depending on the context, as scattering angle components as well as the scattering angle itself. [The latter usually in $t=-P^2\theta^2$ or $-P^2\phi^2$].

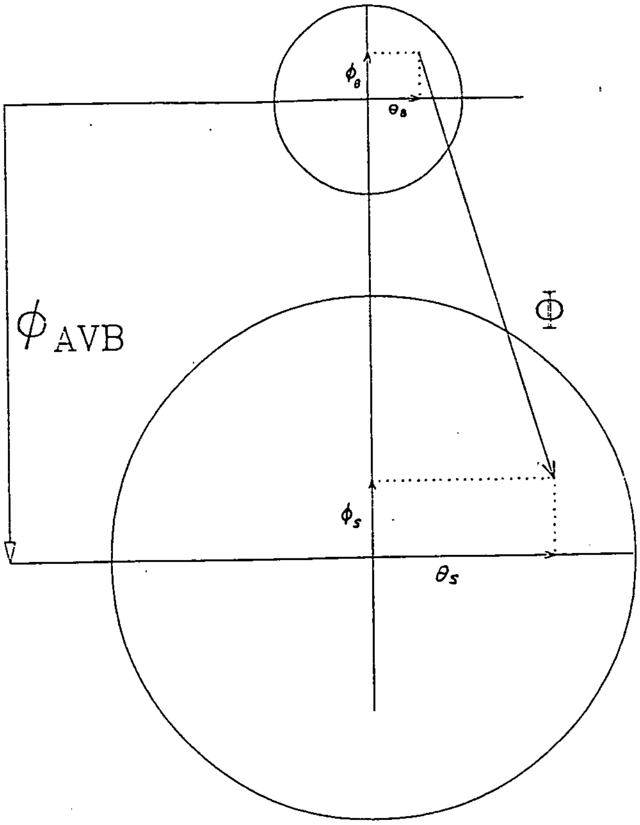

Figure 6: Beam, Spectrometer, and Scattering Angle definitions

2.5 DETECTORS

2.5.1 Trigger counters

Several scintillation detectors were placed in the beam and spectrometer to serve as trigger and veto detectors. See figures 2 and 4. Beam trigger counters, ET1 and BT2, were located at the second focus and between the second and third AVB magnets. This second trigger counter moved vertically in order to remain fixed with respect to the beam centroid as the AVB System pitched the beam. The beam vetos were a variable hole counter just before the target to veto halo and restrict the beam size and another in the parallel region of the last beam stage to restrict the angular divergence of the beam at the target.

Two trigger counters in coincidence in the spectrometer, ST1 and ST2, were used to indicate that a particle had been scattered into the spectrometer. The first was placed after the last bend magnet and the second at the end of the spectrometer. Also there was a variable jaw counter in the parallel section just before the differential Cerenkov counter. The four elements of the counter were separately movable and were used to indicate particles outside the uniform acceptance region. They were used in the trigger only when the event rate was high. They were also used in the solid angle calibration.

2.5.2 Cerenkov Counters

A charged particle travelling in a medium locally polarises the medium along its path. When the medium relaxes it radiates. Only if the particle's velocity is greater than the speed of light in the medium will the radiation emitted interfere constructively along the path. In that case the light moves away from the path at an angle given by

$$\cos\theta = c/nv \qquad (7)$$

where n is the refractive index of the medium, and v the velocity of the particle. Different mass particles of the same momentum will have different velocities and hence different cone angles for the light. If $c/nv > 1$ no light is emitted. The refractive index for a gas increases with its pressure. A threshold Cerenkov counter has its pressure set so that particles lighter than some mass (therefore faster) radiate, but those heavier do not. A differential Cerenkov counter identifies particles by being sensitive to a small range of Cerenkov cone angles and thereby a small range of velocities and mass. The intensity of light of frequency ω is given by

$$I(\omega) = e^2/c^2 \, l \omega \sin^2 \theta \qquad (8)$$

where l is the length of the radiator.
An excellent review of Cerenkov detectors is given in Litt 1974.

2.5.2.1 Beam Cerenkov Counters

There were three Cerenkov counters in the beam. The first, a 60 foot gas threshold counter was set to count pions. It was filled with helium gas and a spherical lucite mirror focused the Cerenkov light onto a phototube. See Ayres 1974 for a detailed description.

The second was a differential counter with 411 inches of either helium or nitrogen radiator. In this counter the pressure was set so that the cone of Cerenkov light from the desired particle type passed through an annular hole in a mirror and was focused by another mirror into a phototube. Light from other particle types would have a larger or smaller cone angle and would not pass through; instead it would be reflected onto two other photo tubes. The annulus for this counter was 10±.6 mr. At 50 GeV, it was pressurized to detect kaons; at higher energies, protons. See Anderson 1976 for a detailed description.

The third was a sophisticated differential counter called a DISC - Differential Isochronous Self Collimating. It requires a particularly parallel beam but has very high rejection of particles for which it is not tuned. Its cone angle is 24.5 mr. and therefore operates at higher pressures than the beam differential counter, but is much shorter, 13 feet. The angular spread of the Cerenkov cone is given by differentiating equation 7, at small angles

$$\theta d\theta = d\beta/\beta + dn/n \tag{9}$$

Now dn is not zero since the refractive index varies with the frequency of the Cerenkov light - which covers a broad spectrum from blue into the UV. If two masses are close together, at high energy $\Delta\beta/\beta\theta$ may be dominated by $\Delta n/n\theta$. The DISC has a sodium chloride and quartz chromatic corrector lens to compensate for Δn. It also has a coma corrector for the spherical mirrors. The index of refraction is measured directly with a laser interferometer, rather than by using pressure vs. n tables. At 50 GeV the DISC was set to count protons, at higher energies, kaons. See Benot 1972 for a detailed description.

The strategy for operating these three counters was to have them identify particles as unambiguously as possible at the expense of efficiency, in order to minimize contamination of minority particle (kaon and anti-proton) cross-sections by the others. For example, the pressure of the threshold counter would be set on the high mass side of a pressure vs. counting rate peak - towards the kaons. This causes more kaons to be counted as pions but fewer pions go unseen and contaminate kaons.

At 50 GeV, the particles are most easily separated. An important consideration at this energy, however, was multiple scattering of the beam by the Cerenkov counter gases which reduces the resolution of all measurements. The DISC counting protons and the DIFF counting kaons configuration at this energy minimized multiple scattering.

2.5.2.2 Spectrometer Cerenkov counters

There were four Cerenkov counters in the spectrometer. A differential counter was placed in the parallel section to trigger on nucleons. There were several anti-coincidence mirrors giving Cerenkov angles cf 8.5 cr 10. mr with angular ranges of ±.5, ±.75, ±1.0 mr. The three threshold counters were made from steel pipes upto 16 inches in diameter. Their lengths were 31.5 m, 14.2 m, and 6.9 m. Since the first was before the momentum focus, its mirror was made of lucite, instead of glass, and had mylar, instead of aluminum, windows to minimize multiple scattering. The first detected only pions. The latter two detected pions and kaons. Since efficiency increases with light intensity, which is proportional to the radiator length, the first was made quite long, 31.5 m, so that it counted pions very efficiently. In this way the small number of kaons could be separated reliably from the pion-plus-kaon signal of the latter two detectors. For a detailed description of the threshold detectors see Ayres 1974; for the differential counter, see Anderson 1976. See the section 'particle identification' in the next chapter for details of their performance.

2.6 TARGETS

Six targets could be remotely selected. They were ten inches or twenty inches in length and were filled with hydrogen, deuterium, or were empty. The target cells were one inch diameter mylar tubes with 7.5 mil. walls, and all were contained in an evacuated aluminum target box with mylar windows for the beam, scattered and recoiling particles. The cells were wrapped with superinsulation. Target lengths were known to .1% by surveying them - cold and pressurized. Carbon resistors monitored the reservoir. A vapor pressure gauge monitored the target density. Since the cells were much bigger than the beam spot, their alignment was not critical.

2.7 FAST ELECTRONICS AND DETECTOR INTERFACING

The fast electronics provided signals 1) to the computer to indicate that a scattering event had taken place and data was ready to be read in from the interfaces, 2) to the detector interfaces to gate the information in from the detectors for that, and only that, event, 3) to scalers to count the beam flux, which is needed in the cross-section calculation, and 4) to scalers and interfaces to provide diagnostic information for monitoring, setup, and calibration of the apparatus.

There were two event triggers in the experiment. The 'spectrometer event' trigger indicated a scattering event. The 'beam event' trigger provided a random sample of beam particles in order to determine the beam phase space distribution. The use of this distribution is described in the next chapter.

Figure 7 is a simplified schematic of the trigger logic. The two event triggers are generated from the three signals BT, BTC, and ST. BT and ST are logical combinations of the beam and spectrometer trigger counter signals as described in section 2.5.1 and shown in figure 8. BTC is generated from the 3 beam Cerenkov logic signals identifying the three possible beam particles. At small scattering angles there were more majority particle events than could be handled by the computer. The three particle identity signals could be counted down separately (by 2^n, for n set by a switch) before being OR'ed together for BTC. By allowing only every 2^n'th majority particle to enter the event coincidences, the relative flux of kaons and anti-protons was enhanced.

The number of beam events was controlled by counting down BT as well. Roughly equal numbers of the two event types were taken. Note that the same beam logic is applied to spectrometer events as to beam events, and so the beam events accurately indicate the phase space of the beam particles in the spectrometer events.

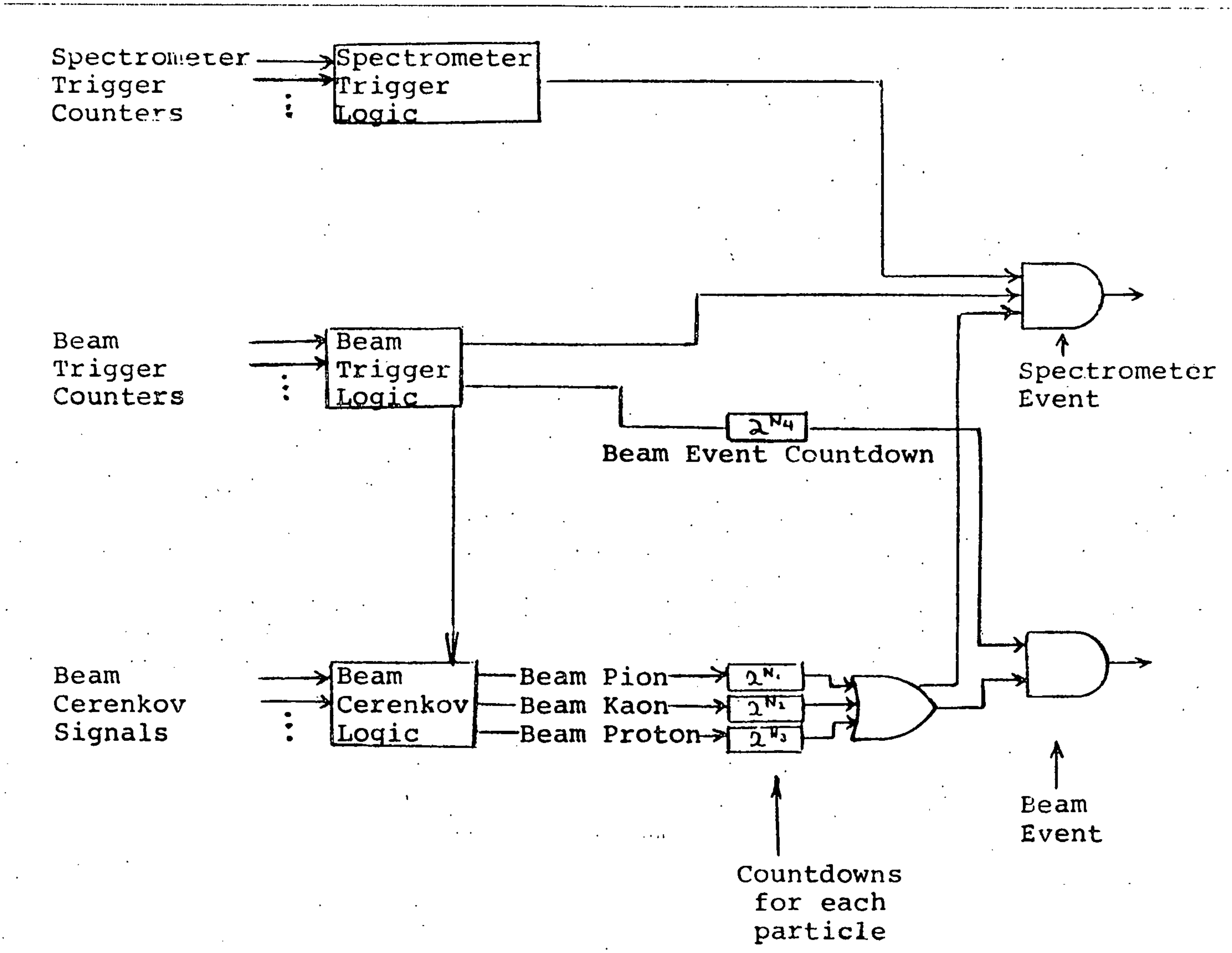
Spectrometer Trigger Counters
Spectrometer Trigger Logic
Beam Trigger Counters
Beam Trigger Logic
2^{N_4}
Beam Event Countdown
Spectrometer Event
Beam Cerenkov Signals
Beam Cerenkov Logic
Beam Pion
Beam Kaon
Beam Proton
2^{N_1}
2^{N_2}
2^{N_3}
Countdowns for each particle
Beam Event

When an event was signaled by the fast electronics a fast veto was applied to the electronics, including the flux scalers. This veto remained in effect until the computer signaled that it had completed reading in the event (200-300 micro seconds). The detector signals were timed so that they arrived at their computer interfaces during a data strobe gate started by the event trigger and lasting about 10-15 nano-seconds. [Beam particles are 'bunched up' at 19 nano-second intervals.] The interfaces held the status of the detector signals in bit latches until the computer readin was completed. One and only one event was held at a time. [Events with 2 or more beam particles in one 'bunch' were eliminated by the data analysis.]

Two interface systems were used. The first was CAMAC, an international convention for a modular system for computer - instrumentation interfacing. It handled all the hodoscopes, Cerenkov, and trigger counter signals, the fast electronics' logic bits, the scalers, ADC's and TDC's, as well as some experimenter - computer communication and experiment control signals. Event information was read from the CAMAC system by direct memory access transfers.

The MWPC's had their own separate interface. It is described by Anelli [1971]. Only the addresses of wires that were hit and an interface status word were transfered to the computer. Typically only 15 addresses were transfered from 800 possible wires. Again DMA transfers were used.

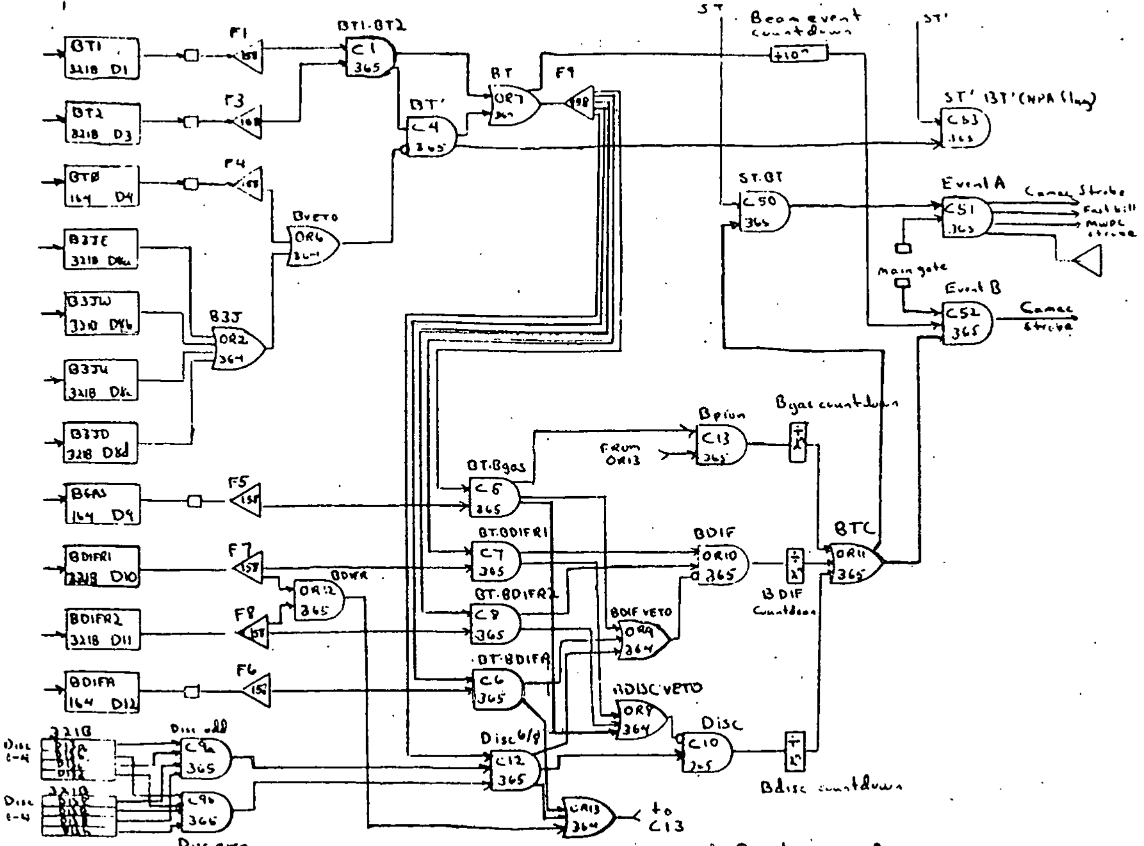

Beam trigger logic and final coincidences

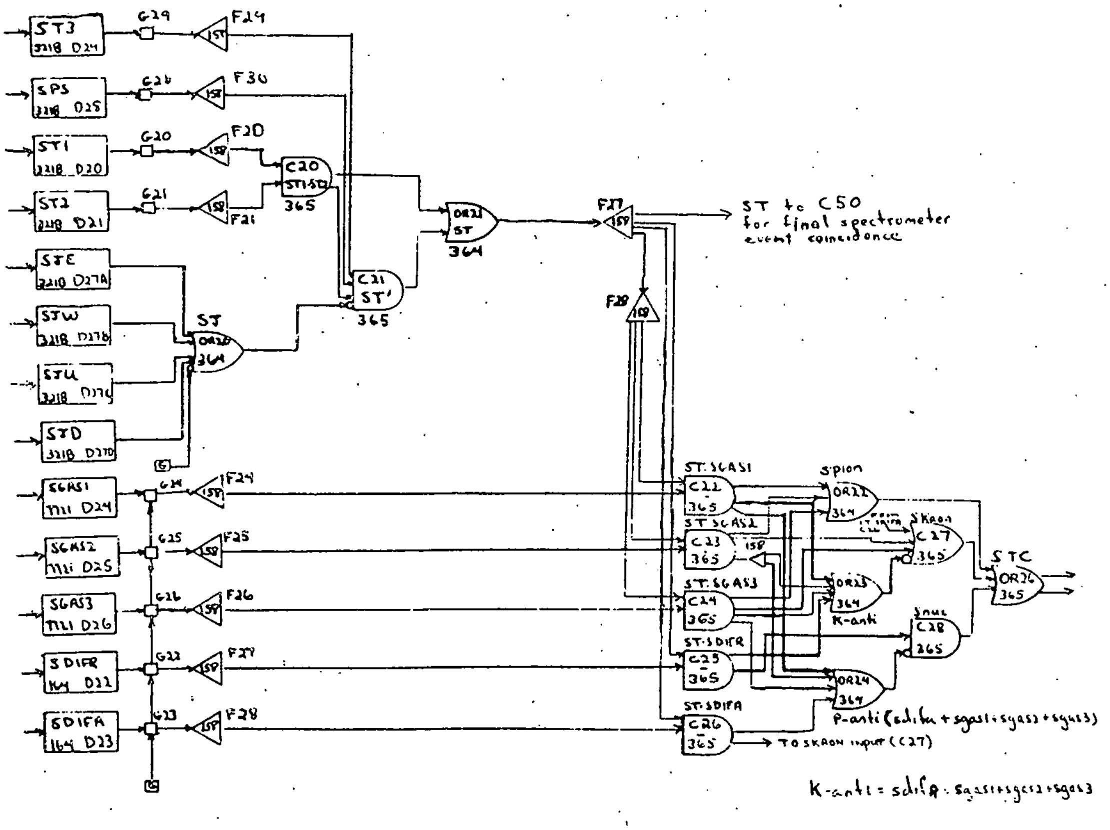

Figure 8: Fast Electronics Schematic

Besides collecting event information, the interfacing enabled the experimenter to easily control the running of the experiment and record the running conditions. In response to commands to begin, pause, resume, and end data taking, the electronics and interfaces could be reset, gated on and off, and various running conditions recorded.

2.8 ONLINE SYSTEM

A PDP11/45 computer with the SPEX multi-tasking system [Massimo 1972,1975] was used for the data collection. The associated hardware included storage type CRT display, two disk memories, magnetic tape and DECtape units, an electrostatic printer/plotter, and 28K of core memory. SPEX loaded the programs from the disk in response to internal and external conditions. Several 'tasks' could be run at once with SPEX handling their communication and synchronization.

The online system was used to record events and running conditions, perform a simple data analysis including a cross-section calculation, and monitor the equipment. It also aided in setting high voltages and timing delays for the hodoscopes and MWPCs, checking beam optics and steering, and doing other setup and checkout chores. Conditions set up at the beginning of each run included the target (hydrogen, deuterium, or empty) and central values for the spectrometer angle, spectrometer momentum, and beam momentum. At the start of each run the magnetic field strength in the beam, spectrometer, and angle varying bend magnets, the Cerenkov pressures and temperatures, and the position of most movables such as the target, some counters, and the pitching magnets, were read into the computer. These and the online system parameters were printed as well as written on magnetic tape. Following a system reset of the electronics, the computer was switched to the event acquisition mode. An event consisted of 50 to 70 16-bit words read via CAMAC and the wire chamber interface. Typical runs included 5K to 65K events. Tape speed and buffer size limited the data taking to about 200 events (14000 words) per accelerator spill.

The computer decoded both beam and spectrometer event data and created tables of hodoscope and MWPC efficiencies, counts of events passing various cuts, counts of particle and reaction types, beam profiles at each detector, pulse height spectra, and other diagnostic aids. Simultaneously, the events, exactly as read, were written to a magnetic tape for offline analysis. For selected spectrometer events, particle trajectories were reconstructed using first and second order TRANSPORT matrices. [See the section 'Event Reconstruction' below.] Events were then binned by scattering angle and momentum loss for the cross-section calculation done at the end of the run. Various phase-space projection histograms were also created. We were able to view any of over 75 histograms on a CRT and make a permanent copy at any time during the run. At the end of a run the diagnostic and summary tables with the final scaler readings, various counting-rate ratios of interest, beam spot size and focus location, the kinematic running conditions, and plots of the histograms were printed out. During the run a scanning digital voltmeter periodically read the photo-multiplier high voltages and the online system compared these readings to a table of standards, signaling any errors.

Chapter III

CALCULATION OF THE PROTON AND DEUTERON CROSS-SECTIONS

3.1 EVENT RECONSTRUCTION

3.1.1 beam coordinates

There are five scintillator hodoscopes in the beam to measure the five beam phase space coordinates of each event:

δ_b, the percent deviation of the momentum from the central momentum, i.e. $P_b = (1+\delta_b/100)\,P_b{}^{o}$,

θ_b, ϕ_b, the projections of the incident angle at the target midplane, and

x_b, y_b, the position of the beam particle at the target midplane.

The location of the hodoscopes is shown in figure 2. The number of bins and their sizes are shown in table 5. The two downstream hodoscopes were moved when the AVB angle was changed to keep their center on the central trajectory of the beam.

To get a coordinate, the hodoscope element number which was struck was converted to a displacement from the central trajectory. The five coordinates are thus given by the five displacements S in cm. as:

$$\begin{aligned}
\delta_b\ (\%) &= (S_\delta - 1.576\, X_p)/4.44 = S_\delta/4.44 \\
\theta_b\ (\text{mr}) &= (S_{xd} - S_{xu})/(z_{xd} - z_{xu}) = (S_{xd} - S_{xu})/1689.2 \\
\phi_b\ (\text{mr}) &= (S_{yd} - S_{yu})/(z_{yd} - z_{yu}) = (S_{yd} - S_{yu})/1676.0 \\
x_b\ (\text{cm}) &= (-z_{xu})\,\theta_b + S_{xu} \qquad z_{xu} = 457.2\ \text{cm.} \\
y_b\ (\text{cm}) &= (-z_{yu})\,\phi_b + S_{yu} \qquad z_{yu} = 433.2\ \text{cm.}
\end{aligned} \tag{10}$$

Table 5.

Beam Hodoscope Properties

Beam Hodoscopes:

name	location	# of elements	Decode sense	element extent in decode plane	element thickness along beam
BP	1037.865' (second focus of M6 beam)	30	horitonzal	2.504 mm	10 mm
BΘ	1400.384' (just after Q17)	8	horizontal	3.385 mm	5 mm
Bφ	1400.384'	8	vertical	3.49 mm	5 mm
BX	1454.458' (between AVB2, AVB3)	16	horizontal	0.965 mm	3 mm
BY	1456.073'	8	vertical	0.965 mm	3 mm

where x, y refer to hodoscopes measuring x (horizontal) or y (vertical) displacements; u, d refer to the upstream or downstream pairs of crossed hodoscopes, and z refers to the z coordinate of a hodoscope relative to the target midplane. X_P is the horizontal position at the beryllium production target - which is only known to be within the 1.5 mm diameter wire and is therefore assumed to be zero.

All the displacements, S_i, were randomized over one bin size since the trajectory could have passed anywhere in the bin. If two adjacent elements were struck the coordinate was set to be the average, but the randomization was done over only 1/10 bin. Adjacent hits usually are caused by delta rays (knock-on electrons) whose range is small. This randomization eliminates false structure in plots which would occur if combinations of only discrete detector coordinates were used in computing θ, ϕ, etc.

3.1.2 spectrometer coordinates

The trajectory in the spectrometer is measured by ten multi-wire proportional chambers. (See table 6 and figure 5). The wire spacing was 2 mm. At the momentum focus two chambers were placed 2 cm. apart, offset by 1 mm. to give 1 mm. bins for finer resolution. There were a total of 800 wires in the nine logical planes. The scintillator hodoscope at the focal plane consisted of ten counters, overlapped by thirds, for 19 logical bins of 2.15 mm each (corresponds to .22 mr. at target). The construction of the wire chambers is discussed in Anelli 1971. Table 6 summarizes their properties.

Since the solid angle is small the chance of more than one particle in the spectrometer is small. The reconstruction of tracks in the drift part of the spectrometer (after the magnets) is therefore unambiguous. The straight line trajectory is defined by the displacements x and y from the spectrometer axis at the momentum focus and the two angles θ, and ϕ_1 with respect to that axis. [The subscript 1 refers to the momentum focus location.]

Table 6.

Wire Chamber Properties

Name	Location	# of 32 wire groups	# of wires	Sensitive Region horiz x vert (mm) (mm)	Decode Sense
V1	1645.54' (after last spectrometer quad)	2	64	180 x 128	vertical
H41	1644.18'	2	64	128 x 345	horizontal
H1	1738.13' (after last bend magnet)	2	64	128 x 180	horizintal
V4	1739.20' (spectrometer vertical focus)	1	32	280 x 64	vertical
H21	1847.58' (spectrometer horizontal focus)	4	128	256 x 90	horizontal
H22	1848.24'	4	128	256 x 90	horizontal
V2	1849.91'	1	32	280 x 64	vertical
H3	1930.17' (end of spectrometer)	5	160	320 x 190	horizontal
V3	1931.39'	2	64	345 x 128	vertical
H42	1646.45'	2	64	128 x 180	horizontal
Total wires:			800		

All chambers have 2 mm wire spacing.
H22 and H21 are offset horizontally by 1 mm to form a single logical chamber with 1 mm spacing.
H41 and H42 are arranged the same way.

Referring to figure 5, we see that there is redundancy in the measurements - eight planes (not including H41 and H42 before the bends) for four coordinates. In fact the planes H3 and V3 at the end of the spectrometer were not used in the reconstruction since reconstruction efficiency was sufficient without them and their resolution was poor due to multiple scattering in the Cerenkov counters. In the horizontal plane one of either H21 or H22 coordinates could be missing resulting in only a loss of resolution from .5 mm to 1 mm. In the vertical plane V1 and V2 were used since they provided the best angular resolution. If either V1 or V2 coordinates were missing, we used V4, located between them, as a substitute. Fitting to more than two planes was not warranted since tests showed it did not significantly increase the resolution. If all of V1, V2, and V4 had ambiguous or missing hits, the focal plane hodoscope was used in the reconstruction instead. In this way we were able to reconstruct about 95% of the events.

Up to three adjacent wires hit was accepted as a single coordinate, the value being their average. Just as for the beam measurements, the spectrometer measurements were randomized over one bin. Butler 1975 shows and interprets profiles of the scattered flux at the various wire chamber planes.

3.1.3 Extracting the scattered particle coordinates

There are five phase space coordinates of the scattered particle at the target to be determined: x_s, y_s, θ_s, ϕ_s, and δ_s - analogous to the five coordinates of the beam particle. The four coordinates x_1, y_1, θ_1, ϕ_1 measured in the drift region of the spectrometer are clearly insufficient to define all five. If we knew the momentum x_1, y_1, θ_1, ϕ_1 would unambiguously define x_s, y_s, θ_s, ϕ_s. For a point source at the target, the displacement at the momentum focus would give the momentum directly. For a finite source, however, there is a magnified image at the focus. Knowing the x coordinate of the particle at the source and the magnification factor allows one to calculate the momentum. [The angle coordinate at the source is not needed since, by definition of a focus, all angles are brought to the same point.] We can approximate the x coordinate very well by its projection on the target midplane, x_b. Thus knowing the momentum, we can now trace the trajectory from the drift region back through each magnet to the target.

As mentioned earlier, the small magnet apertures allow us to use the first and second order Matrix Theory of beam transport [Brown 1972, 1975]. Briefly, the trajectories through a magnet are described by means of a Taylor series expansion about the 'central trajectory' - that trajectory which passes through the magnetic center of the magnet. Terms to second order are kept. To first order the coordinates of a particle on exit from a magnet are linear combinations of its entrance coordinates. The effect of a series of magnets is thus given by the product of the matrices describing each magnet. The program, TRANSPORT [Brown 1975], calculates such 'transfer matrices' from input describing the field strengths and positions of the spectrometer magnets. The coordinates at location Z, downstream from the target at Z=0, are given, to second order by:

$$X_i^2 = \Sigma_j R_{ij} X_j^0 + \Sigma_{jK} T_{ijK} X_j^0 X_K^0 \qquad (11)$$

where the x_i are: $x, y, \theta, \phi, \delta$. Since the momentum remains constant, i.e. $\delta^0 = \delta^2$, $R_{\delta j} = \delta_{\delta j}$. Also, since the bend is in the horizontal plane, $R_{\phi\delta} = R_{y\delta} = 0$. Since the quadrupoles are symmetric about the horizontal plane, the horizontal and vertical are decoupled and $R_{xy} = R_{yx} = R_{\theta\phi} = R_{\phi\theta} = R_{x\phi} = R_{\phi x} = R_{\theta y} = R_{y\theta} = 0$. This leaves six nontrivial coefficients. The matrices R and T can be inverted to give the coordinates at the target

$$X_i^0 = \Sigma_j R_{ij}^{-1} X_j^2 + \Sigma_{jK} T_{ijK}^{-1} X_j^2 X_K^2 \qquad (12)$$

where R^{-1} is the usual matrix inverse and

$$T_{ijK}^{-1} = \Sigma_{lm} R_{jl}^{-1} T_{ilm} R_{km}^{-1} \qquad (13)$$

Since we know $x^0 = x_b$ and do not know $\delta^0 = \delta_s$, we must first solve equation 12 for i=x, invert it to get δ_s and only then can we solve for the other coordinates. Using subscript s to indicate the scattered particles coordinates at the target and, 1 the coordinates at the momentum focus, we get, to first order:

$$X_s = R_{xx}^{-1} X_1 + R_{x\delta}^{-1} \delta_s = X_b \qquad (\delta_1 = \delta_s) \qquad (14)$$

so

$$\delta_s = (X_b - R_{xx}^{-1} X_1) / R_{x\delta}^{-1}$$

and

$$\begin{aligned} \theta_s &= R_{\theta x}^{-1} X_1 + R_{\theta\theta}^{-1} \theta_1 + R_{\theta\delta}^{-1} \delta_s \\ Y_s &= R_{YY}^{-1} Y_1 + R_{Y\phi}^{-1} \phi_1 \\ \phi_s &= R_{\phi Y}^{-1} Y_1 + R_{\phi\phi}^{-1} \phi_1 \end{aligned} \qquad (15)$$

The matrix, R^{-1}, is shown in table 7.

The calculation to second order is done analogously. The equation relating x_s and δ_s is a quadratic, however. Table 7 shows those second order coefficients that are not zero nor very small.

Table 7.

The Matrices R^{-1} and T^{-1} (from focus to target)

R^{-1}	x'	θ'	y'	ϕ'	δ'
x^o	-.547	0	0	0	2.029
θ^o	.1625	-1.828	0	0	.692
y^o	0	0	-.245	.818	0
ϕ^o	0	0	.752	-6.60	0
δ^o	0	0	0	0	1

T_{xx}	1.53×10^{-2}	$T_{x\theta}$	-1.48×10^{-1}	$T_{x\delta}$	3.04×10^{-2}
$T_{\theta x}$	4.88×10^{-3}	$T_{\theta\theta}$	-7.34×10^{-3}	$T_{\theta\delta}$	-1.90×10^{-2}
T_{yy}	1.66×10^{-2}	$T_{y\phi}$	-1.68×10^{-1}		
$T_{\phi y}$	-5.56×10^{-3}	$T_{\phi\phi}$	8.55×10^{-2}		

The angle ϕ_s is also given by the vertical coordinate at the focal plane of the first triplet, as measured by the hodoscope at that location. From the transfer matrix calculated there we get, to first order:

$$\phi_s = .9703\, Y_{FP} \tag{16}$$

The scattering angles and momentum loss are calculated from ϕ_b, ϕ_s, θ_b, θ_s, δ_b, δ_s as:

$$\begin{aligned} \phi &= \phi_{AVB} + \phi_s - \phi_b \\ \Theta &= \theta_s - \theta_b \\ \Delta P &= P_b - P_s = P_b^o(1+\delta_b/100) - P_s^o(1+\delta_s/100) \\ &= \delta_b P_b - \delta_s P_s + (P_b^o - P_s^o) \end{aligned} \tag{17}$$

For $P_b{}^o$ and $P_s{}^o$, the central momentum for the beam and spectrometer; and ϕ_{AVG} the central angle of the spectrometer.

3.2 THE CROSS-SECTION IN TERMS OF MEASURED QUANTITIES

The goal of this experiment was to measure elastic scattering cross-sections for several reactions as a function of the 4-momentum transfer, t, by counting the number of events of each reaction type that scattered into small intervals of t, over the range $.05 < |t| < .45$. We did not measure t directly but rather the scattering angles θ and ϕ defined earlier. Each event was counted in a bin depending on its θ and ϕ. For small angles the scattering angle is $\mathrm{sqrt}(\theta^2+\phi^2)$ and $d\Omega = d\theta d\phi$. See figure 6 above. Now the yield of events into the bin at $(\theta i, \phi j)$ of size $\Delta\theta\Delta\phi$ is:

$$Y(\phi_i \cdot \theta_i); \Delta\theta, \Delta\phi) = \frac{\rho l N}{A} B \int_{\theta_j - \frac{\Delta\theta}{2}}^{\theta_j + \frac{\Delta\theta}{2}} \int_{\phi_i - \frac{\Delta\phi}{2}}^{\phi_i + \frac{\Delta\phi}{2}} \frac{d\sigma}{d\Omega}(t)\, d\theta\, d\phi \qquad (18)$$

where $t = t(\theta,\phi) = -PbPs(\phi^2+\theta^2)$
$d\Omega = d\theta d\phi$
B = beam flux
N = Avogadro's number
l = target length
ρ = target density
A = atomic weight of target
$\Delta\theta, \Delta\phi$ = binsize
θi, ϕj central values for bin ij

We want to derive an expression for $d\sigma/d\Omega$ in terms of the other variables. If we choose bins small enough so that $d\sigma/d\Omega$ does not change appreciably over the bin we can write

$$Y_{ij} = \frac{\rho l N}{A} B \frac{d\sigma}{d\Omega}(\bar{t}_{ij}) \int_i \int_j d\theta\, d\phi \qquad (19)$$

where $\bar{t}_{ij}$ is the average value of t for the ij'th bin, i.e.

$$\bar{t}_{ij} = \frac{\rho \ell N}{A} B \int_i \int_j t \frac{d\sigma}{d\Omega}(t) \, d\theta \, d\phi \qquad (20)$$

We can measure $\bar{t}_{ij}$ as

$$\bar{t}_{ij} = \frac{\sum_{\text{in bin } ij}^{\text{all events}} t(\theta, \phi)}{Y_{ij}} = \frac{-P_b P_s \sum (\theta_i^2 + \phi_i^2)}{Y_{ij}} \qquad (21)$$

So far this is correct only for a very narrow beam, (i.e. RMS spread in beam ϕ << scattered ϕ). In this experiment $\phi = \phi avb + \phi s - \phi b$ where ϕs is not much larger than ϕb. In this case the edge bins are cut off by the beam and spectrometer angle limits differently than are the central bins. Also we must take into account that different bins 'see' different parts of the beam, and the beam is not uniform over its limits. This situation is shown in figure 9a. The vertical and horizontal lines are the beam and spectrometer limits. The points shown correspond to events with various combinations of ϕb and ϕs, but all lying in the same ϕi bin, i.e. $\phi i < \phi avb + \phi s - \phi b < \phi i + \Delta\phi$. Note that bin A sees a different portion of the beam than does bin B.

Equation 19 must be written

$$Y_{ij} = \frac{\rho \ell N}{A} B \frac{d\sigma}{d\Omega}(\bar{t}_{ij}) \iiiint B(\theta_b, \phi_b) \, d\theta_b d\theta_s d\phi_b d\phi_s \qquad (22)$$

In effect there are still only two integrals since there are two constraints of the form $\phi = \phi s - \phi b$. The beam flux now depends on the beam angle co-ordinates. $B(\theta b, \phi b)$ is determined from a

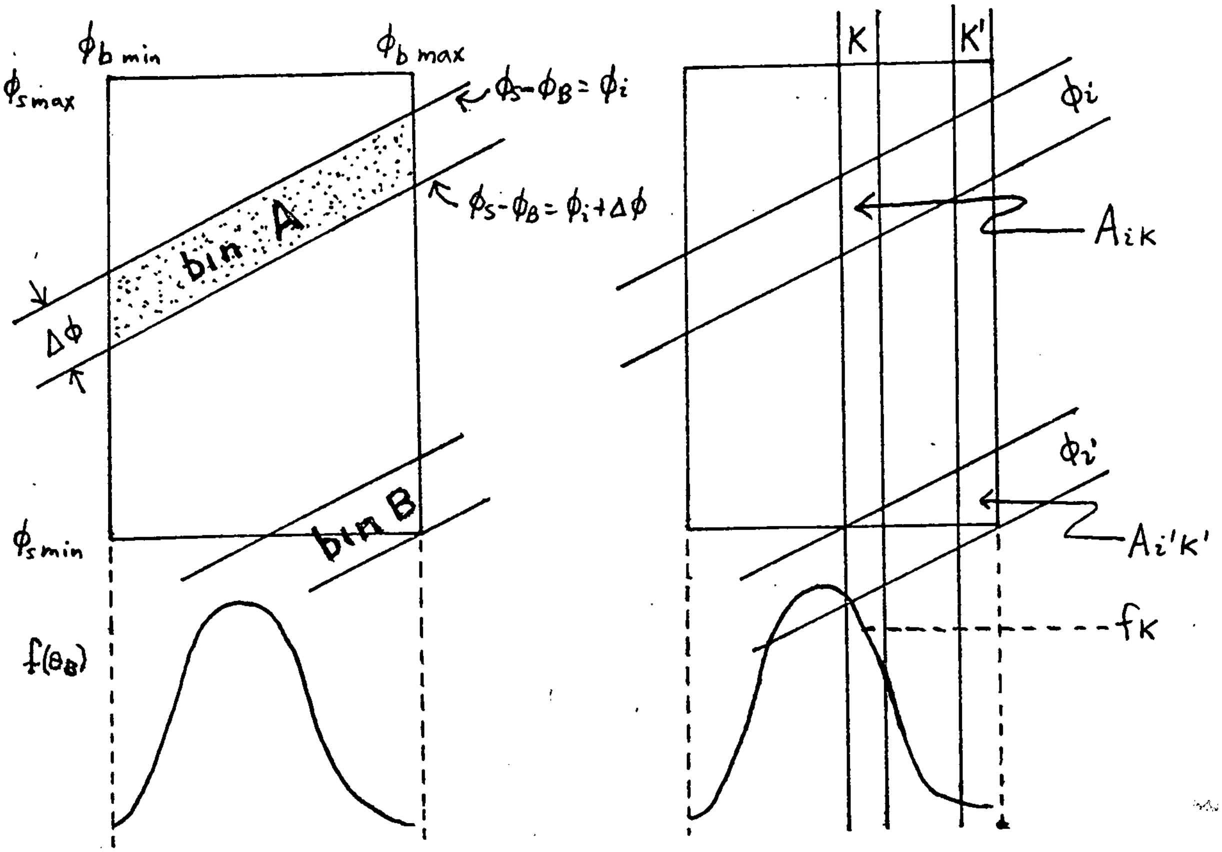

Figure 9: Yield bins and the beam and spectrometer cuts

random sample of beam particles -- the 'beam events' discussed earlier.[1] An analysis of the beam events indicated that to good approximation θb and ϕb were uncorrelated and so we can write:

$$B(\theta_b, \phi_b) = B\, f_\theta(\theta_b)\; f_\phi(\phi_b) \tag{23}$$

where for convenience we have defined f normalized to unity. The integrals of equation 22 now separate:

$$B \cdot \int_{\phi\, bin\, i} f_\phi(\phi_b)\, d\phi_b\, d\phi_s \cdot \int_{\theta\, bin\, j} f_\theta(\theta_b)\, d\theta_b\, d\theta_s \tag{24}$$

---

[1] We can regain equation 19 by setting $B(\theta b, \phi b) = B\delta(\theta)\delta(\phi)$ and integrating over the beam phase space. In that case 0 = θs and $\phi = \phi s$ and we can further simplify by integrating again and get $B\Delta\theta\Delta\phi$.

Each integral is over a region like the dotted regions in figure 9a. If f is binned finely enough into f_K, we can write:

$$B \cdot \sum_K f_{\phi K} \int_{\substack{\phi_{bin\,i} \\ \phi_{b\,bin\,K}}} d\phi_b \, d\phi_s \cdot \sum f_{\theta \ell} \int_{\substack{\theta_{bin\,j} \\ \theta_{b\,bin\,\ell}}} d\theta_b \, d\theta_s$$

$$= B \cdot \sum_K f_{\phi K} A_{\phi i K} \cdot \sum f_{\theta \ell} A_{\theta j \ell} \qquad (25)$$

$$= B \cdot \Delta\phi \, \Delta\theta \, G_{\phi i} \, G_{\theta j}$$

where $A\phi ik$ and $A\theta jl$ are little areas like those shown in figure 9b. They depend only on the beam and spectrometer cuts and, as can be seen from the figure, are easily calculated using simple geometry. Gj are defined to show explicitly the solid angle, $\Delta\theta\Delta\phi$, and can be thought of either as a flux correction or as solid angle correction. So equation 22 becomes:

$$Y_{ij} = \frac{\rho \ell N}{A} \, B \, \frac{d\sigma}{d\Omega}(\bar{t}_{ij}) \, G_{\phi i} \, G_{\theta j} \, \Delta\phi \, \Delta\theta \qquad (26)$$

We can now write $d\sigma/d\Omega$ in terms of the measured quantities: B, $f\theta$, $f\phi$, $\Delta\theta$, $\Delta\phi$, and Y and the calculated Gi, Gj:

$$\frac{d\sigma}{d\Omega}(\bar{t}_{ij}) = \frac{A}{\rho \ell N} \, \frac{Y_{ij}}{G_i \, G_j \, \Delta\theta \, \Delta\phi} \qquad (27)$$

We note that

$$\frac{d\sigma}{dt} = \frac{\pi}{p_b \, p_s} \, \frac{d\sigma}{d\Omega} \qquad (28)$$

3.3 CHOICE OF EVENTS

Not all events are suitable for inclusion in the yields, Y. Several kinds of cuts were made to the data. They are discussed below with their effect on the calculation of the cross section. If the same criteria for beam information is applied both to the scattering events and to the beam events used in calculating the beam phase space density, there is no effect on the final cross section. Only the total flux has to be corrected by the fraction rejected.

3.3.1 good beam reconstruction

Events with more than one track in any beam hodoscope, i.e. an ambiguous signature, were rejected. This eliminated events with more than one beam particle in the beam line (about 8 to 12%) and tracks in coincidence with noise in other elements of the same hodoscope. If any beam hodoscope had no signature (due to hodoscope inefficiency) that event was rejected. These requirements rejected over 60% of the events since the beam hodoscopes were noisy and not very efficient. Beam events outside beam angle and momentum cuts were also rejected. Clearly one could make gains by going beyond this simplest approach of requiring complete and unambiguous information for each event. There were no cuts on the beam x and y coordinates at the target, except those implied by the non-zero hodoscope signature requirement, and a hole counter in hardware veto.

3.3.2 good spectrometer trajectory

Sufficient unambiguous and non-zero wire chamber planes were required to completely decode ϕs, θs and Ps. If ϕs could not be calculated from the MWPC information, its determination from the focal plane hodoscope was used. Those events for which both MWPC and hodo information were available served to check that there was no systematic offset or scale difference between the two. Since there were several combinations of planes that could be used to calculate a given coordinate, and since each plane was fairly efficient (about 95%), the overall efficiency for the spectrometer decoding was usually about 95%. The yields were corrected for this on a run to run basis.

3.3.3 acceptance cut

Events falling outside the spectrometer's uniform acceptance region in angle or momentum were rejected. Consequently the efficiency for seeing an event at any angle or momentum was either 0 or 1, and no weighting of events according to their position in the aperture was necessary. The uniform acceptance region was determined by three separate methods, described below. All three results were consistent with $\phi s = \pm 1.4$mr, $\theta = \pm .75$mr, Ps = ±1.75%. The cuts in θs, ϕs, and Ps were made independently of each other and of any beam cuts.

Monte Carlo'ing events in a model of the spectrometer. We modified the TURTLE program [Carey 1971] to randomly choose trajectories uniformly from a phase space that totally covered the acceptance of the first quadrupole. TURTLE plotted the target coordinates of each trajectory not stopped anywhere along the spectrometer by magnet steel and passing inside each detector. The plot of a large number of such trajectories defines the uniform acceptance region. The x versus θ and y versus ϕ projections are shown in figure 10. TURTLE uses the same model for the spectrometer as TRANSPORT.

Mapping the various magnet and Cerenkov counter apertures back to the target. Each aperture was described by 4 lines: $x = \pm x^0$, $y = \pm y^0$, at the location of the aperture. These 4 lines were then transformed to lines of the form $x = a\theta + A$, $y = b\phi + B$, at the target, using the same transformation as used to reconstruct events, i.e. the TRANSPORT program model of the spectrometer. If these lines for all the apertures are plotted on the same plot, their envelope is the uniform acceptance region. See Butler [1975: p. 217] for a more complete discussion.

Looking at the cross section for narrowing acceptance cuts. Butler 1975 has calculated cross-sections for runs overlapping in angle for several values of the spectrometer cuts. In this way several cross-sections are calculated at the same t, but from different parts of the spectrometer. One then opens the cuts until cross-sections from the edges of the spectrometer fail to agree with those from the center.

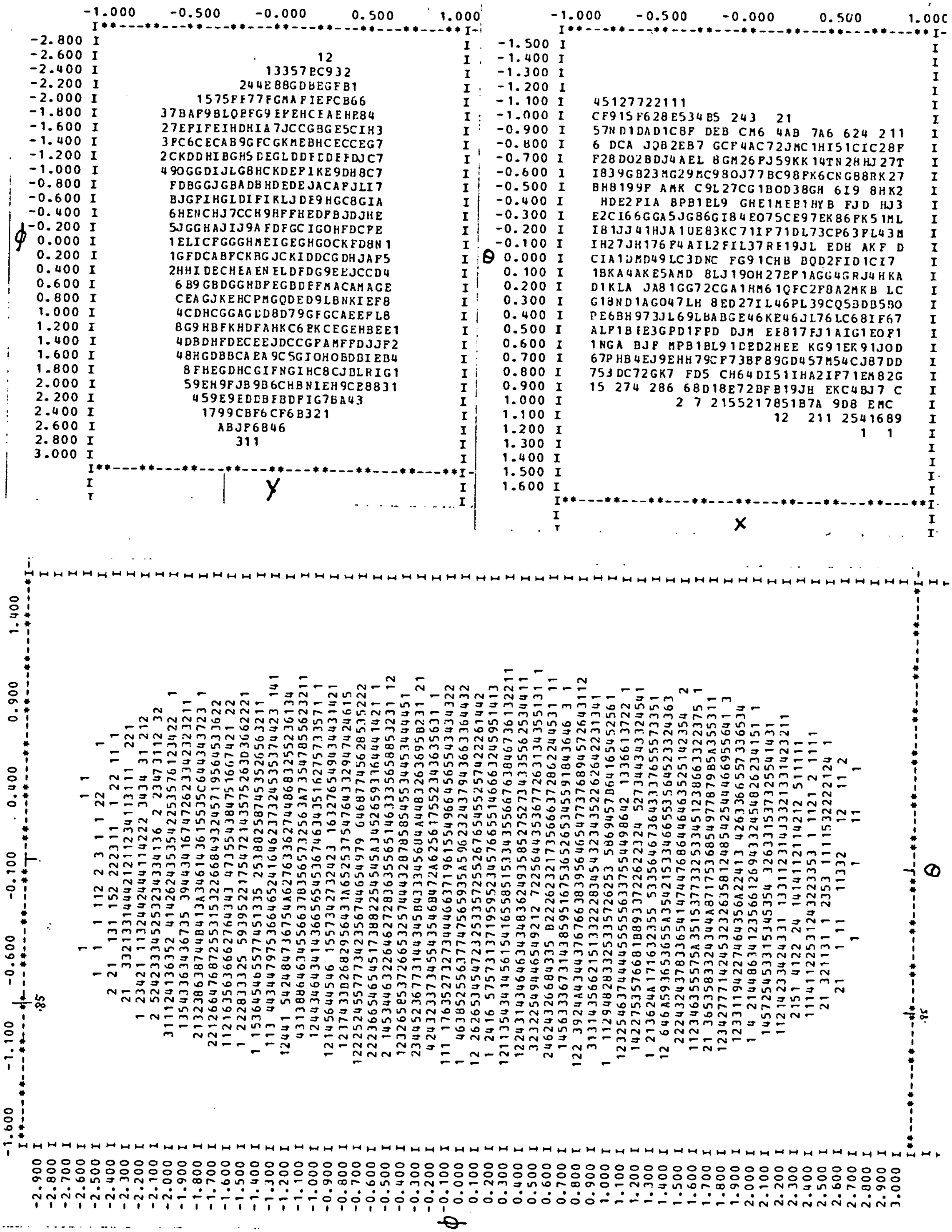

Figure 10: Spectrometer Acceptance, by Monte Carlo

3.3.4 missing mass cut

We wish to exclude from the yield Y any events where particles were produced. For each event the number

$$x^2 = -|t| + m^2 + 2m(Pb-Ps) \qquad (29)$$

is calculated (m = proton mass). For a hydrogen target this is the missing mass. With perfect t and momentum resolution elastic scattering events will have $x^2 = m^2 = .88\ (GeV/c)^2$. Figure 11 shows a plot of x^2 for a hydrogen target. The peak is broadened by the finite momentum resolution, $\Delta p/p = .13\%$. We accept all events with $x^2 \le 1.30\ (GeV/c)^2$. This includes some inelastic events, and loses some elastic events. Therefore a correction factor must be applied to the cross-section. Butler 1975 has estimated this correction (for this cut at 50 GeV) to be 1.01.

Deuterium target data is more complex; several types of scattering processes are possible. [The next chapter discusses this in detail.] We want to include all events except those where particles are produced. If the scatter was from a single constituent nucleon, x^2 is broadened by the Fermi motion of the target nucleon as well as the resolution. This broadening of x^2 was determined by a Monte Carlo calculation. [See figure 12].

The calculation used the Fermi momentum distribution derived from the Hulthen wave function. Adding the broadening ($\sigma = .04\ GeV^2$) in quadrature to the experimental resolution of $.12\ GeV^2$, we get a width of $.126\ GeV^2$. The calculation included only breakup single scattering by the deuteron. It is shown in the next chapter that the multiple scattering processes contribute upto 15% of the cross-section in the t range of this thesis. Since 1) their widths are small, 2) they are less than 15% of the cross-section,

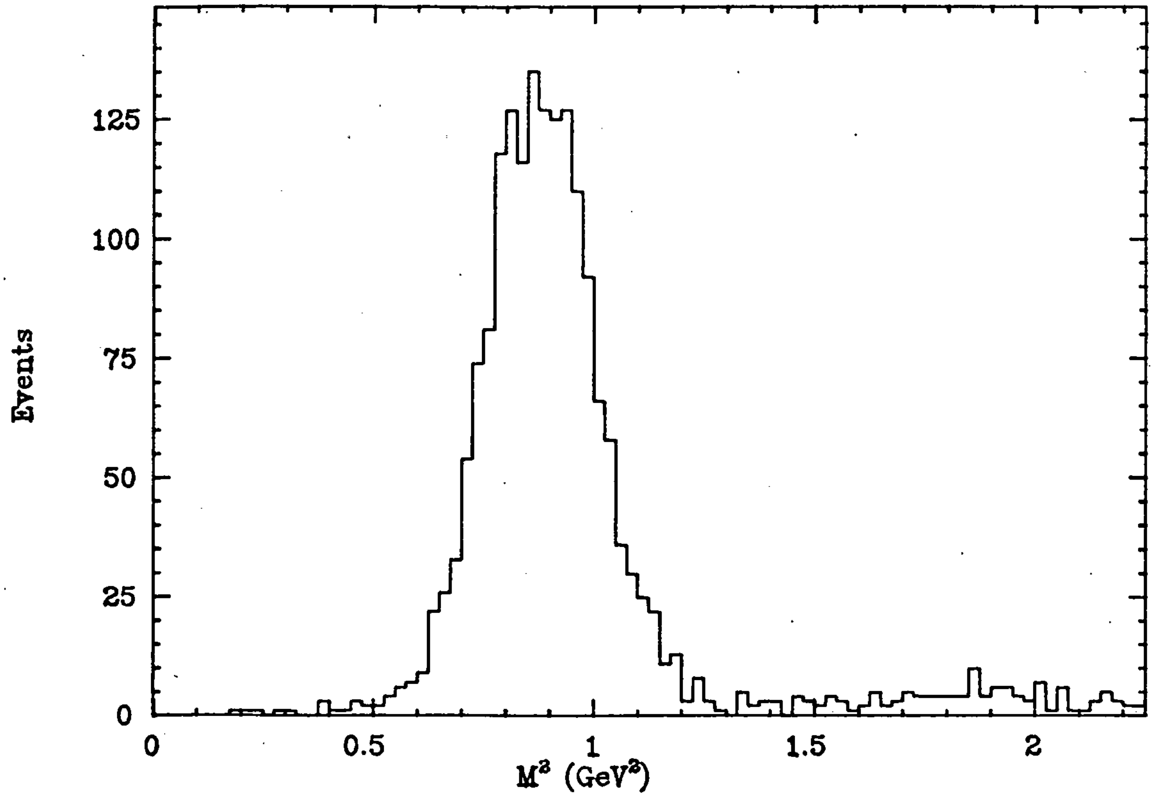

Figure 11: Missing Mass Plot (one run)

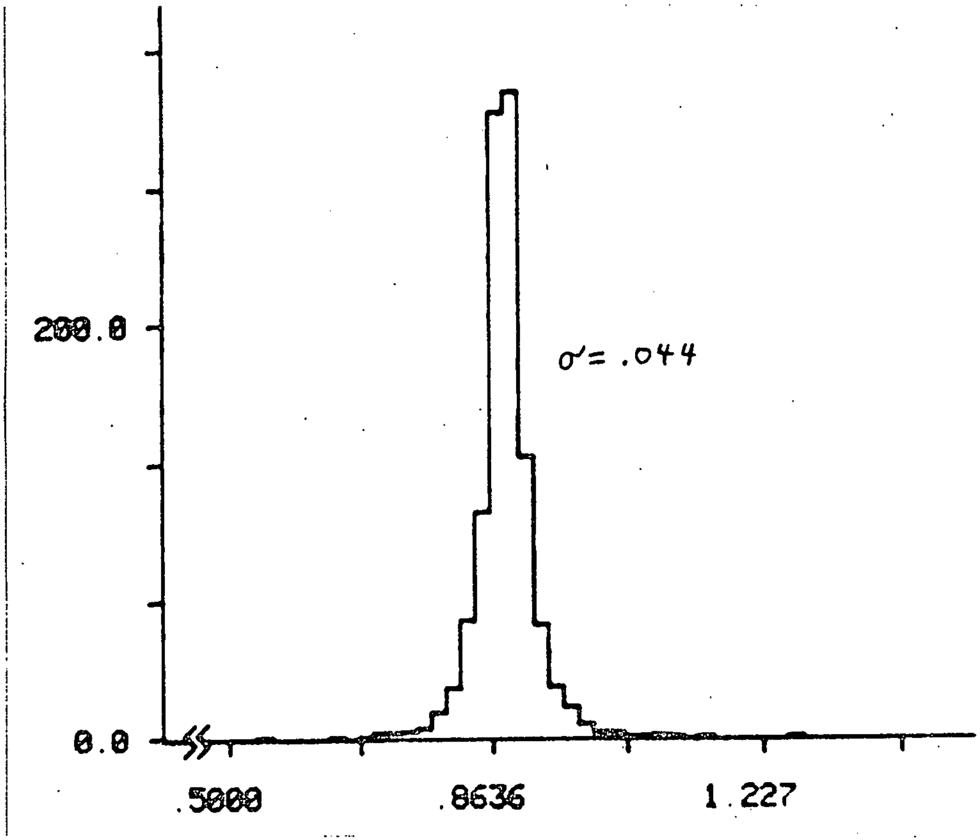

Figure 12: Fermi Broadening of Missing Mass Peak

and 3) they are centered at lower missing mass, the multiple scattering processes are assumed not to broaden the missing mass spectrum on the high side. See section 'The Momentum Loss Spectrum' below for details supporting this assumption.
If the recoil particle is not identified we do not know if the event was a breakup scatter or an elastic deuteron scatter. For the elastic case, $Pb-Ps = |t|/2M$, so $x^2 = m^2 - |t|(1-m/M)$ (M = deuteron mass), and these events have lower missing mass and therefore are contained by the cut.

Since the widths of the missing mass peak for hydrogen and deuterium targets are different, different correction factors should be applied for the same cut position. However, since 1) the cut is several standard deviations away from the peak, 2) the difference in widths is small, and 3) the correction factors are small, we have used the same cut and correction factor for both targets.

X^2, t, and Ps are not independent. Once a range for x^2 and for t (implied by the ranges of ϕ and ϵ) are chosen, equation 29 implies a range for Ps. The Ps cut must totally include this range (and be within th uniform momentum acceptance region), or events will be lost.

3.3.5 particle identification

There were 7 Cerenkov counters in the beam and spectrometer. Certain logical combinations of signals from these counters were allowed for each of the reactions studied. In all cases the beam particle identification criteria were very strict in order to minimize the contamination of the minority particles. [No correction to the cross section was required since the same criteria were applied to the beam events.] The spectrometer particle identification was less strict. Ambiguities in spectrometer particle identification were resolved by assuming identity with the beam particle. This is justified since the missing mass cut selects only elastic events at the 98% level and since the ambiguous signatures were only a small proportion. The matrix for Cerenkov signal possibilities, the assigned identifications, and a typical population (after missing mass cut and a hardware selection for good beam identification) for 50 GeV/c is shown in table 8. The reliability of the scheme was checked by examining the population numbers when the beam was run straight into the spectrometer with no target. The matrix for this case is shown in figure 8b. It shows that cross-talk between the various reaction channels is less than 1/2%.

Beam events. No particle identification criteria were used to select events for the beam phase space determination since analysis showed that the 1st and 2nd moments of θb, ϕb, and Pb did not depend on particle type. The increase in the number of beam events available reduced the random errors. However, the number of beam events with a particular beam particle identification was needed in the flux calculation.

Table 8.

Cerenkov signal and particle id assignments

	NONE	SGAS1	SGAS23	SG1.23	SDIFR	SGAS1 SDIFR	SG23 SDIFR	SG1.23 SDIFR
NONE	11.7 25.8	0 0	2.1 0	0 0	0 0	0 0	0 0	0 0
BGAS	0 0	0 0	0 0	0 0	0 0	0 0	0 0	0 0
DISC	ⓟ 1654 4734	6.4 9.4	ⓟ 353 157	0 1.7	5.4 6.0	0 0	.9 .85	0 0
BGAS.DISC	0 0	0 0	0 0	0 0	0 0	0 0	0 0	0 0
BDIFR	0 0	0 0	0 0	2.1 3.4	0 0	0 0	14 51	.9 .85
BGAS.DIFR	0 0	0 0	0 0	0 0	0 0	0 0	0 0	0 0
DISC.DIFR	3.2 8.5	0 0	0 0	0 .85	0 0	0 0	0 0	0 0
BG.DSC.DIFR	0 0	0 0	0 0	0 0	0 0	0 0	0 0	0 0
BDIFA	0 0	0 0	0 0	0 0	0 0	0 0	0 0	0 0
BGAS.DIFA	6.4 .85	17 0	253 .85	π 7274 4622	.9 0	0 0	0 2.6	π 78 33
DISC.DIfA	2.1 1.7	0 0	.9 0	0 0	0 0	0 0	0 0	0 0
BG.DSC.DIFA	.9 161	0 0	2.1 3.4	0 36	0 .85	0 0	0 0	0 .85
BDIFR.A	0 0	0 0	.9 0	0 2.6	0 0	0 0	K 184 102	.9 3
BGAS.DIFR.A	0 0	0 0	4.3 0	106 23	0 0	0 0	0 0	6.4 0
DISC.DIFR.A	0 1.7	0 .85	0 0	0 0	0 0	0 0	0 0	0 0
G.DSC.DFA.R	0 3.4	0 0	0 0	0 0	0 0	0 0	0 0	0 0

3.4 CALCULATION OF THE BEAM FLUX

The flux available for scattering with the above criteria applied to the beam particle is

$$B = (GBEV/BEV) \bullet BT \tag{30}$$

where:

BT is the number of beam particles of all kinds counted during the time the data acquisition system was ready to accept data and which did not have beam Cerenkov counter ambiguities detected by the fast electronics. BT does not include particles vetoed by the particle type countdowns.

BEV is the number of beam particles that were sampled as beam events.

GBEV is the number of beam events which 1) survived the same selection criteria as were applied to the beam particle in a scattering event, and 2) which had a beam particle of the type for the given reaction.

3.5 RANDOM ERRORS

From equation 27 we see that random errors in Y, B, and G will contribute to the uncertainty in $d\sigma/dt$. The relative error-squared of Y is 1/Y since the counts of Y are distributed according to a Poisson distribution. The relative error-squared of B, from equation 30, is 1/GBEV - 1/BEV. The negative sign is due to the fact that the good beam events are a sub-sample of all beam events and so the errors are correlated. We ignore the error in

BT since it is much smaller than the others. From equation 25 we can write the absolute error-squared of G as:

$$\begin{aligned}\Delta G_i^2 &= \Sigma_K A_{iK}^2 (\Delta f_K)^2 \\ &= \Sigma_K A_{iK}^2 (1/f_K N) f_K^2 \\ &= \Sigma_K A_{iK}^2 f_K/N\end{aligned} \qquad (31)$$

where N is the number of beam events used in determining the beam phase space. The relative error of $d\sigma/dt$ is the sum in quadrature of the separate errors.

$$\left(\frac{1}{GBEV} - \frac{1}{BEV} + \frac{\Delta G_i^2}{G_i^2} + \frac{\Delta G_j^2}{G_j^2}\right)^{1/2} \qquad (32)$$

Strictly speaking the N events are a subset of the BEV events and so there is a correlation and the error will be less than the above.

3.7 FINAL CORRECTIONS TO THE CROSS-SECTION

Several corrections can be applied to the cross-sections calculated above. Butler [1975] discusses them in detail. Since all except the empty target subtraction and transmission corrections are not made by the analysis in this thesis, we discuss here only enough to describe their nature and why they were not made.

Empty Target Subtraction

In order not to count in the cross-section events due to scattering in the target walls and other materials near the target, data was taken with an evacuated target cell which was otherwise identical to the full targets. The number of empty target events per unit beam flux times the hydrogen (deuterium) target flux was subtracted from the number of hydrogen (deuterium) target events. This correction was never more than 5% in the angle range for this thesis.

Transmission

Not all events scattering into the spectrometer's acceptance travel through all the spectrometer detectors to the last trigger counter. Some are 'absorbed', i.e. scattered inelastically by the hydrogen target or other materials along its path. Pions and kaons can also decay. The transmission corrections are measured by passing the beam straight into the spectrometer, for hydrogen, deuterium and empty targets. The pion transmission factor, for instance, is then given by the ratio of a scalers counting beam pions in coincidence with the spectrometer to one counting beam pions. The transmission for all three targets for all three beam particles is measured. The empty target cross-section is corrected by the empty target transmission before the empty target subtraction is made from the corrected full target cross-section. The transmission corrections for pions were: .834,.879, .787 for for hydrogen, deuterium, and empty targets and .795, .729 and .858 for protons.

Electromagnetic corrections

Coulomb as well as hadronic scattering can take place. The purely real Coulomb amplitude interferes with the hadronic amplitude and increases (for like charges) or decreases (for unlike) the cross-sections in the interference region. Coulomb scatering dominates at $t < .001$. At the low end of our t region, $t < .05$, the corrections were calculated as, for d, 1.3%, for p, 2.5%. The calculation followed that of Franco [1975], using a formalism suitable for hadron-nucleus scattering. It agreed numerically with the more traditional formalism of West [1968] and Foley [1969]. Assuming the deuteron cross-section is roughly twice the proton cross-section, we conclude that the pion-deuteron coulomb scattering is that due to the proton. When we 'subtract' the uncorrected proton from the deuteron cross-section to extract the neutron cross-section, we will automatically do this correction. The Coulomb correction has therefore not been made explicitly for these reasons.

The dominant radiative correction [Sogard 1974] is the momentum loss of the forward scattered particle due to photon emmision when the particle accelerates on approaching and leaving the interaction. Some events then appear to be inelastic. The correction is about 1% in our t range and is almost independent of the target particle. Hence it has been ignored.

Macroscopic Double Scattering

If the scattered particle interacts again downstream in the target, the observed scattering angle will be to 1st order, if both scatters are in the same plane, the sum of the two angles. The momentum transfer, t, is proportional to θ^2, however. At sufficiently large t, for a cross-section falling exponentially in t, the probability of two scatters at $\theta 1 + \theta 2 = \theta$ becomes larger than that for one scatter at θ. The contamination by double scattering was estimated by Monte Carlo and found to be atmost 3% for pd in our t range. It is roughly half this for pp. The cross-sections have not been corrected for this effect.

Chapter IV

THE MULTIPLE SCATTERING THEORY

4.1 INTRODUCTION

The naive first approximation to scattering from deuterons assumes the scattering to take place from one nucleon as if it were free with the other being a passive spectator. Since the cross-section has been found to differ significantly from this, the impulse approximation, Glauber & Franco, Harrington, West, and others[1] have gone beyond it. A list of possible corrections (most can't be calculated) can be found in West [1972: App. A]. The major corrections in this experiment are the multiple scattering terms. We are interested in two kinds of scattering: 1) elastic deuteron scattering, where the deuteron recoils in the final state, and 2) quasi-elastic or breakup scattering, where the deuteron's constituent nucleons become unbound and recoil, but there is still no resonance or particle production. At the energies and momentum resolution of this experiment these processes cannot be distinguished by measurements of the scattered particle only.

---

[1] Glauber 1955,1959, Franco & Glauber 1966,1967, Franco 1975, 1977, Wilkin 1966;
Harrington 1964;
West 1972, Atwood 1973, Landshoff 1977;
see Kolybasov 1973 for a bibliography

The multiple scattering theory amplitudes are often represented diagramatically as:

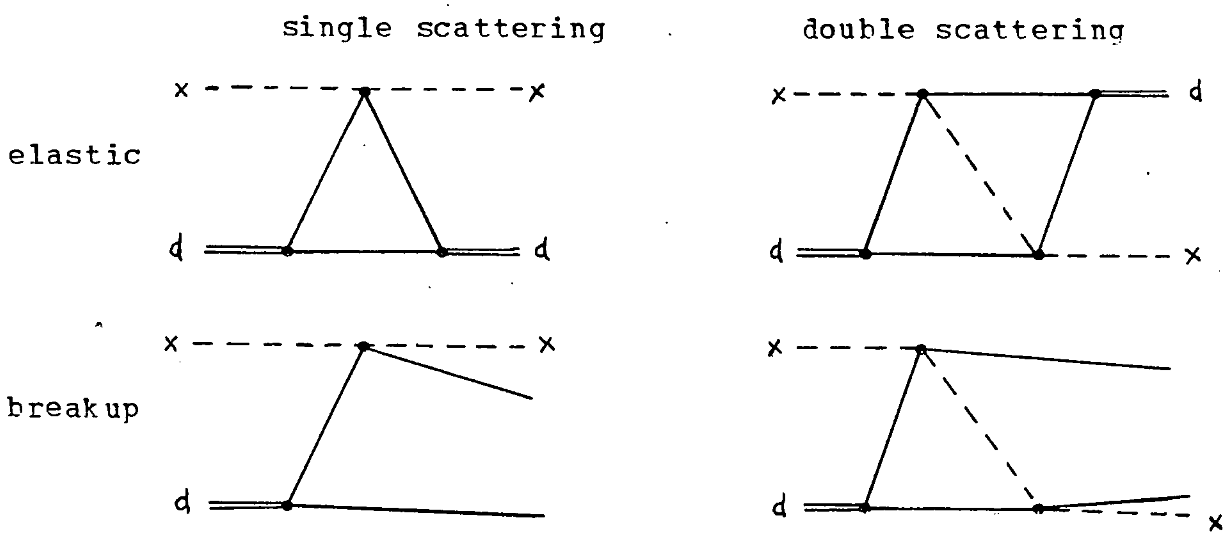

We give here a sketch of the derivation in Franco & Glauber 1966 of the multiple scattering theory of elastic and breakup scattering -- for the purpose of completeness, to define the terms, and in order to make plausible the main features of the theory. This theory expresses small angle high energy scattering from deuterons in terms of the nucleon elastic scattering amplitudes and the deuteron wave function. Kolybasov [1973] reviews the basic assumptions of the theory.

4.2 SKETCH OF THE DERIVATION

We begin with the eikonal approximation for the hadron-nucleon scattering amplitude, [see Glauber 1959 and Kolybasov 1973: sect. 7] and write

$$\Gamma(\vec{b}) = 1 - e^{i\chi(\vec{b})} = \frac{1}{2\pi i k}\int e^{-i\vec{q}\cdot\vec{b}} f(\vec{q})\, d^2\vec{q} \qquad (33)$$

where:

$\vec{b}$	is the impact parameter and is perpendicular to the incident beam direction
$\vec{q}$	is the 3-vector momentum transfer
k	is the magnitude of the incident momentum
$f(\vec{q})$	is the nucleon elastic scattering amplitude, i.e. $\lvert f(q)\rvert^2 = d\sigma/d\Omega(q)$.
$\chi(\vec{b})$	is the complex phase shift function
$\Gamma(\vec{b})$	is called the profile function

It can be shown for small angle scattering that the expressions in terms of laboratory coordinates are the same as those in center of momentum coordinates [Franco & Glauber 1966: App. B]. If the scattering angle is small, $\vec{q}$ is almost in the same plane as $\vec{b}$, and so the integration is over the plane perpendicular to the beam direction, instead over the sphere of possible $\vec{q}$'s. Also for small angles $t = -\lvert\vec{q}\rvert^2$. For a nucleon in a deuteron the off mass-shell scattering amplitudes should be used. But these are not known and since the nucleons are only weakly bound we use the on-shell amplitudes as would be measured in scattering from a free nucleon. It is also assumed that each nucleon acts independently on the incident particle and so the phase shifts for the two add. We then write the profile function for the deuteron as:

$$\begin{aligned}
\Gamma_d(\vec{b}) &= 1 - e^{i[\chi_p(\vec{b}+\frac{1}{2}\vec{s}) + \chi_n(\vec{b}-\frac{1}{2}\vec{s})]} \\
&= 1 - e^{i\chi_p(\vec{b}+\frac{1}{2}\vec{s})}\, e^{i\chi_n(\vec{b}-\frac{1}{2}\vec{s})} \\
&= 1 - \left(1 - \Gamma_p(\vec{b}+\tfrac{1}{2}\vec{s})\right)\left(1-\Gamma_n(\vec{b}-\tfrac{1}{2}\vec{s})\right) \qquad (34) \\
&= \Gamma_p(\vec{b}+\tfrac{1}{2}\vec{s}) + \Gamma_n(\vec{b}-\tfrac{1}{2}\vec{s}) - \Gamma_p(\vec{b}+\tfrac{1}{2}\vec{s})\,\Gamma_n(\vec{b}-\tfrac{1}{2}\vec{s})
\end{aligned}$$

where $\vec{s}$ is the projection along $\vec{b}$ of the relative position coordinate, $\vec{r}$, of the nucleons. At this point the deuteron profile function shows the impulse approximation terms plus a double scattering term. Γ_d depends on $\vec{r}$ through $\vec{s}$. So, in transforming from $\Gamma_d(\vec{b},\vec{s})$ to the deuteron amplitude, $F(\vec{q})$, we must average over all deuteron states, i.e. we use

$$\langle \Gamma_d \rangle = \langle f | \Gamma_d(\vec{b},\vec{s}) | i \rangle = \int \phi^*(\vec{r}) \Gamma_d(\vec{b},\vec{s}) \phi(\vec{r}) \; d^3\vec{r} \tag{35}$$

where $|i\rangle$ and $|f\rangle$ are the initial and final states of the deuteron and $\phi(\vec{r}) = \langle \vec{r} | \phi \rangle$ is the deuteron wave function. Then

$$\begin{aligned} F_{fi}(\vec{q}) &= \frac{iK}{2\pi} \int e^{i\vec{q}\cdot\vec{b}} \langle f | \Gamma_b + \Gamma_n - \Gamma_p \Gamma_n | i \rangle \, d^2\vec{b} \\ &= \langle f | F | i \rangle \end{aligned} \tag{36}$$

For elastic scattering $|i\rangle = |f\rangle = |\phi\rangle$. After some manipulation [Franco & Glauber 1966] we get:

$$\begin{aligned} F_{ii}(\vec{q}) = {} & S(\vec{q}/2) \left[f_n(\vec{q}) + f_p(\vec{q}) \right] \\ & + \frac{i}{2\pi K} \int S(\vec{q}) f_n(\overrightarrow{\tfrac{q}{2}+q'}) f_p(\overrightarrow{\tfrac{q}{2}-q'}) \, d^2\vec{q}\,' \end{aligned} \tag{37}$$

where $S(\vec{q}) = \int e^{i\vec{q}\cdot\vec{r}} |\phi(\vec{r})|^2 \, d^3\vec{r}$, the deuteron form factor. There is a single scattering term and a double scattering term, so the elastic cross-section $|\langle i|F|i\rangle|^2 = |F_{ii}|^2$ will have an interference term:

$$\begin{aligned} \frac{d\sigma}{d\Omega}\Big|_{el}(\vec{q}) = {} & S^2(\tfrac{q}{2}) \left\{ |f_n(\vec{q})|^2 + |f_p(\vec{q})|^2 + 2\,\mathrm{Re}\!: f_n^* f_p(\vec{q}) \right\} \\ & \frac{-1}{\pi K} S(\tfrac{\vec{q}}{2})\, \mathrm{Im}\!: \left\{ \left[f_n^*(\vec{q}) + f_p^*(\vec{q}) \right] \cdot \int S(q') f_n(\overrightarrow{\tfrac{q}{2}+q'}) f_p(\overrightarrow{\tfrac{q}{2}-q'}) \, d^2\vec{q}\,' \right\} \\ & + \frac{1}{(2\pi K)^2} \left| \int S(\vec{q}\,') f_n(\overrightarrow{\tfrac{q}{2}+q'}) f_p(\overrightarrow{\tfrac{q}{2}-q'}) \, d^2\vec{q}\,' \right|^2 \end{aligned} \tag{38}$$

These three terms will be refered to as elastic single scatering, elastic single-double interference, and elastic double scattering: ESS, ESD, EDD respectively.

The cross-section for scattering into some particular final state $|f\rangle$ is $|\langle f|F|i\rangle|^2 = \langle i|F^*|f\rangle\langle f|F|i\rangle$. If we sum over a complete set of final states we can use the completeness relation $\sum_f |f\rangle\langle f| = 1$. This is true if we ignore the energy differences of the final states $|f\rangle$, i.e. we ignore the recoil kinetic energy (which is small for small angle scattering) and whether the deuteron is bound or broken up. Then we have

$$\frac{d\sigma}{d\Omega}(\vec{q})\Big|_{sc} = \langle i\,|\,F^*F\,|\,i\rangle \qquad \text{c.f.} \tag{39}$$

which we write out fully as

$$\begin{aligned}\frac{d\sigma}{d\Omega}(q)\Big|_{sc} = {} & |f_n(\vec{q})|^2 + |f_p(\vec{q})|^2 + 2S(\vec{q})\,\mathrm{Re}:\{f_n^* f_p(q)\} \\ & -\frac{1}{\pi K}\,\mathrm{Im}:\Big\{f_n^*(q)\int S(\vec{q}\,'-\tfrac{q}{2})\,f_n(\tfrac{q}{2}+q')\,f_p(\tfrac{q}{2}-q')\,d^2\vec{q}\,' + \text{term } n\leftrightarrow p \\ & +\frac{1}{(2\pi K)^2}\int f_n^*(\tfrac{q}{2}+q')\,f^*(\tfrac{q}{2}-q')\end{aligned} \tag{40}$$

These three terms will be refered to as single scattering, single-double interference, and double scattering: SS, SD, DD respectively. Note that they include both elastic and breakup processes because of the completeness relation.

Figures 13 - 19 are plots of terms in equations 38 and 40 for a 50 GeV/c proton beam using $fp = fn = A(i+\rho)\exp(-bq^2)$. [Where ρ is the usual ratio of the real to the imaginary part.] We used the tabulated charge form factor derived from the Reid soft-core potential by Greben [1970]. For elastic scattering, the terms containing the quadrupole form factor are not included. The form factor is discussed in more detail below. Note that $S(\vec{q}) = S(-\vec{q}) = S(q)$ and $S(0) = 1$.

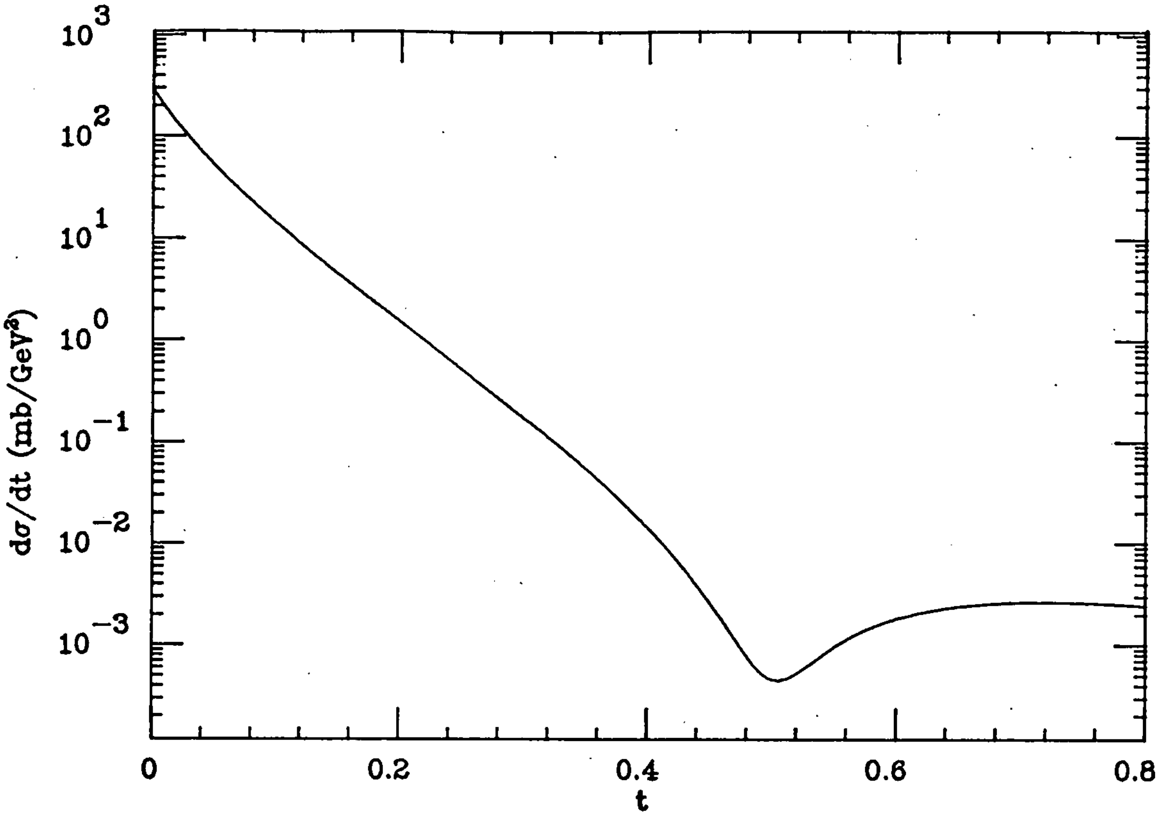

Figure 13: Elastic Deuterium Scattering

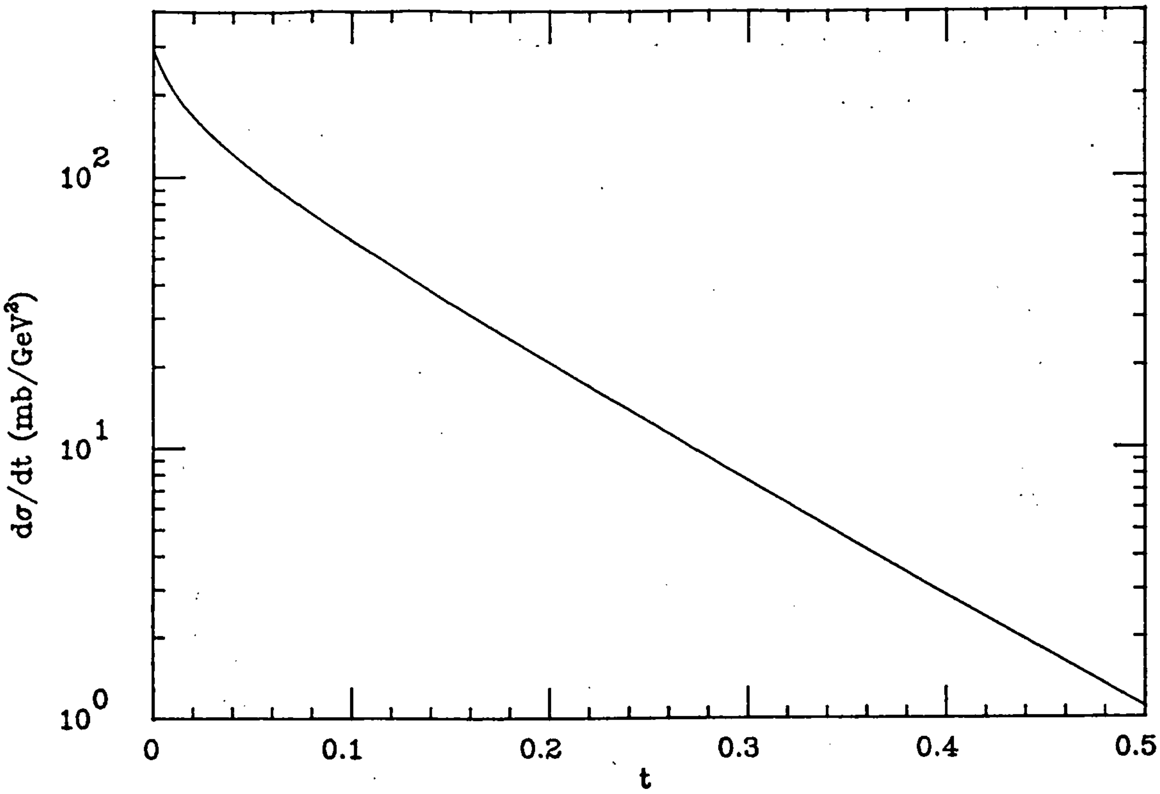

Figure 14: Elastic plus Breakup Scattering

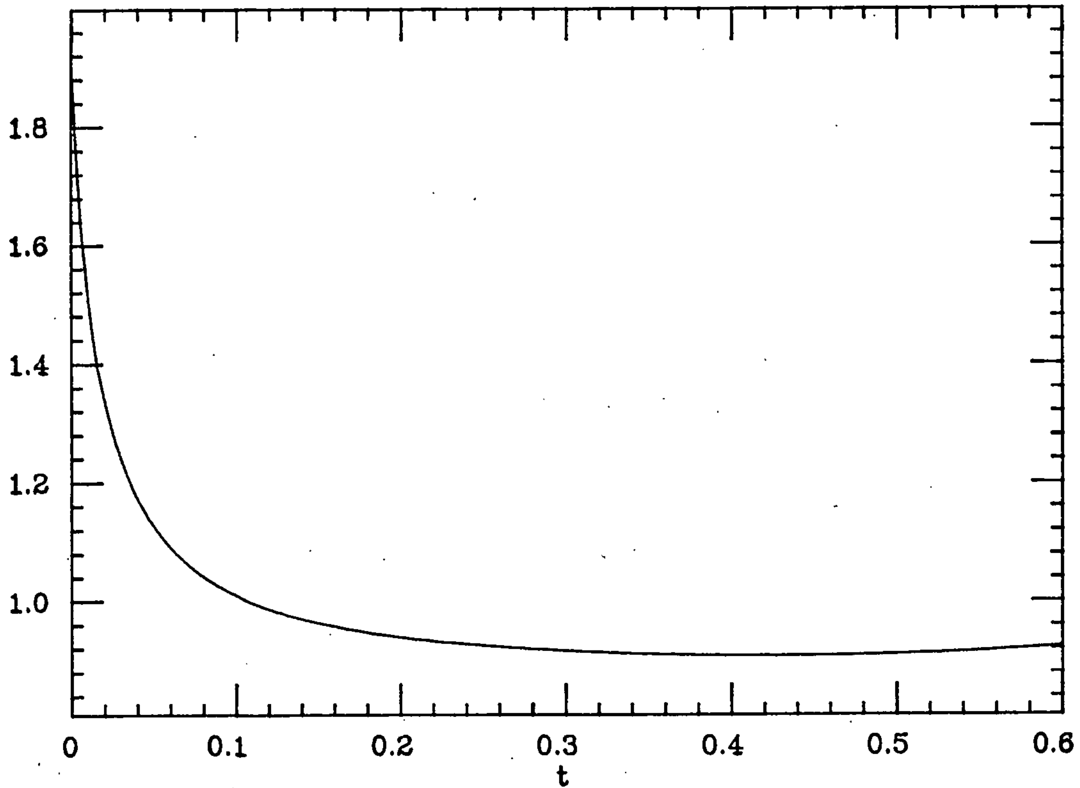

Figure 15: (Elastic + Breakup)/(2•Free Nucleon Scattering)

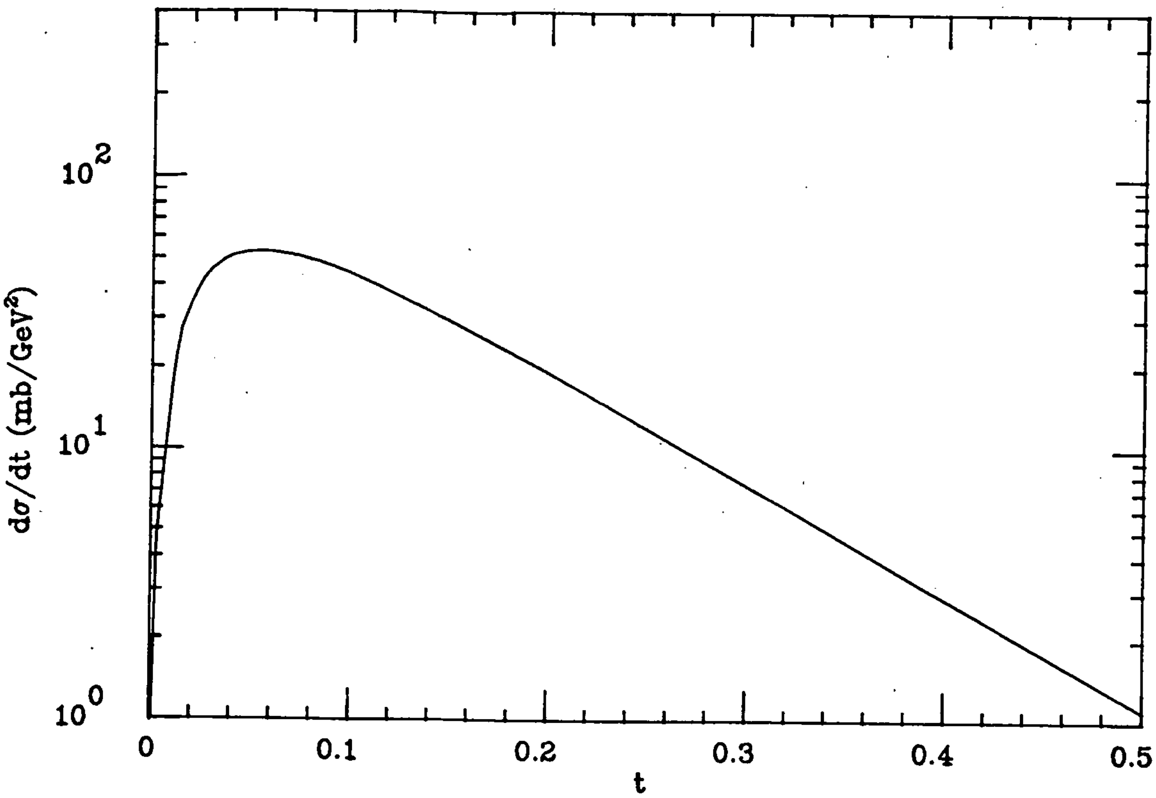

Figure 16: Breakup only scattering

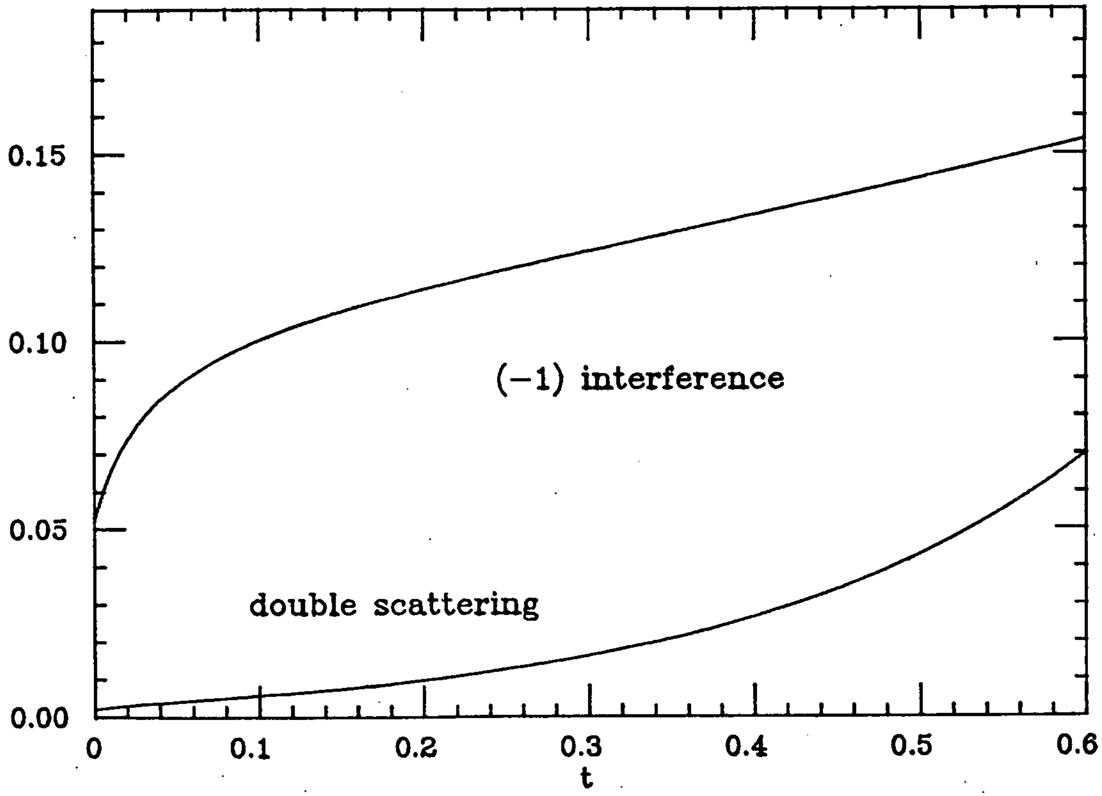

Figure 17: Ratio of Multiple to Single Scattering terms

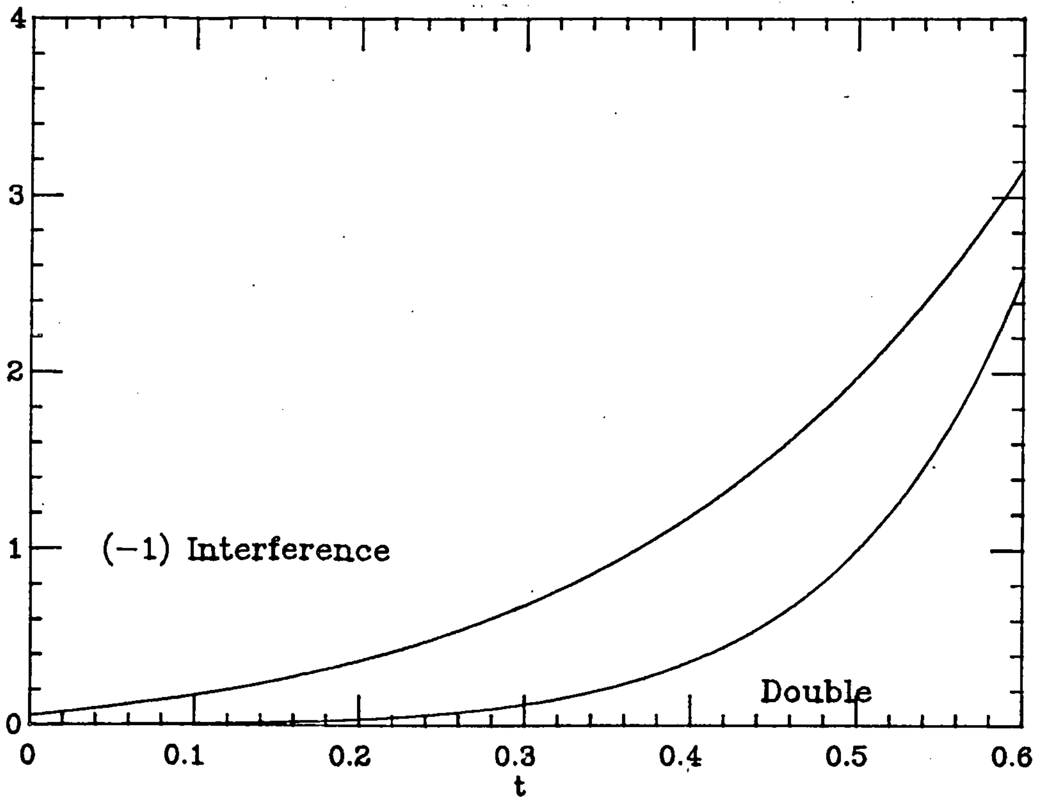

Figure 18: Ratio of Multiple to Single Scattering (elastic)

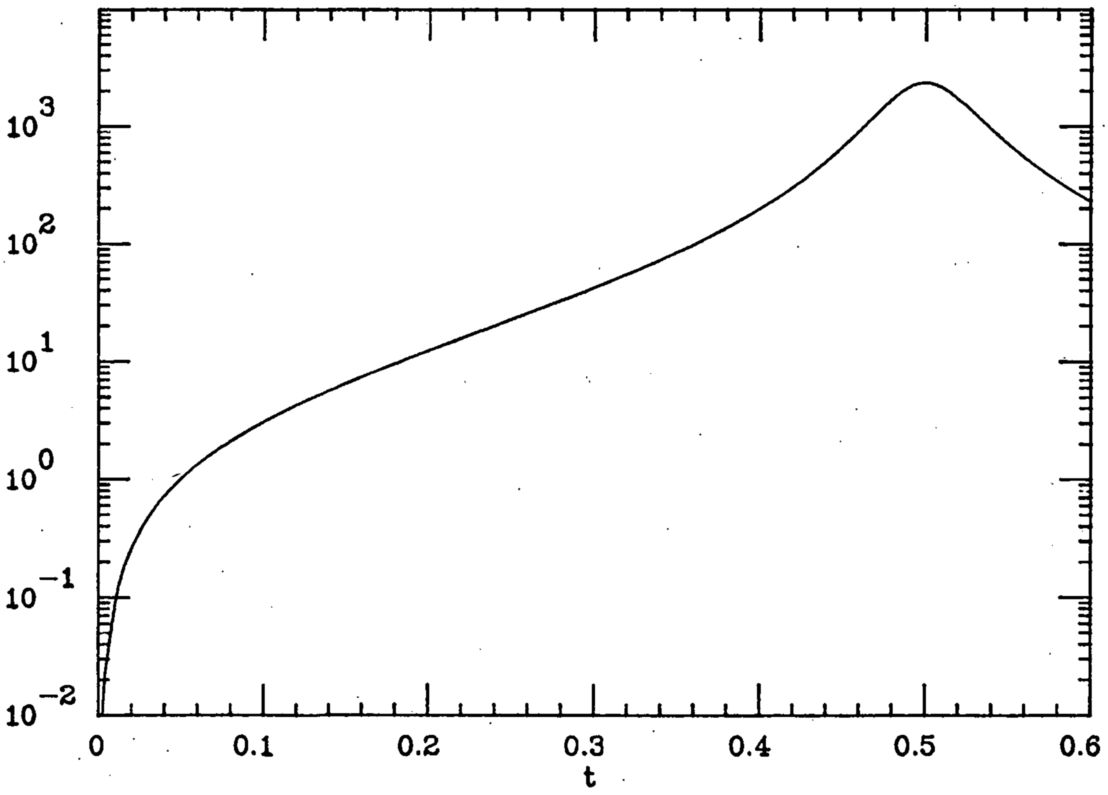

Figure 19: Ratio of Breakup to Elastic Scattering

4.3 FEATURES OF THE MULTIPLE SCATTERING THEORY

4.3.1 The single scattering terms

The gross difference between the elastic and the elastic plus breakup cross-sections, is the role of the form factor. The single scattering term for elastic scattering in the approximation of equal neutron and proton amplitudes is

$$4\ S^2(q/2)\ |f(q)|^2$$

whereas for elastic and breakup, it is:

$$2\ |f(q)|^2\ (1+S(q))$$

S(q) falls very quickly with q (see figure 20) much more quickly than the nucleon cross-sections, so the elastic differential cross-section is dominated by $S^2(q/2)$. This also means the shape of the elastic differential cross-section is very sensitive to S(q) and hence to our model of the deuteron wave function. On the other hand, for the elastic plus breakup cross-section, the (1+S(q)) factor is much less sensitive to the details of the form factor. Details of the choice of form factor are discussed below.

4.3.2 The effects of the interference and double scattering terms

At high energies the nucleon elastic scattering amplitude is mainly imaginary. Then the single-double interference terms (SD and ESD) will be negative and the double scattering terms positive. If both the nucleon amplitudes are approximated by Ae^{-bt}, then, roughly, the single scattering term will go as e^{-2bt}, the interference term as $e^{-\frac{3}{2}bt}$, and the double scattering term as

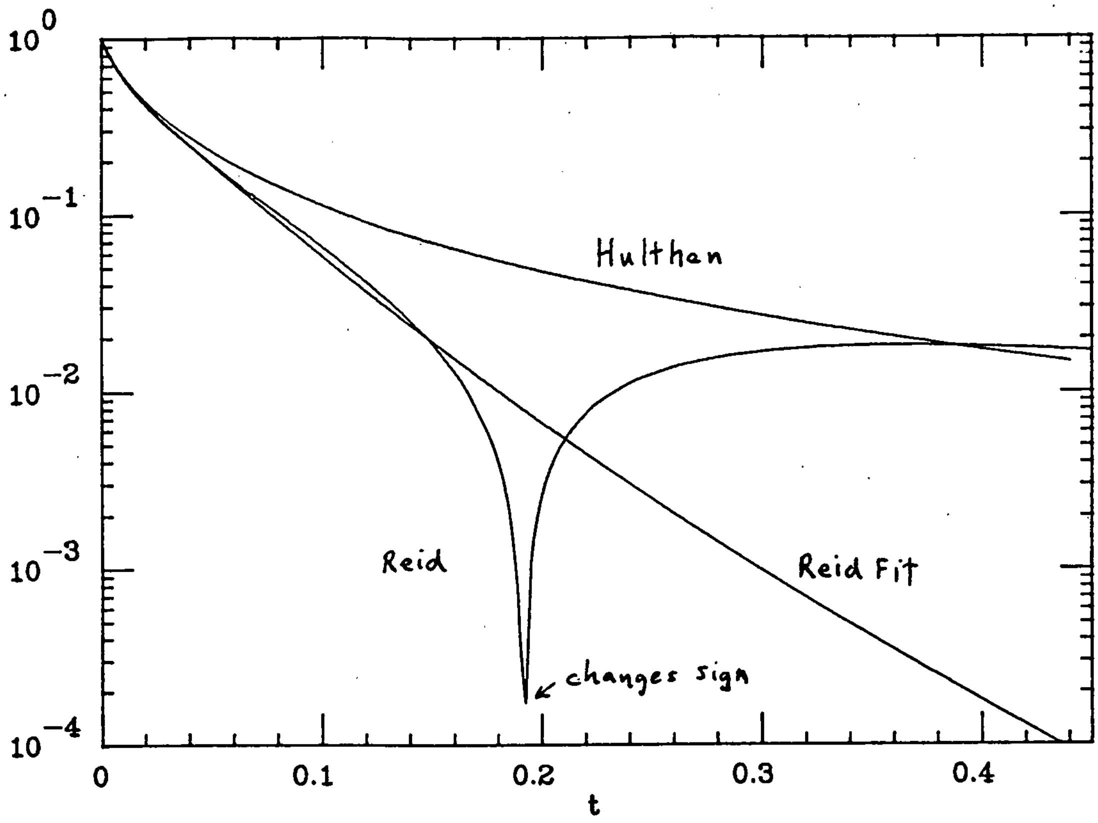

Figure 20: Deuteron Form Factors

e^{-bt}. This means that DD and EDD will dominate at large |t|, and SS and ESS at small |t|. The interference terms will be important in between the two t regions. See figures 13 - 19.

For elastic scattering, the interference term causes a dip in the cross-section - in fact a zero for a purely imaginary nucleon scattering amplitude. However the 6% D-wave component causes this dip to move slightly in t for different states of the initial and final deuteron spins. [Because single scattering is not possible for certain initial and final spin combinations.] If the target deuterons are unpolarized and the recoil deuteron polarizations are not measured, the dip is washed out by the average over initial states and sum over final states. See Franco 1969.

For breakup plus elastic scattering, if only a particular recoil state was detected, the differential cross-section for scattering into that state would have a dip, but since we sum over all final states incoherently (they are distinguishable) the dip is washed out even in a theory without a D-wave component.

The figures show that the SD and DD terms together are less than a 15% correction to the impulse approximation over the t range of this experiment [.05 < |t| < .5].

4.3.3 The form factor in the integrands

An important consideration is that the form factor behaves much like a delta-function when it appears in an integrand because it is so sharply peaked in the forward direction. Its details at large q^2 are not important to the value of the integral. This allows us to use a sum-of-exponentials fit to the deuteron form factor - optimized for small q^2 - in integrands. This allows the SD integral to be done analytically.

4.3.4 Flux factors

The 1/k and $1/k^2$ factors do not lessen the contributions of the multiple scattering terms as the momentum increases, as it might appear. Since

$$\frac{d\sigma}{d\Omega} = \frac{\pi}{K^2} \frac{d\sigma}{dt} \tag{41}$$

we can write equations 38 and 40 in terms of invariant amplitudes g such that

$$\frac{d\sigma}{d\Omega} = |g|^2 \quad \text{and} \quad g(t=-q^2) = \frac{\sqrt{\pi}}{K} f(q) \tag{42}$$

The resulting cross-section will not have any relative momentum dependence in its terms.

4.3.5 Origins of the interference terms

Note that there are two kinds of interference terms: 1) neutron-proton interference in a single scattering and 2) single-double scattering interference. Why are there interference terms at all? Clearly there is interference in elastic scattering: we cannot tell whether the neutron or proton was struck (the interference term in ESS), or whether one or both nucleons were struck (the ESD interference term). But in breakup reactions are we not capable of detecting whether the neutron or proton or both recoil? If so, there should not be interference terms. At the moment of impact, the Fermi momentum may be opposite the momentum transfer q and such that the target nucleon then stops; the spectator then appears to be recoiling with momentum -q. This is an extreme case but well illustrates that the Fermi momentum makes separating the alternatives uncertain when the momentum transfer q is small. Hence the neutron-proton interference term is present in single breakup scattering. Its importance diminishes as q increases because it is multiplied by S(q). Similarly, if we see two nucleons recoiling slowly, we cannot tell whether there was a double scatter or whether one of the nucleons is moving by virtue of the Fermi motion.

4.3.6 Charge independence

Wilkin 1966 and Glauber 1967 have pointed out that the theory so far considered violates charge independence. If we require the incident particle to keep its charge, the only way charge exchange processes can contribute is in double scattering where both scatters have charge exchange. Since charge exchange cross-sections at the energy of this experiment are less than 3% of the elastic cross-sections, these diagrams have been ignored here.

4.3.7 The usefulness of breakup single scattering

Figures 19 and 17 show that in the t range of this experiment, the dominant process is breakup single scattering. This is particularly advantageous for extracting a neutron cross-section for two reasons:

1) the breakup expressions are insensitive to the details of the deuteron wave function, i.e. S(q) as mentioned above.
2) breakup double scattering usually results in the two recoiling nucleons being very close in momentum. One therefore expects final state corrections (e.g. pion exchange between the two nucleons) to become important. In single scattering, one can picture one nucleon cleanly knocked out of the deuterons and the other a spectator.

The fact that single scattering dominates means, however, that this t range is not a good range in which to test the Multiple Scattering Theory.

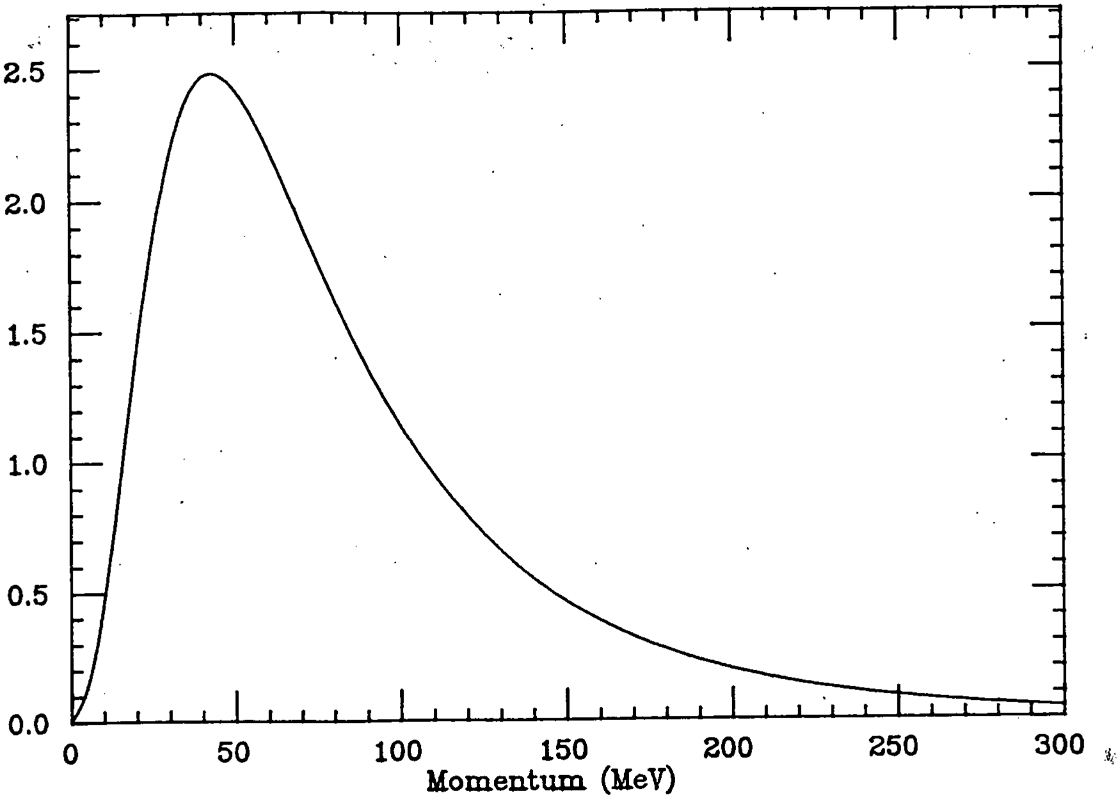

Figure 21: Fermi Momentum Distribution for Hulthen Potential

This is the location of the most probable momentum loss, i.e. the location of the peak. Glauber et al. 1971 express the spectrum as a one sided exponential, $e^{-a(\Delta p - \Delta p_d)}$, starting at $\Delta p_d = |t|/2m$ and decaying to larger losses with $a = 2bm$. [b = logarithmic slope of nucleon cross-section at q/2; m = nucleon mass] (Actually 2bm is the first term of a power series.) Figure 22 illustrates the scattered particle's momentum spectrum.

Since 2m-M = 2MeV, the elastic and double scattering peaks are not resolved at our incident energies. Whether or not the double and single scattering peaks are resolved depends on t, the experimental momentum resolution, and the contribution of the interference spectrum which lies between the single and double scat-

With perfect resolution the elastic peak is a delta function.

For breakup single scattering, $\vec{P}_2$ is given by the deuteron Fermi momentum distribution. So if we average over all deuteron states and use the fact that $\vec{P}_2$ is isotropic in the lab, we get the expected value of the momentum loss as:

$$\langle \Delta P_s \rangle = \frac{|t|}{2m} \tag{45}$$

The shape is essentially that of the Fermi momentum, $\vec{p}_2$, distribution (see figure 21). Spectrum calculations have been done by Straumann & Wilkin 1970, Glauber, Kofoed-Hanson & Margolis 1971, and Kofoed-Hanson 1972. Glauber et al. 1971 have found a width

$$\sigma^2 = \frac{|t|}{2m}\,\frac{\gamma^2}{m} \tag{47}$$

using a gaussian deuteron form factor:

$$S(q) = e^{-q^2/4\gamma^2} \qquad \frac{1}{4\gamma^2} \approx 66\,(GeV/c)^2 \tag{48}$$

They also calculate the spectrum of the interference term, and find it centered between the single and double scattering spectrum. The results of a Monte Carlo calculation using the Hulthen momentum distribution are shown in figure 12, in section 3.3.4.

For breakup double scattering we have $\Delta p_d = (\Delta p)_1 + (\Delta p)_2$. If we are measuring at a fixed angle ϵ, the most probable double scattering process is two scatters in the same plane, each with $\theta/2$. Then for scatters 1 and 2:

$$t_1 = -P_1 P_3 (\theta/2)^2 \qquad t_2 = -P_3 P_5 (\theta/2)^2 \qquad P_1 \approx P_3 \approx P_5$$

So

$$\Delta P_d = 2\,(t/4)\,/\,(2m) = |t|\,/\,4m \tag{49}$$

4.4 THE MOMENTUM LOSS SPECTRUM

Inelastic - i.e. resonance and particle production - events are rejected from the data used in this thesis by requiring that the quantity

$$-|t| + m^2 + 2m(Pb-Ps) \qquad m = \text{proton mass}$$

be less than some value. See section 3.3.4. [For a hydrogen target this quantity is the missing mass.] Since this calculation uses the scattered particle's momentum, Ps, it is necessary to know its distribution for the various processes. We want to be sure we do not lose breakup events when we make this cut.

We can get a rough idea of the momentum spectrum of the scattered particle for a fixed angle by considering elastic deuteron scattering at angle θ, breakup single scattering at θ, and breakup double scattering with the two scatterings each at θ/2. We write:

$$P_4{}^2 = (P_1 + P_2 - P_3)^2 \qquad \text{four vectors}$$

$$P_4{}^2 = (P_1 - P_3)^2 + m_T{}^2 + 2P_2(P_1 - P_3) \qquad \text{four vectors}$$

$$= -|t| + m_T{}^2 + 2E_2(E_1 - E_3) - 2P_2 \bullet (P_1 - P_3)$$

For elastic scattering $P_4{}^2 = m_T{}^2$, the mass of the target particle; for high energies $E_1 - E_3 = P_1 - P_3$. So, the laboratory momentum loss is

$$\Delta P = P_1 - P_3 = \frac{|t| + 2\vec{P_2} \cdot (\vec{P_1} - \vec{P_3})}{2E_2} \qquad (43)$$

<u>For elastic deuteron scattering</u> $\vec{P_2} = 0$, $E_2 = M$, the deuteron mass since the deuteron is at rest in the lab. So

$$\Delta P_{el} = \frac{|t|}{2M} \qquad (44)$$

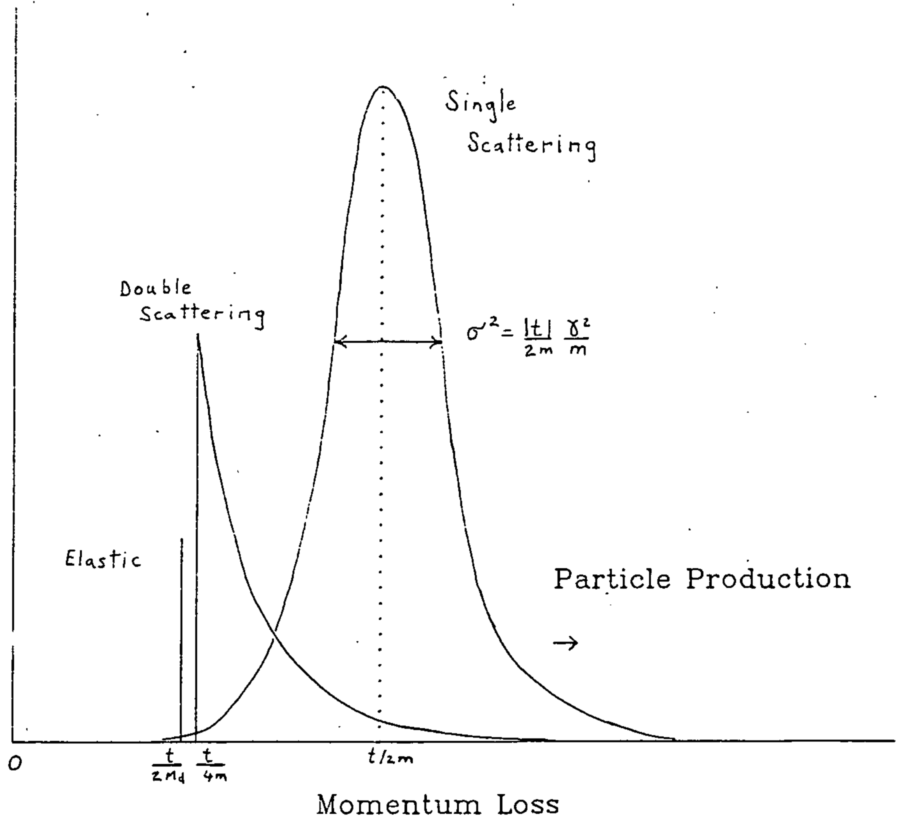

Figure 22: Features of the Momentum Loss Spectrum

tering peaks. Ignoring all but the t dependence, the peaks are just separated when

$$\sqrt{\frac{|t|}{2m}\frac{\gamma^2}{m} + \frac{1}{2bm}} = \left(\frac{|t|}{2m} - \frac{|t|}{4m}\right) \qquad (50)$$

implying t =.25; they continue to move apart as t increases. With an experimental resolution of $\Delta p/p$ = .13% the peaks are not resolved over most of the t range of this experiment. (They were resolved however, by Allaby 1969 and Amaldi 1972, at lower incident momentum and higher $|t|$.) This experiment therefore cannot distinguish between the single and double scattering peaks nor between elastic and breakup events on the basis of the scattered particle's momentum alone.

4.5 THE DEUTERON SPIN AND FORM FACTOR

4.5.1 The theory with spin

The deuteron is observed to have spin J=1 and parity P=+1. Since $P=(-1)^L$, the relative orbital angular momentum L must be even, i.e. L=0,2,4... . Two nucleons of spin 1/2 can be combined to give total spin S=0 or 1. S=0 is ruled out since J=L+S. We are left with S=1 and L=0 or 2. The observed non-zero quadrupole moment of the deuteron requires some L=2 component and its magnitude indicates a 6 to 7% component. What effect does this L=2 state have on the scattering process - for incident spinless particles (pions and kaons) and even for spin 1/2 protons whose nucleon spin flip amplitudes are very small?

For elastic scattering, the matrix element of the scattering operator <i|F|i> becomes <im'|F|im>, where the index m (m') indicates the deuteron's initial (final) spin projection along some axis; m=-1,0,+1, and where F, given by equation 36, has both a single and double scattering term. The cross-section is then:

$$\left.\frac{d\sigma}{d\Omega}\right|_{el\ m'm} = |\langle im'|F|im\rangle|^2 \qquad (51)$$

The result has been worked out in the literature [Franco 1969, Sidhu 1973, Michael 1969, Fridman 1974]. If the target deuterons are not polarized, and the recoil deuteron polarization is not measured:

$$\left.\frac{d\sigma}{d\Omega}\right|_{el} = 1/3 \sum_{m'} \sum_{m} |\langle im'|F|im\rangle|^2 \qquad (52)$$

The result is expressed in terms of a spherical form factor, S (q) and a quadrupole form factor S (q):

$$S_0(q) = \int (u^2+v^2)\, j_0(qr)\ dr$$

$$S_2(q) = \int (2vu - 2v^2)\, j_2(qr)\ dr \,/\sqrt{2} \qquad (53)$$

where u and v are the radial parts of the L=0 and L=2 terms of the deuteron wave function:

$$\frac{d\sigma}{d\Omega}\bigg|_{el} = \left|a(S_0) + b(S_0)\right|^2 + \frac{3}{4}\left|a(S_2)\right|^2 + \frac{1}{4}\left|a(S_2) + b(S_2)\right|^2 \quad (54)$$

where

$$a(S) = \left[f_n(\vec{q}) + f_p(\vec{q})\right] S\left(\frac{\vec{q}}{2}\right)$$

$$b(S) = \frac{i}{2\pi K} f_n\left(\frac{q}{2} + q'\right) f_p\left(\frac{q}{2} - q'\right) S(\vec{q}\,') \; d^2\vec{q}\,' \quad (55)$$

The elastic plus breakup cross-section is calculated here with these same assumptions.

$$\frac{d\sigma}{d\Omega}\bigg|_{sc\ m'm} = \sum_f |\langle fm'|F|im\rangle|^2 \quad (56)$$

The derivation, ignoring the deuteron spin, invoked closure at this point, i.e. $\sum_f |f\rangle\langle f| = 1$, in order to avoid writing wave functions for all possible states of recoiling nucleons from this broken deuteron. Clearly this would be even more complicated a task if the spin and angular momentum states are to be included as well. However, closure can be invoked again if we extend the sum over m' as well as f. Then

$$\frac{d\sigma}{d\Omega}\bigg|_{sc\ m} = \sum_{m'f} \langle im|F^*|fm'\rangle\langle fm'|F|im\rangle \quad (57)$$

$$= \langle im|F^*F|im\rangle$$

If we average over initial deuteron states we have the situation of this experiment - unpolarized target deuterons and no measurement or identification of the recoiling state at all. Then

$$\frac{d\sigma}{d\Omega}\bigg|_{sc\ m} = 1/3 \sum_m \langle im|F^*F|im\rangle \quad (58)$$

we examine first the single scattering term of the F*F product. From equation 36

$$F(q) = e^{i\frac{\vec{q}\cdot\vec{r}}{2}} f_n(q) + e^{-i\frac{\vec{q}\cdot\vec{r}}{2}} f_p(q) + \frac{i}{\pi K}\int e^{i\vec{q}'\cdot\vec{r}} f_n(\tfrac{q}{2}+q')\, f_p(\tfrac{q}{2}-q')\, d^2\vec{q}' \qquad (59)$$

so the single scattering terms are

$$\begin{aligned} &\langle im|\,\left|e^{i\frac{\vec{q}\cdot\vec{r}}{2}} f_n(q) + e^{-i\frac{\vec{q}\cdot\vec{r}}{2}} f_p(q)\right|\,|im\rangle \\ &= \langle im|\,|f_n|^2 + |f_p|^2 + e^{-iq\cdot r} f_n f_p^* \, e^{+iqr} f_p f_n^* \,|im\rangle \\ &= \langle\, |f_n|^2 + |f_p|^2 + 2\,\mathrm{Re}:\, f_n^* f_p \,\langle im|\, e^{i\vec{q}\cdot\vec{r}}\,|im\rangle \end{aligned} \qquad (60)$$

The 3 matrix elements $\langle im|\,e^{+i\vec{q}\cdot\vec{r}}\,|im\rangle$ have been calculated in the literature for elastic scattering. They are (see especially Fridman 1974):

$$\begin{aligned} \text{for } m &= +1 & S_0(q) &- 1/\sqrt{2}\; S_2(q) \\ m &= 0 & S_0(q) &+ \sqrt{2}\; S_2(q) \\ m &= -1 & S_0(q) &- 1/\sqrt{2}\; S_2(q) \end{aligned} \qquad (61)$$

So the single scattering term of the cross-sections, averaged over all m is:

$$|f_n(q)|^2 + |f_p(q)|^2 + 2\,\mathrm{Re}:\left\{f_n^*(q)\, f_p(q)\, S_0(q)\right\} \qquad (62)$$

The quadrupole form factor drops out in the averaging. Note, however, that $S_0(q)$ contains L=2 wave function information since

$$S_0(q) = \int (u^2 + v^2)\, j_0(qr)\, dr \qquad (63)$$

Similarly, the multiple scattering terms will have integrals like

$$\langle im|\, e^{i(\overrightarrow{\frac{q}{2}+q'})\cdot\vec{r}}\,|im\rangle \qquad (64)$$

By arguments similar to Fridman's [1974], these integrals can be evaluated. We expect that the quadrupole form factor will again disappear from the expressions leaving expressions exactly like those of the spinless theory, but with the spinless form factor replaced by the spherical form factor. The form factor in the multiple scattering terms appears only in the integrands and thus only its small q^2 behaviour is important. Since the quadrupole form factor is small at small q^2 (Franco 1969, Sidhu 1972), working through the details of the calculations was not warranted.

The important result is that the breakup-plus-elastic cross-section involves <u>only</u> the spherical form factor, even when the deuteron spin is taken into account.

4.5.2 The choice of form factor

In the analysis of the data for this thesis, the spherical (also called charge or monopole) form factor derived from the Reid softcore deuteron model was used. It has been tabulated by Greben [1970] along with other realistic models and the Hulthen model. All except the Hulthen model agree at the few percent level. The Hulthen model over-estimates the form factor considerably, and should not be used. See figure 20.

For the form factor appearing in integrands, a triple sum-of-exponentials fit to the Reid hard core spherical form factor was used. [See also Section 4.3.3] This fit was done at small q^2 by Franco [1975] who found the following parametrization which we have used:

$$S_0(q) = \Sigma_i W_i e^{-a_i q^2} \qquad \sum W_i = 1 \tag{65}$$

where $W = .34, .58, .08$

and $a = 141.5, 26.1, 15.5$

Chapter V

EXTRACTICN OF A NEUTRON CROSS-SECTION

5.1 PARAMETRIZATION OF THE CROSS-SECTIONS

If the recoil particle is not identified as a deuteron, the cross-section measurement will include elastic and breakup events. Equation 40 then describes the differential cross-sections that should be observed. For each set of data taken with a deuterium target, a corresponding hydrogen target set was taken without changing anything other than the target - both within a few hours atmost. This simultaneous determination of the cross-section on protons is essential to the extraction of the neutron cross-section. The two sets of data are simultaneously fit to their respective differential cross-sections. The neutron amplitude is determined only by the deuterium data, but the proton amplitude is determined by both hydrogen and deuterium data.

The elastic nucleon amplitudes were parametrized as the usual exponentials in q^2:

$$f_p(q) = A_p(i+\rho)\, e^{-b_n q^2}$$
$$f_n(q) = A_n(i+\rho)\, e^{-b_p q^2} \qquad (66)$$

It was assumed for ρ, the ratio of the real to imaginary part of the scattering amplitude, that $\rho_p(q) = \rho_n(q) = \rho_p(0) = \rho$. So the single scattering term, SS, is

$$SS = (1+\rho^2)\,[A_n^2 e^{-2b_n q^2} + A_p^2 e^{-2b_p q^2} + 2S(q)\, A_n A_p\, e^{-(b_n+b_p)q^2} \qquad (67)$$

The tabulated spherical Reid form factor was used for this term (see section 4.5.2).

In the two SD terms, a sum-of-exponentials form factor was used (see section 4.5.2).

$$S(q) = \sum_i W_i \, e^{-a_i q^2} \qquad \sum_i W_i = 1 \qquad (68)$$

This enabled the integral to be done exactly. The result is:

$$SD = -\frac{A_p A_n^2}{K} \, e^{-2bq^2} (1+\rho)^2 \sum_i \frac{W_i \, e^{\frac{+b_n q^2}{a_i+b_n+b_p}}}{a_i + b_n + b_p} \quad + \text{term}_{n \leftrightarrow p} \qquad (69)$$

For the double scattering term, DD, the integrals were done ignoring the neutron-proton slope difference and using instead the average slope. This is adequate since the DD term is small in our t range, and the difference in slope parameters is small. The result is

$$DD = \frac{A_n^2 A_p^2}{16K^2 b} (1+\rho)^2 \, e^{-bq^2} \sum_i \frac{W_i}{a_i + b} \qquad b = \frac{b_n + b_p}{2} \qquad (70)$$

In this parametrization of the nucleon amplitudes, the slope parameter is constant in t. If it was not, we would use the average slope at t/4 in calculating DD. [t/4 is the most probable value of the momentum transfer for each scatter when the apparent momentum transfer for the event is t.]

The deuteron cross-section is then parametrized with four parameters: A_p, b_p, A_n, b_n and the proton with two: A_p, b_p. The best values of these four parameters are then found by minimizing a χ^2

which is the sum of the χ^2 for both target's data, i.e.:

$$\begin{aligned} \chi^2 &= \chi^2_H + \chi^2_D \\ \chi^2_H &= \Sigma_i^{N_H} \left[\frac{d\sigma}{d\Omega}\Big|_H (q_i)^2 - Y_{Hi} \right]^2 / \delta Y_{Hi} \\ \chi^2_D &= \Sigma_i^{N_D} \left[\frac{d\sigma}{d\Omega}\Big|_D (q_i)^2 - Y_{Di} \right]^2 / \delta Y_{Di} \end{aligned} \qquad (71)$$

where

N_H, N_D are the number of data points for hydrogen and deuterium targets.

YH_i, YD_i, YH_i, YD_i are the measured cross-sections on hydrogen and deuterium at q^2_i, and their respective random error (absolute) estimates.

$$\frac{d\sigma}{d\Omega}\Big|_H (q_i^2) = \left| A_p (i+\rho)\, e^{-b_p q_i^2} \right|^2 = (1+\rho)^2 A_p^2\, e^{-2b_p q_i^2}$$

(note the factor of 2 in the exponent.)

$\frac{d\sigma}{d\Omega}\Big|_D (q_i^2)$ is given by the sum of equations 67, 69, and 70

We use $q^2 = |t|$.

Note that this method does not require that the t values at which there are hydrogen target measurements coincide with those for deuterium target measurements, or that $N_D = N_H$.

The YH_i, YD_i and t_i have been calculated from the event samples according to the methods and selections described in section 3.2. The errors δYH_i, δYD_i are calculated as described in Section 3.2. The selection of the ND and NH data points used in the fitting is described in the next section. All results will be shown as

$d\sigma/dt\,(|t|)$ rather than $d\sigma/d\Omega(q^2)$, using

$$\frac{d\sigma}{dt}(|t|) = \frac{\pi}{P_1 P_3}\frac{d\sigma}{d\Omega} \qquad (72)$$

where $P_3=P_1-|t|/(2m)$ and π/P_1P_3 is the Jacobian used when the scattering is from a proton at rest. Strictly speaking, it is incorrect for scattering from deuterium since $P_3 \neq P_1-|t|/(2m)$ on account of the Fermi momentum (see section 4.4). However, the expected value of P_3, $\langle P_3\rangle = P_1 - |t|/(2m)$ for single scatter breakup events which are the majority of events.

5.2 SELECTION AND COMBINATION OF POINTS FOR FITTING

Events were collected in 'runs' during which the settings of the experimental apparatus remained fixed. The vertical scattering angle was stepped 1.5 mr from run to run and since the spectrometer accepted a range of at least ±1.4 mr, there was considerable overlap in the t ranges of the runs. Even though two points from different runs might have t values very close together, they were <u>not</u> combined into one point. However, if two or more runs were taken at the same angle, they were combined according to the following rule since they constituted several measurements of the same quantity:

$$\begin{aligned} Y &= \left\{\textstyle\sum_i Y_i/\delta Y_i^2\right\}/W \\ t &= \left\{\textstyle\sum t_i/\delta Y_i^2\right\}/W \qquad (73)\\ \delta Y &= 1/W \end{aligned}$$

where $W = \sum_i \frac{1}{\delta Y_i^2}$

where Y are the measured cross-sections at t. If after this combination, $\delta Y/Y > 20\%$, the point was rejected from fitting. This eliminated points with fewer than about 25 events contributing to the cross-section.

As shown in section 3.6, the vertical angle offset error is cancelled to first order by averaging runs with positive and negative offset. The rule for combining these runs is:

$$\begin{aligned} Y &= (Y^+ + Y^-)/2 \\ t &= (t^+ + t^-)/2 \\ \delta Y &= \sqrt{\delta Y^{+2} + \delta Y^{-2}}\,/2 \end{aligned} \qquad (74)$$

5.3 CALCULATION OF A NEUTRON POINT-TO-POINT CROSS-SECTION

In order to present a tabulation and a graph of the neutron cross-sections, we need to extract the neutron cross-section on a point-to-point basis. If we look at the SD and DD terms as corrections to the data calculable from the fitted parameters, we can subtract them from the measured deuterium cross-section to get the SS term at each t value. Now, from equation 67

$$SS = \sigma_p + \sigma_n + 2S(q)\sqrt{\sigma_n \sigma_p} \qquad (75)$$

So

$$\sqrt{\sigma_n} = -S(q)\sqrt{\sigma_p} + \sqrt{(S^2(q)-1)\,\sigma_p + \sigma_D - SD - DD} \qquad (76)$$

is the 'extracted cross-section'. A slight complication is that the t values at which σ_d is measured are not quite the same as the t values for σ_p. If Y(t) is used for the measured point-to-point cross-section at t, and $\sigma'(t)$ for the fitted value, we can use

$$\sqrt{Y_n(t_D)} = -S(t_0)\sqrt{Y_H(t_H)} + \sqrt{(S^2(t_0)-1)\cdot Y_H(t_H)\cdot R} + Y_D - SD - DD \quad (77)$$

$$R = \sigma_p(t_0) / \sigma_p(t_H) \approx 1$$

to get the neutron cross-sections. Ignoring the errors in the fitted quantities, SD and DD, the error-squared is:

$$\delta Y_n^2(t_0) = \left(\frac{1}{1+S}\right)^2 \delta Y_0^2(t_D) + R^2 \, \delta Y_H^2(t_H) \quad (78)$$

Chapter VI

RESULTS

6.1 THE PION AND PROTON CROSS-SECTIONS

The results of the simultaneous fits to the hydrogen and deuterium target data are shown in table 9. Shown are p, π^+ and two fits to π^-, one for a t range limited to that of the π^+ data $(.06<|t|<.32)$, and a second using the full range of the available π^- data $(.04<|t|2.5)$. The reason for a separate fit to the truncated range is given below. The tabulated values of the cross-sections are in Appendix C. In order to reduce the correlations of the errors of the parameters, the amplitude at $t=.25$, $f(.25)$, rather than at $t=0$, $f(0)=A$, was a used as fitting parameter. The data must be extrapolated to $t=0$ to determine $f(0)$, and so $f(0)$ is highly correlated to the slope.

We first note that the proton slopes agree excellently with those published previously [SAS 1977] by our collaboration using only, and a much larger sample of hydrogen target events. [Recall that these slopes are from the simultaneous fit. Hydrogen only data fits are discussed below.] The hadron-proton magnitudes do not agree with those previously published, but differ by 15%. This is partly due to the fact that the spectrometer cuts were opened beyond the uniform acceptance region (to $\phi=\pm1.6$ mr, $\theta=\pm.8$ mr) in an effort to increase the number of events. A comparison between

Table 9.

Results of the Fits to the Cross-sections

	Sec below*		Value	Error	Correlation Coefficients		
π+	AP		1.724 (1.83)	0.1091E-01 (.012)			
	AN		1.550	0.2052E-01	+.416		
	BP		3.969 (4.005)	0.5392E-01 (.03)	-.654	-.656	
	BN		4.470	0.1116	-.586	-.663	-.504
	A_p		21.62				
	A_n		22.44				
	χ^2		65.86/53 = 1.243				
π⁻	AP		1.753 1.86	0.1455E-01 .012			
	AN		1.620	0.2684E-01	-.636		
	BP		4.199 (4.2)	0.7220E-01 (.03)	-.872	+.567	
	BN		4.125	0.1497	+.559	-.840	-.640
	A_p		25.08				
	A_n		20.63				
	χ^2		40.95 /60 = .686				
π⁻	AP	full range	1.698	0.9193E-02			
	AN		1.731	0.1555E-01	-617		
	BP		4.416	0.4100E-01	-.708	+.425	
	BN		3.590	0.7004E-01	+.402	-.596	-.610
	A_p		26.23				
	A_n		18.04				
	χ^2		155.8/89 = 1.75				
p	AP		2.431	0.3702E-01			
	AN		2.189	0.6474E-01	-.619		
	BP		4.827 (4.83)	0.1206 (.03)	-.924	+.566	
	BN		5.022	0.2405	+.555	-.908	-.593
	A_p		66.04				
	A_n		59.00				
	χ^2		73.31/50 = 1.466				

---

1. Numbers in parenthesis are from SAS [1975].
2. AP, AN are $f_p(t=.25), f_n(t=.25)$
3. A_p, A_n are f^*f at $t=0$

hydrogen target data with these and tighter cuts ($\phi=\pm1.4$ mr, $\theta=\pm.75$ mr) shows that about 4% of the difference can be accounted for. The remainder is undetermined. A comparison of π^+d and π^-d determines the relative normalisation of π^+ and π^- (see below) so the use of the pions to check the Glauber theory is not sensitive to the absolute normalisation.

Figures 23 to 26 show the Glauber Theory fits to the hadron-deuteron data. Both the fit and the data have been divided by the sum of the fitted nucleon cross-sections and plotted on a linear scale in order to display the fit most sensitively. [Note that hydrogen target data (not shown) has been simultaneously fit.] The fits agree excellently with the data. This is the usual area and order of success of the Glauber Theory. The comparison of the extracted pion-neutron cross-sections in the light of I-spin invariance is a much more stringent test, however.

Figures 27 to 34 show the hadron-proton and the extracted hadron-neutron cross-sections determined from the hydrogen-deuterium simultaneous fits. For π^+ and π^- the figures show the data for a reaction, its fitted curve, and the fitted curve for the reaction to which it must be equal by I-spin invariance. Note that the xp data is hydrogen target data but the fitted curves are from the simultaneous fit. The xn 'data' is the point-to-point data extracted by the procedure described in the previous section.

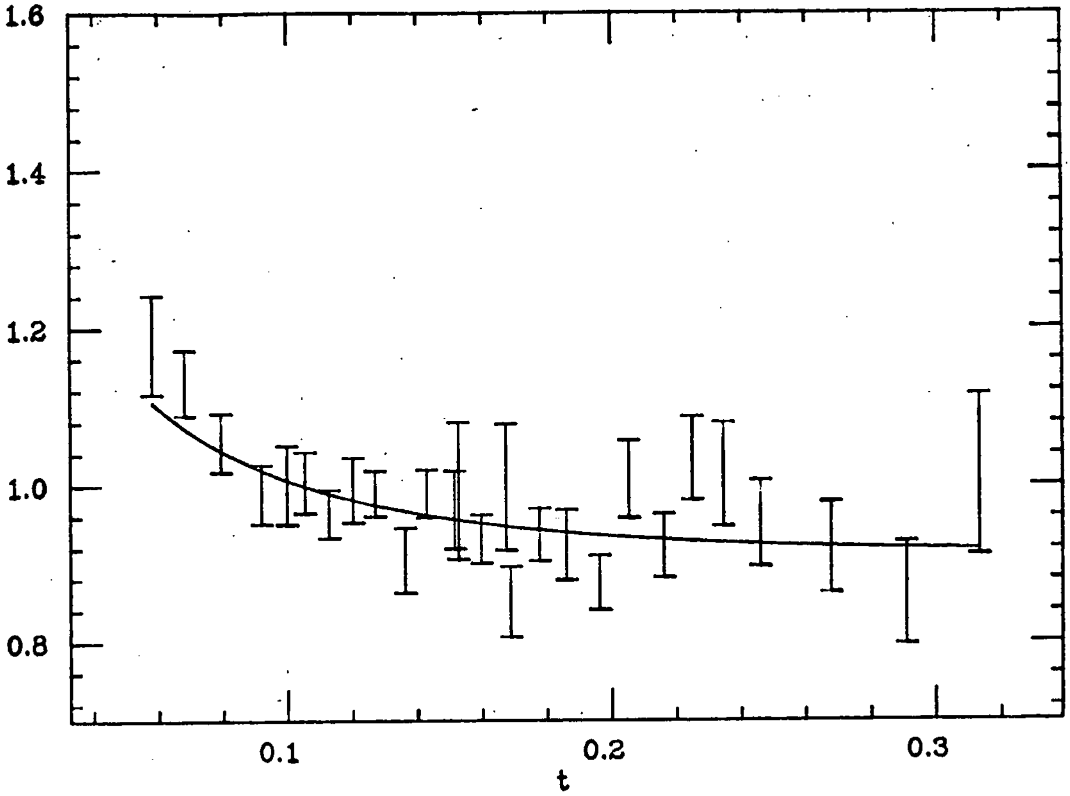

Figure 23: π+d Cross-section

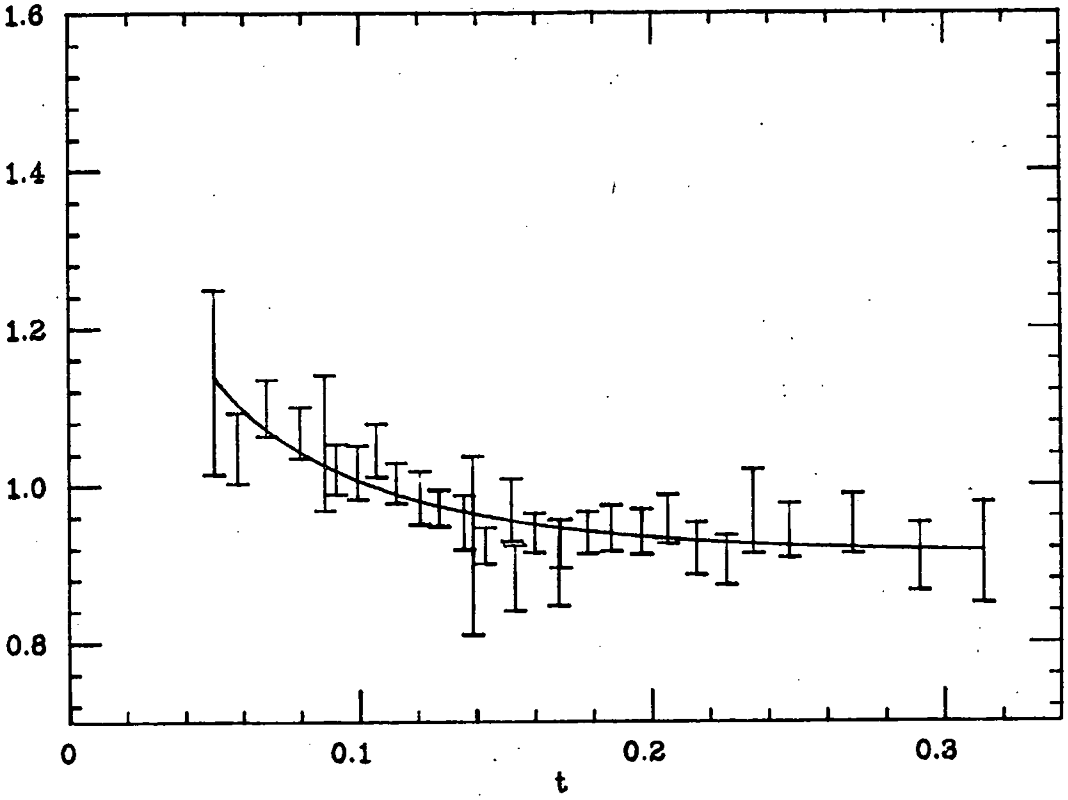

Figure 24: π-d Cross-section

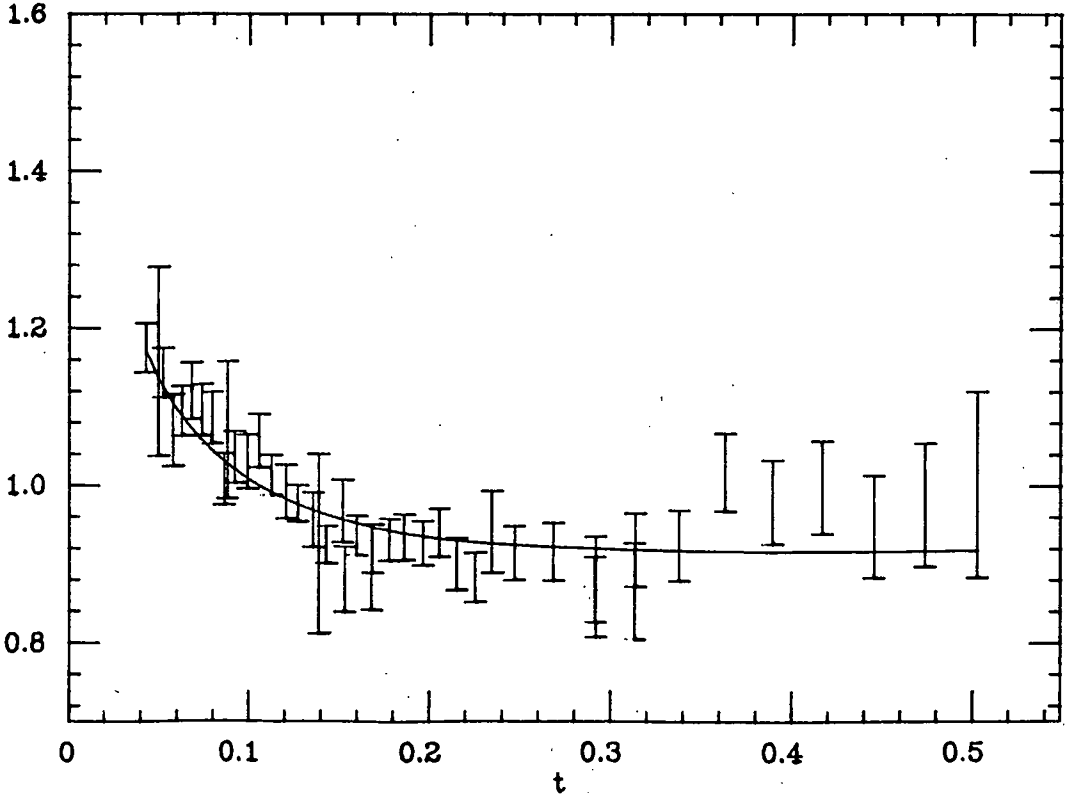

Figure 25: π-d Cross-section, Full Range

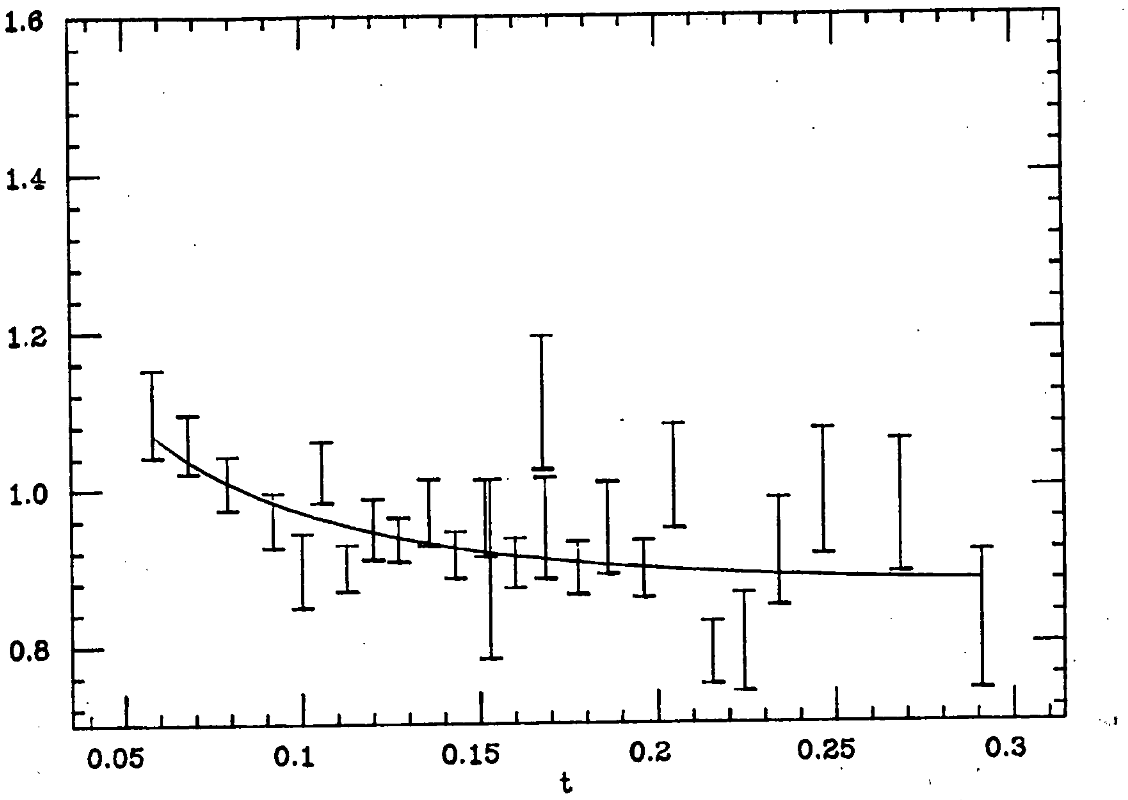

Figure 26: pd Cross-section

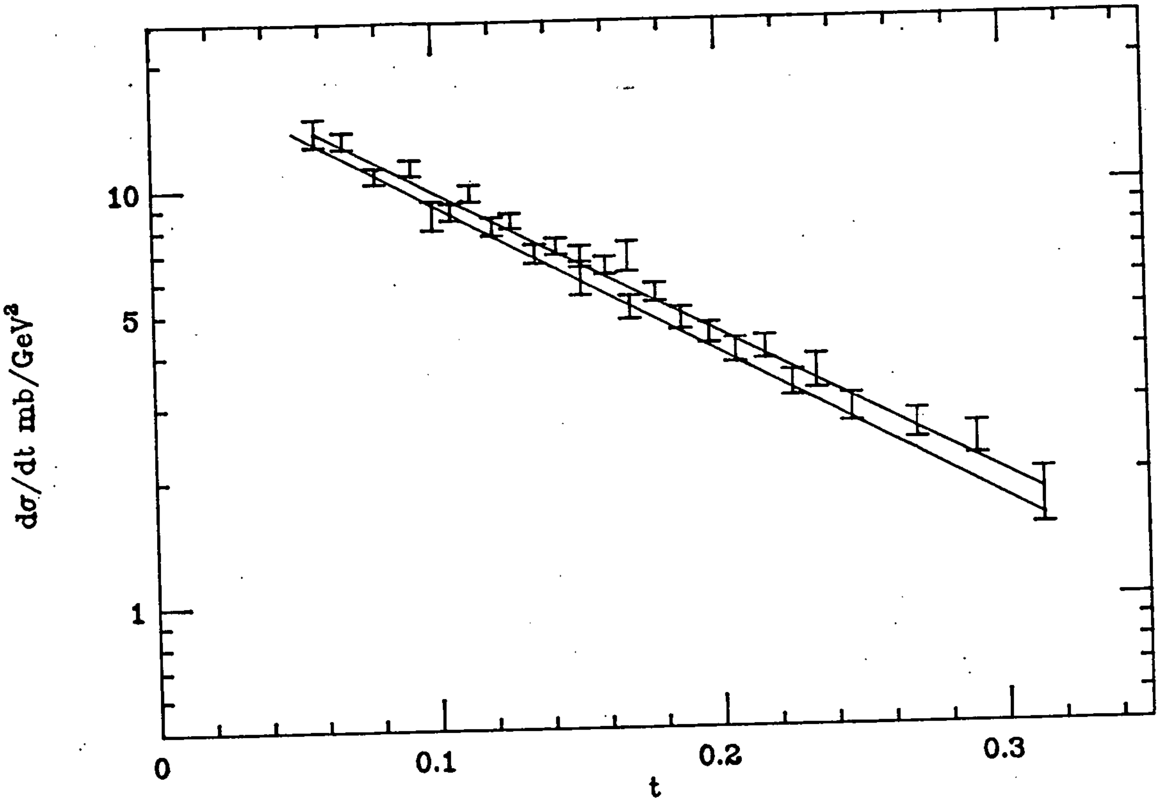

Figure 27: π⁺p Data and Fit with π⁻n Fit

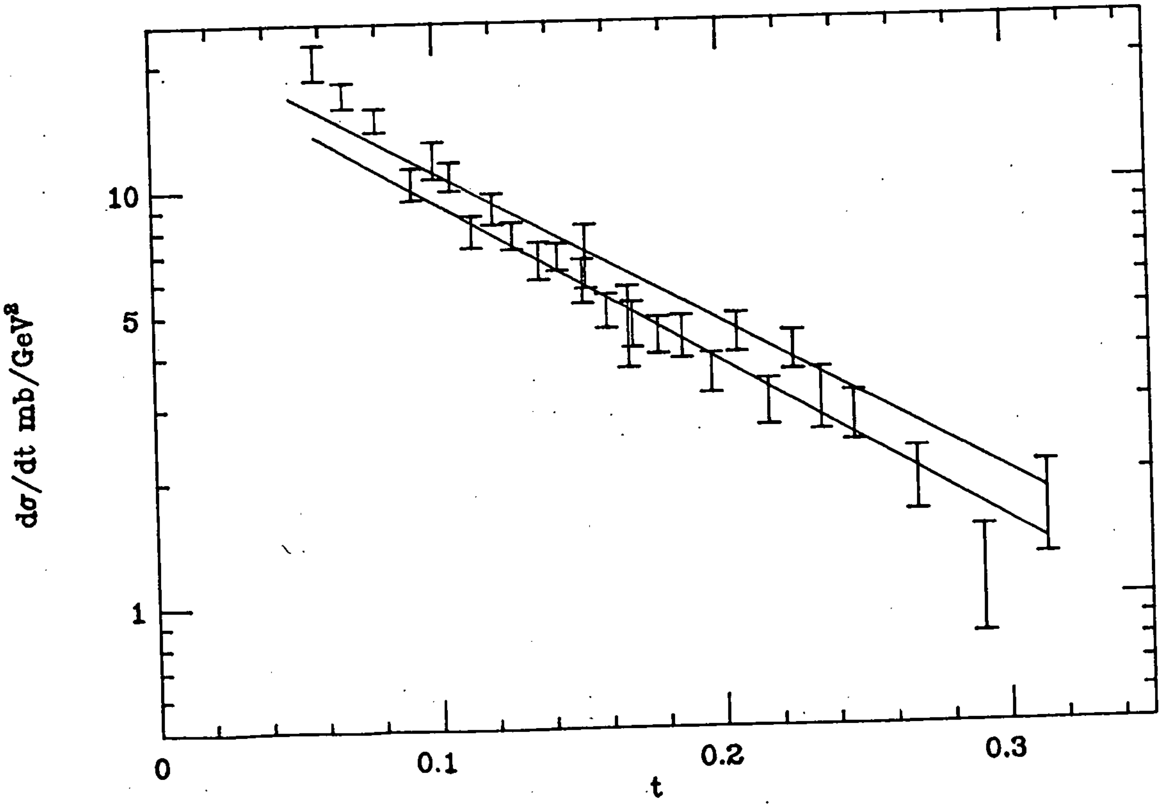

Figure 28: π⁺n Data and Fit with π⁻p Fit

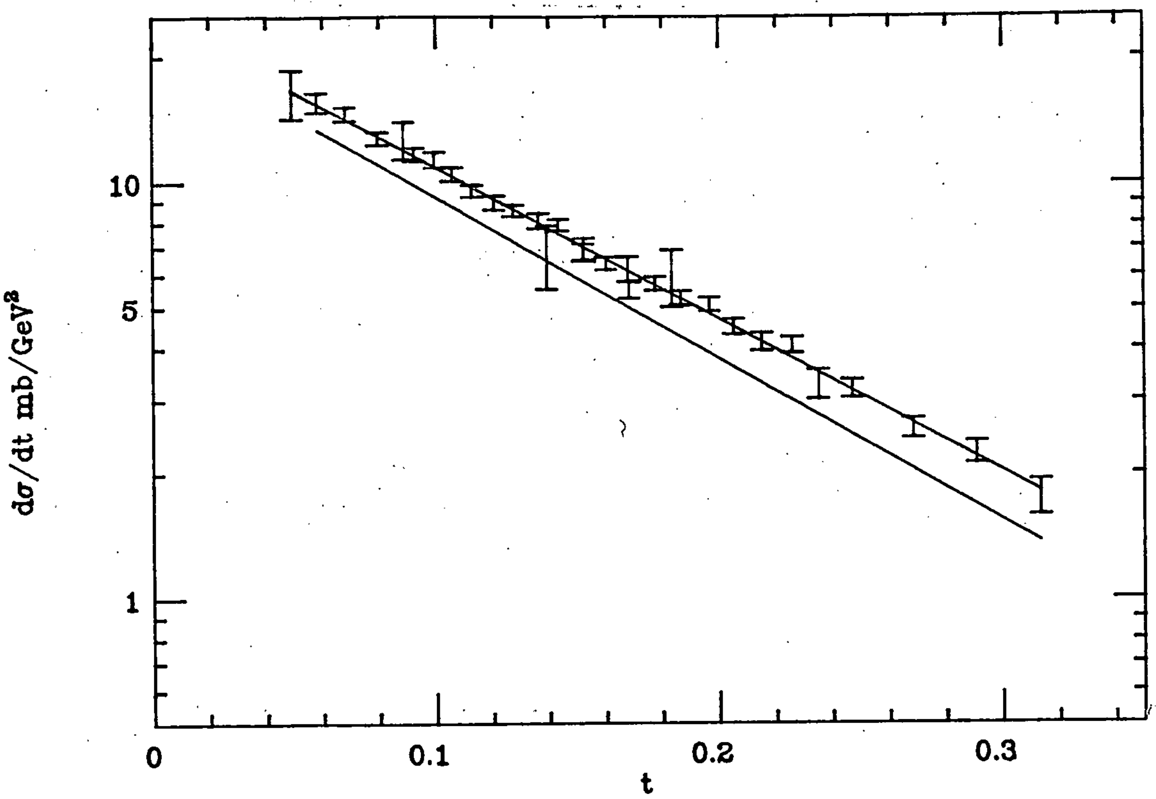

Figure 29: π⁻p Data and Fit with π⁺n Fit

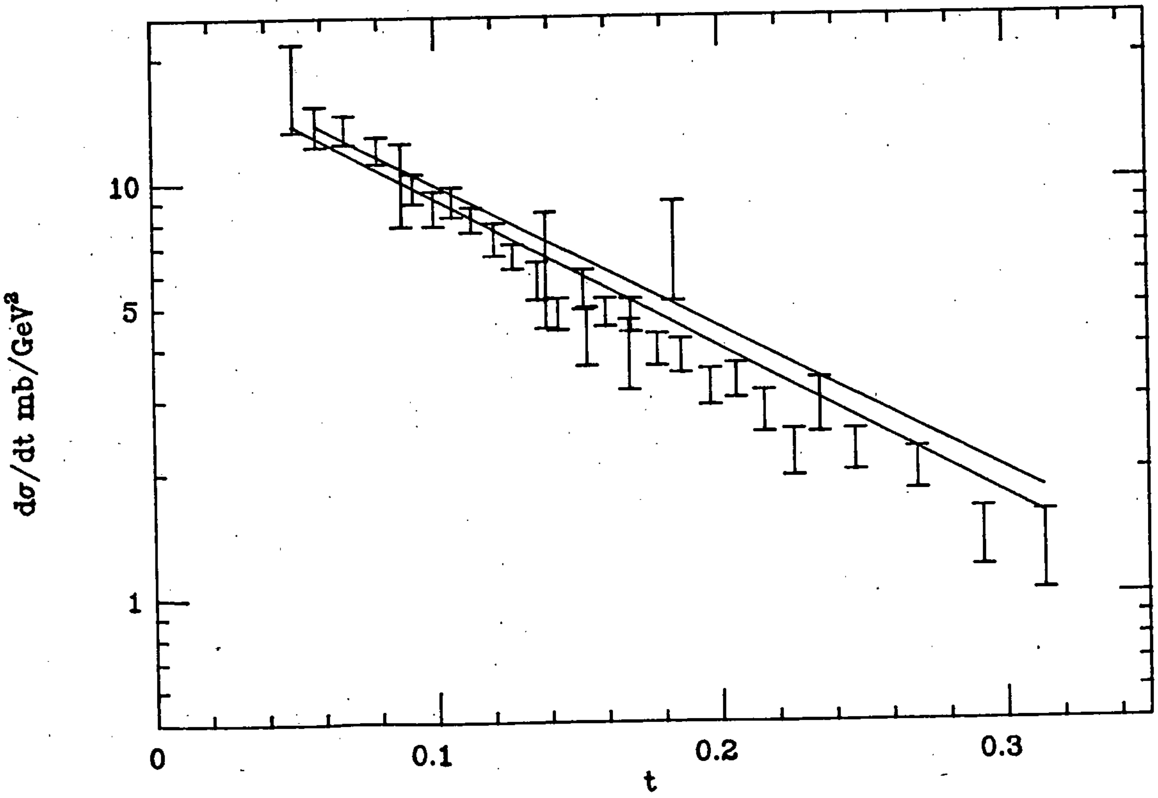

Figure 30: π⁻n Data and Fit with π⁺p Fit

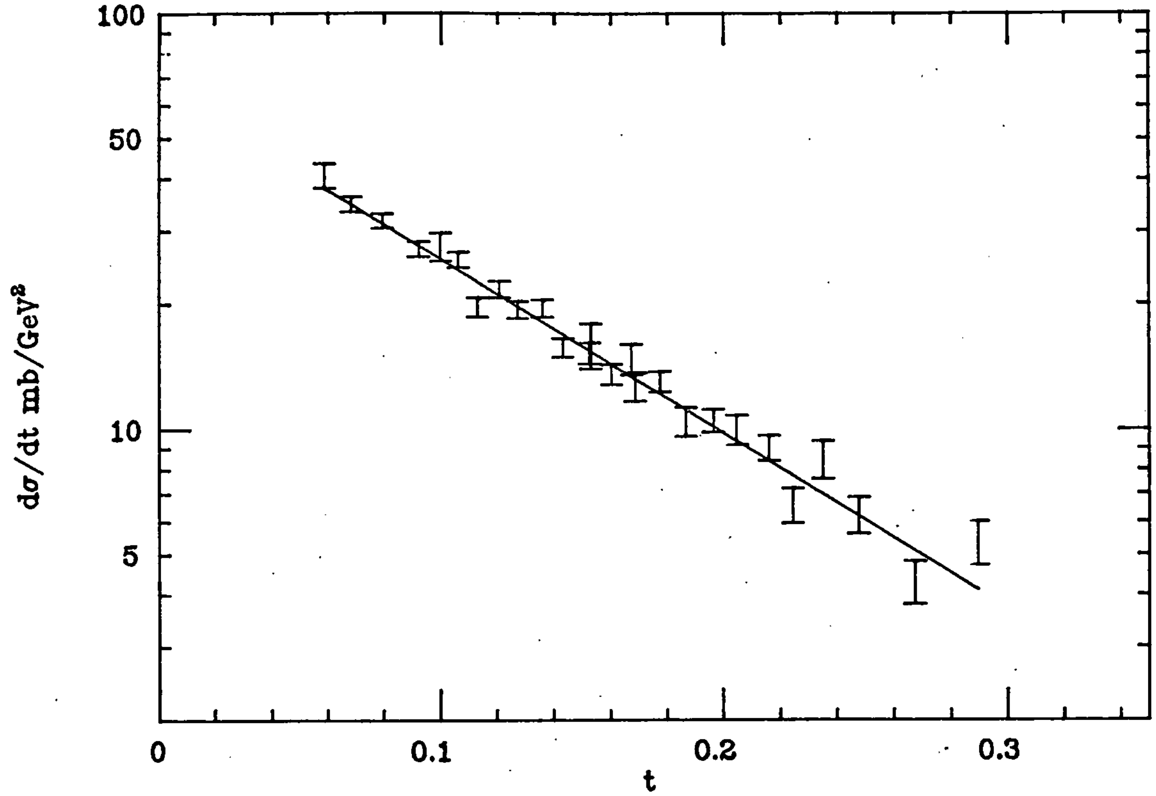

Figure 31: pp Data and fit

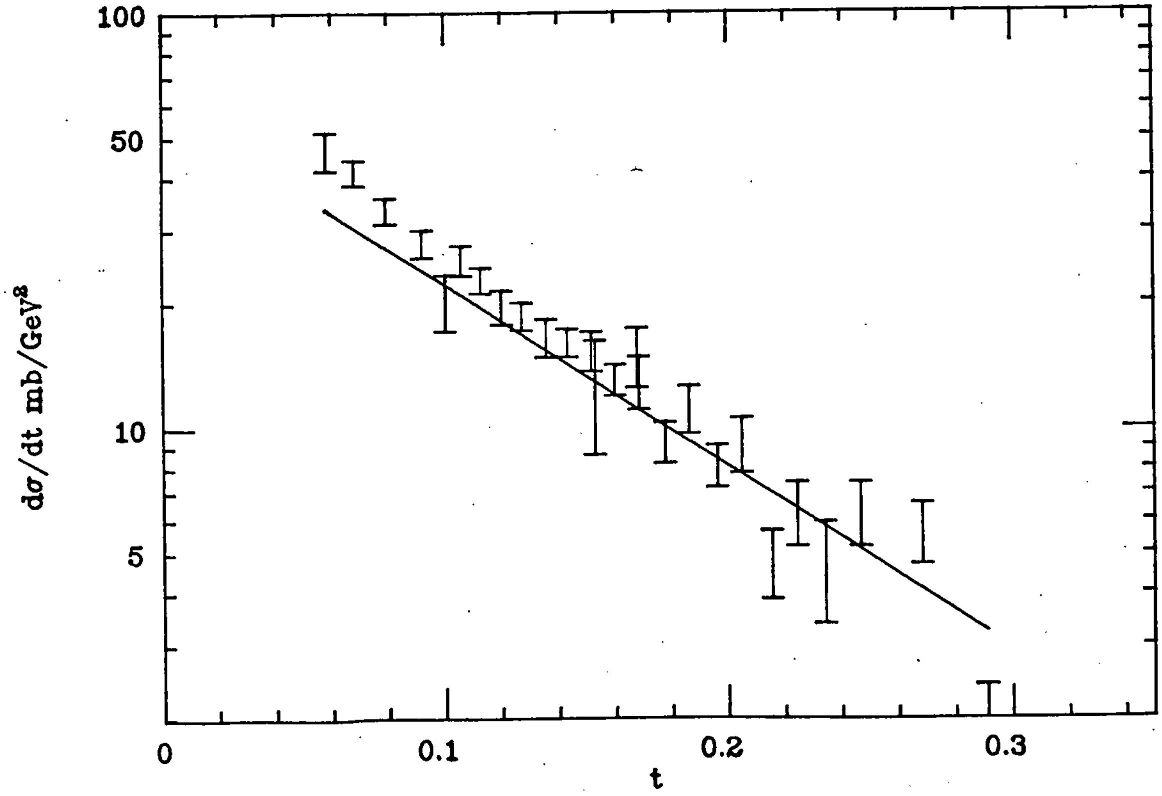

Figure 32: pn Data and fit

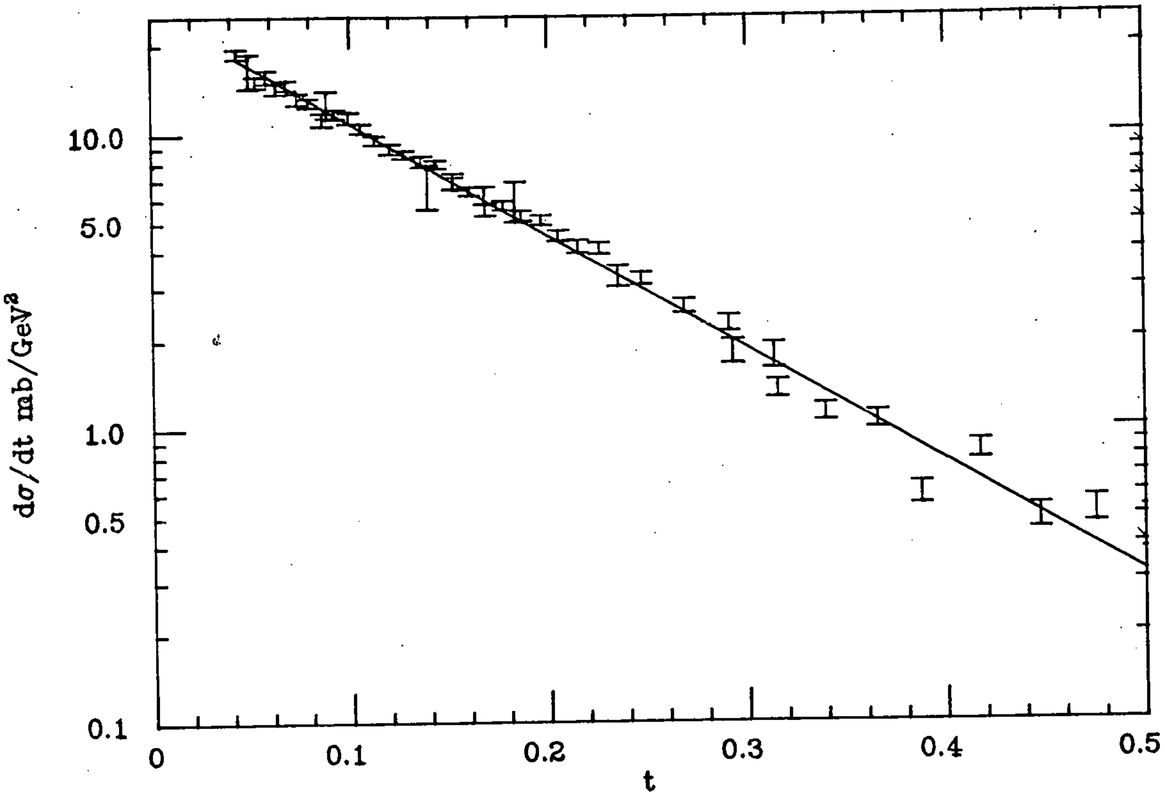

Figure 33: π⁻p Data and fit, full range

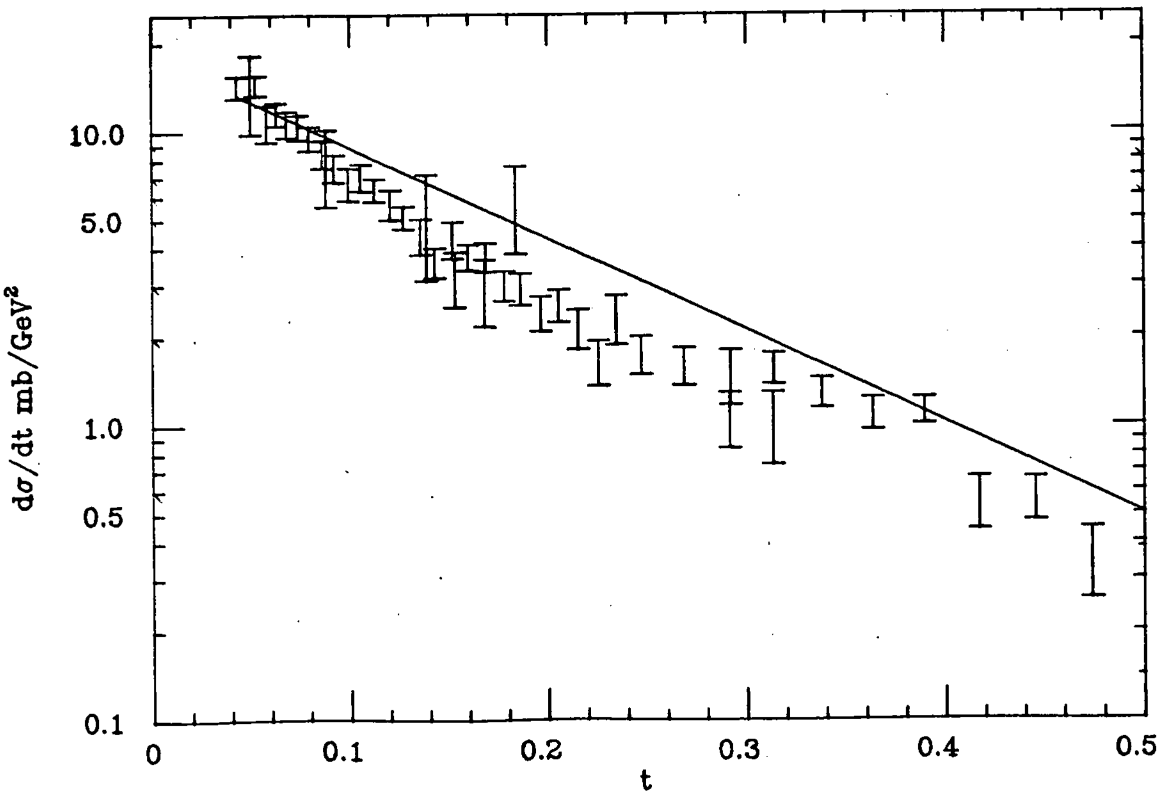

Figure 34: π⁻n Data and fit, Full Range

6.2 CONSISTENCY CHECKS

It is evident from the figures and the values of the parameters that the π^+ and π^- cross-sections we have determined are not consistent with I-spin invariance. The requirement that each parameter equal, within error, its I-spin complement, e.g. $b_{\pi^+p} = b_{\pi^-n}$, is too strong a requirement because the errors are correlated: A difference in slope can be compensated by a difference in magnitudes. Contour plots of χ^2 at the minima showed that A_n and b_n could be adjusted in concert by several times their errors, and still be within the 63% confidence level region of the minima. Indeed the off-diagonal elements of the covariance matrices are appreciable, compared to the diagonal. The proper way to test the consistency of the parameters with I-spin invariance is to use the covariance matrices and compare all parameters at once using the compatability check described in Eadie [1971:p.176]. This test measures the nearness in parameter space of the two sets of parameters to their weighted (by the full covariance matrix) average. The nearness, Q^2, is distributed like a χ^2 for, in this case, 4 degrees of freedom. This test was applied and Q^2 was found to be 418 for 4 degrees of freedom: the two sets of parameters are most probably not compatible. Examination of the χ^2 contours near the minima confirmed this. Unless the random errors are much larger than those estimated by the fitting program[1], the inconsistency of the parameters could be due to run-to-run systematic errors-to which the analysis is very sensi-

---

[1] the CERN program, MINUIT.

tive: The neutron cross-section is primarily a difference between two independent measurements and the I-spin comparison involves 4 independent measurements.

The study of the systematic errors was made difficult by the absence of almost all redundancy in the data runs. None-the-less, several checks were made and are described in the next sections along with other checks on the multiple scattering model.

Effect of the t Range on the Fit Results. The uncertainty in a slope determined from a set of data points and their errors, depends on the t range of the data as well as the errors on the individual points. If that range is small on a scale set by the errors of the points, the uncertainty in the slope will be large. We expect, therefore, that the fit results will depend somewhat on the t range. To avoid this, comparisions of π^+ and π^- were always done with equal t ranges, even though the π^- data was available for both higher and lower t. In fact we used only runs corresponding in spectrometer central angle in the various comparison tests below. Table 9 shows the π^- fits for both the short and complete t ranges.

6.2.1 Checks on consistency of the data

1) Systematic differences between particle sign. The π^+d cross-section must equal the π^-d since the deuteron has I-spin=0. By plotting the π^+d and π^-d cross-sections on the same plot, we can test for the presence of any scale or other systematic differences between the positively and negatively charged beam runs.

These runs were taken several days apart. Figure 35 is such a plot but with the data divided by $50e^{-8t}$ so that the plot will show any slight scale difference. In fact, there is about a 4% difference.

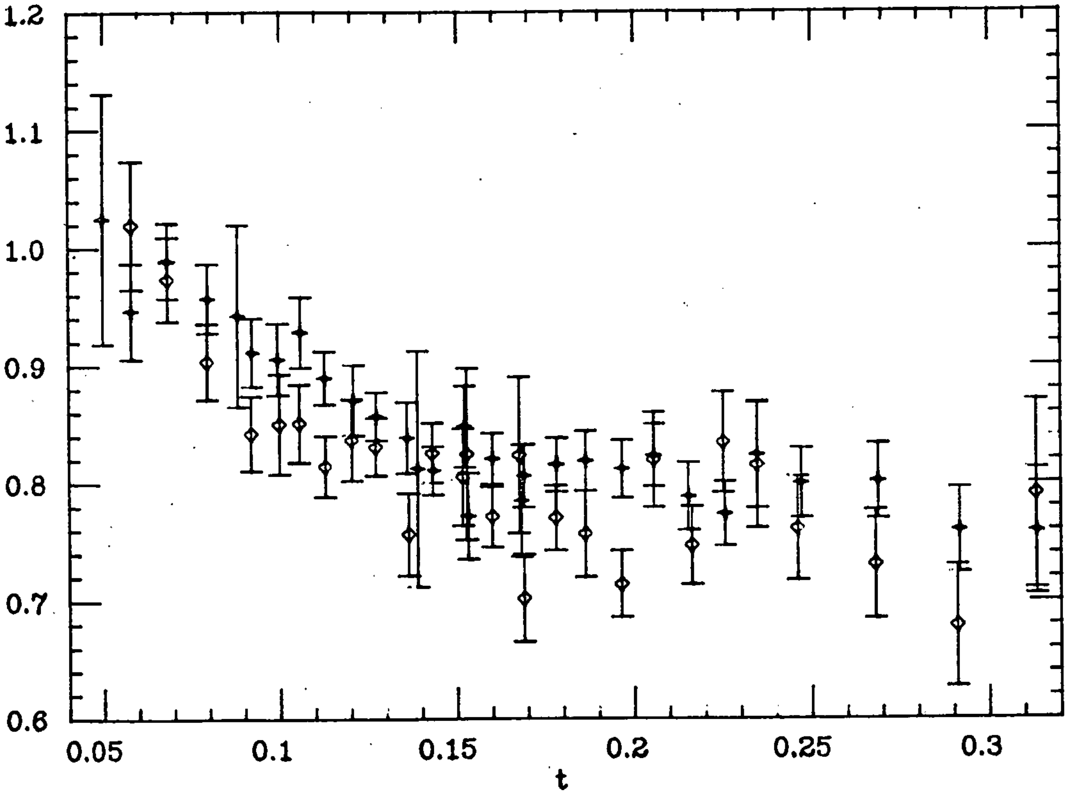

Figure 35: π^+d and π^-d Cross-sections / $(50e^{-8t})$

2) <u>The presence of systematic differences between the hydrogen and deuterium target runs</u> can be discovered to some extent by comparing a) a proton target cross-section fit using the hydrogen target data alone, b) a fit using both target data, and c) a fit using $\chi^2_D+\chi^2_H/10$. This comparison shows to what extent the hydrogen target data is determining the fit against the 'will' of the deuterium target data. We expect very small systematic dif-

ferences because the data for the two targets were collected within hours of each other. Table 10 shows that this is indeed the case.

Table 10.

Fit Results for different target weighting

		$\frac{\chi^2_H}{100}+\chi^2_D$	$\frac{\chi^2_H}{10}+\chi^2_D$	$\chi^2_H+\chi^2_D$
π^+	f_p (.25)	4.60	4.63	4.64±.029
	f_n (.25)	4.77	4.76	4.75±.14
	b_p	3.93	3.93	3.96±.042
	b_n	4.49	4.52	4.49±.20
π^-	f_p (.25)		5.05	5.02±.014
	f_n (.25)		4.47	4.50±.031
	b_p		4.30	4.27±.022
	b_n		3.97	4.01±.047

3) <u>The presence of an anomalous run</u> might be detected by comparing the fits using positive vertical angle offset data with those using negative offset (Section 3.6 describes the two offset configurations of the apparatus and their necessity). Due to the offset error $\delta\phi$, the two sets of data will be shifted with respect to each other, in t by $2\delta t = 4t\delta\phi/\phi$. Since δt is small, usually less than .005, and since the log-slope parameter, b, of the cross-section is certainly constant over a t interval of this size, we expect the two fit's results for b to agree. Table 11 shows the results of this test. The differences in slopes are within the random errors.

Table 11.

Comparison of AVB± Fits

	amplitude at t=.25			slopes		
	AVB+	AVB-	average	AVB+	AVB-	average
π^+p	1.69	1.73	1.72 ±.0077	4.10	3.96	3.97 ±.03
π^+n	1.51	1.59	1.55 ±.013	4.49	4.50	4.47 ±.07
χ^2	1.215/50	1.178/49		1.24/53		
π^-p	1.73	1.76	1.75 ±.0056	4.27	4.20	4.20 ±.03
π^-n	1.60	1.64	1.62 ±.012	4.09	4.13	4.13 ±. 5
χ^2	.684/55	.873/56		.683/60		

6.2.2 Checks on consistency of the model

1) Deuteron Form Factors. If equation 40 is evaluated with both nucleon amplitudes specified as Ae^{-bq^2} but with the form factor not yet specified, the angular integrations can be carried out. The interference term, can then be written, apart from a constant factor, as [Franco 1966]:

$$e^{-2bq^2}\int_0^\infty S(q')\, e^{-2bq'^2}\, I_0(2bqq')\, q'\,dq' \qquad (79)$$

where I_0 is the Bessel function with purely imaginary argument. The above integral was then evaluated a) numerically for the Hulthen form factor, b) the tabulated Reid formfactor, and analytically for c) the sum-of-exponentials fit to the Reid form factor described in section 4.5.2, as well as d) a sum-of-exponentials fit to the Hulthen form factor - not at small t but for .1 < |t| < .4. Figure 36 shows this integral as a function of t. For this figure, the nucleon amplitude slope parameter, b, was fixed at 4; in fact, the integral is quite insensitive to b. The three curves agree only at the 20% level. The fit to the Reid softcore charge form factor is to be preferred, for reasons explained in Section 4.5.2. However, this difference only contributes an uncertainty of about 2% to the deuterium cross-section. We note here that a computation using the analytic solution agreed exactly with the numerical solution for the sum-of-exponentials form factor, so the integrals were solved correctly.

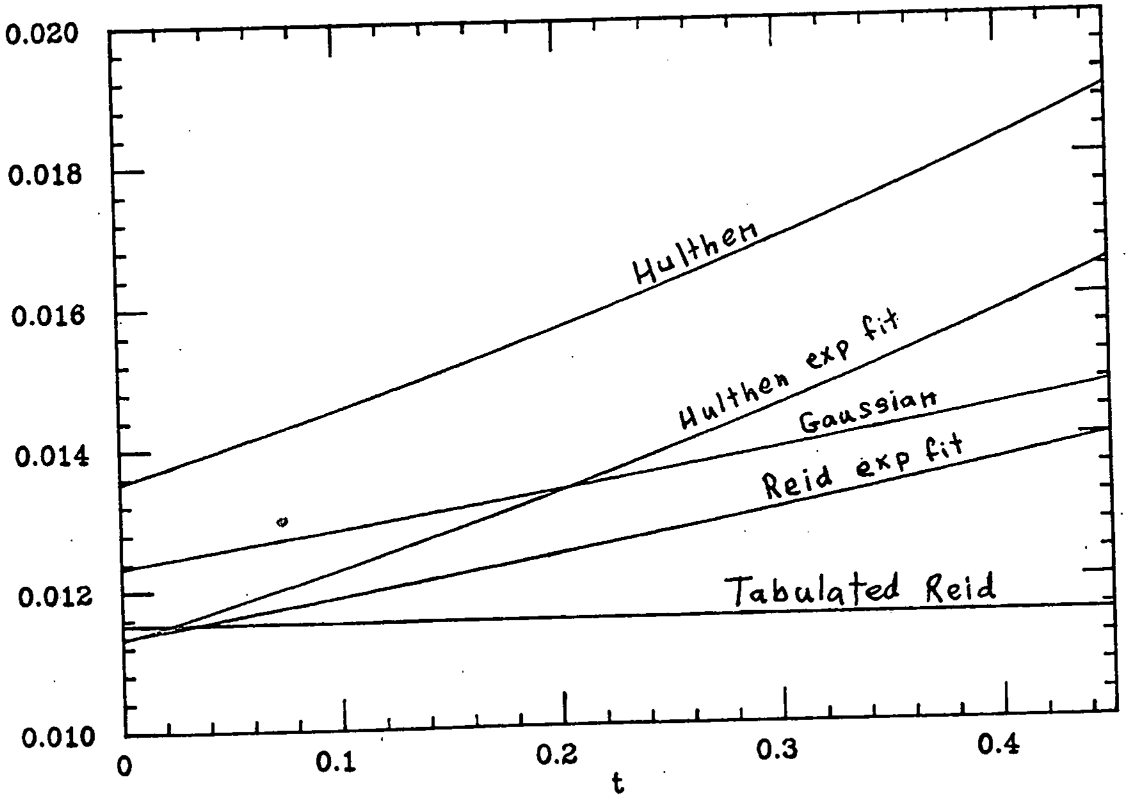

Figure 36: Plots of the Integral in Equation 79

2) <u>Exponential Parametrization of the Nucleon Amplitudes</u> The logarithmic slope parameter of the nucleon cross-section, b, is known to be t dependent at this energy. The usual parametrization of the amplitudes is $Ae^{\frac{(-bt+ct^2)}{2}}$ [SAS 1977]. This form diverges exponentially at large t and so integrals cannot be done

analytically with it. An alternate parametrization is $Ae^{-bt} + Ce^{-dt}$, which has the advantage that integrals can often be done analytically. Fits were done with this parametrization. The χ^2 for these fits were not significantly better when the additional degrees of freedom are considered - i.e. by the F-test. The data is not significantly accurate to discern curvature over the limited t range here. All results quoted in this thesis are therefore with the nucleon amplitude parametrization of Ae^{-bt}.

3) <u>Contribution of the Multiple Scattering Terms</u>. One problem with the statistical significance of the multiple scattering terms is that they depend appreciably on the nucleon cross-sections at t/4. At the low end of the t range of the data, these cross-sections are determined by extrapolation. Statistical uncertainties in the slope parameter, which is primarily determined by the single scattering terms, are magnified by the lever arm of the extrapolation. This is probably more important than the steepening of the slope towards t=0.

Fits were done without the single-double interference and double scattering terms, and also with their magnitude arbitrarily doubled. The results for π^+ are shown in table 12. This gives an indication of the extent to which the neutron cross-section is affected by the fit attempting to compensate for any defficiencies of the multiple scattering terms, or the absence from the model of other important terms. The fitted neutron cross-sections are too low. However, even doubling the interference term, which is negative, does not increase the neutron cross-section enough.

Table 12.

Fit Results with Enhanced and No Multiple Scattering Terms

	SS only	SS+SD+DD	SS+2(SD+DD)
f_{π^+p} (.25)	1.725±.007	1.724±.007	1.724±.021
f_{π^-n} (.25)	1.429±.009	1.550±.013	1.682±.035
b_{π^+p}	3.96±.026	3.97±.033	3.97±.10
b_{π^-n}	4.60±.076	4.47±.070	4.36±.18
χ^2	66.1927/53	65.8645/53	65.486/53

6.3 CONCLUDING REMARKS

In summary we were not able to find systematic errors sufficiently large to cause the incompatibility between the π^+ and π^- fits of the pion-nucleon amplitudes. The relative normalization of π^+ to π^- and of hydrogen to deuterium runs seems not to be the cause. For both π^+ and π^- the neutron cross-sections are steeper and lower than expected from the corresponding proton cross-sections. This could be due to the form factor being larger than it should be, or the interference term smaller than it should be. However, the form factor is already < .05 over much of the t range and, as shown above, an arbitrary doubling of the multiple scattering terms is not sufficient to restore compatibility. An anomalous run or runs seems a most likely possibility, since the AVB± test is not sensitive to normalization shifts. It is conceivable that such a shift could be large enough to cause the observed incompatibility. There remains the possibilities of an undetermined systematic error, an error in the analysis programs, or finally a defficiency in the Multiple Scattering Theory. The lack of redundancy in the data, the appreciable random errors, and the rather limited range in t over which data was taken make the latter difficult to support.

Appendix A

Pion-Nucleon Cross-section Relations from I-spin

The four pion-nucleon I-spin states are:

$$|\pi^+\rangle\ |p\rangle = |+1\rangle\ |+1/2\rangle = |3/2\ +3/2\rangle$$

$$|\pi^-\rangle\ |p\rangle = |-1\rangle\ |+1/2\rangle = 1/3\ |3/2\ -1/2\rangle - 2/3\ |1/2\ -1/2\rangle$$

$$|\pi^+\rangle\ |n\rangle = |+1\rangle\ |-1/2\rangle = 1/3\ |3/2\ +1/2\rangle + 2/3\ |1/2\ +1/2\rangle$$

$$|\pi^-\rangle\ |n\rangle = |-1\rangle\ |-1/2\rangle = |3/2\ -3/2\rangle$$

So if T is the scattering operator for the pion-nucleon system, the scattering amplitudes for the various reactions are:

$$T(\pi^- p) = \langle\pi^- p|T|\pi^- p\rangle = 1/3\ T(I=3/2) + 2/3\ T(I=1/2)$$

$$T(\pi^+ p) = \langle\pi^+ p|T|\pi^+ p\rangle = T(I=3/2)$$

$$T(\pi^- n) = \langle\pi^- n|T|\pi^- n\rangle = T(I=3/2)$$

$$T(\pi^+ n) = \langle\pi^+ n|T|\pi^+ n\rangle = 1/3\ T(I=3/2) + 2/3\ T(I=1/2)$$

Then $d\sigma/dt = |\langle|T|\rangle|^2$ is given by:

$$\frac{d\sigma}{dt}(\pi^- p \rightarrow \pi^- p) = 1/9\ |T_3 + 2T_1|^2 = \frac{d\sigma}{dt}(\pi^+ n \rightarrow \pi^+ n)$$

$$\frac{d\sigma}{dt}(\pi^- n \rightarrow \pi^- n) = |T_3|^2 = \frac{d\sigma}{dt}(\pi^+ p \rightarrow \pi^+ p)$$

Appendix B

Analysis with the Recoil Particle

B.1 INTRODUCTION

The apparatus for this experiment included hodoscopes placed below the target in the path of the recoiling particles. The original purpose of the detectors was to determine if the recoil particle was in the plane defined by the incident and scattered particles. This would be true only for elastic scattering and so inelastic contamination of the hydrogen target elastic data at large |t| could be reduced by a coplanarity cut. The detectors evolved into two crossed hodoscopes with time-of-flight and dE/dx information when deuterium target running was included in the plans for the experiment.

In the analysis of the data for this theses, an attempt was made to identify the recoiling particles as a proton, deuteron, or neutron by using the dE/dx information. [For reasons discussed below, the other information available was not used.] This separation of events would allow measurement of the elastic deuteron cross-section and the elastic neutron cross-section, the latter via xd->xn(p), p being a proton spectator. The elastic proton cross-section determined from xd->xp(n) could be compared to xp-->xp as a check. This chapter discusses the analysis technique of the recoil separation and why extraction of the neutron and deuteron cross-sections met with only limited success.

B.2 RECOIL DETECTOR DESCRIPTION

An extensive description of the recoil detector arm of the spectrometer is given in Gottschalk 1974. We give here only a brief description and mention of why only the dE/dx detectors were used in this analysis.

The recoil detector consisted of a) the Z or dE/dx detector, a 16 element hodoscope with bins across the beam direction and b) the Rϕ detector, a 32 element hodoscope with bins parallel to the beam direction. They were made from NE110 plastic scintillator whose chemical composition, relevant to loss of energy by ionizing particles, is CH. Figures 37 and 38 show the detector sizes and placement.

The Z-detector scintillators were 1/8 inch thick by 6 inches by 2 1/4 inches; the Rϕ-detector, 3/8 inch thick by 46 inches by 1 inch. Both were overlapped by thirds. The 16 Z-detector signals were linearly OR'ed into an analog-to-digital convertor (ADC) and read into the computer as event data to give the dE/dx information. Because the pulse heights were kept small in order to be linear, they were amplified before each was fed to a disciminator driving a latch. The Rϕ detector was also latched and both were read into the computer. The logical OR of all Z signals, the OR of the odd (upper layer) Rϕ signals, and the OR of the even (lower layer) Rϕ signals were used to stop three time-to-digital converters (TDC'S). The three TDC's were started by a common start signal from a detector in the beam.

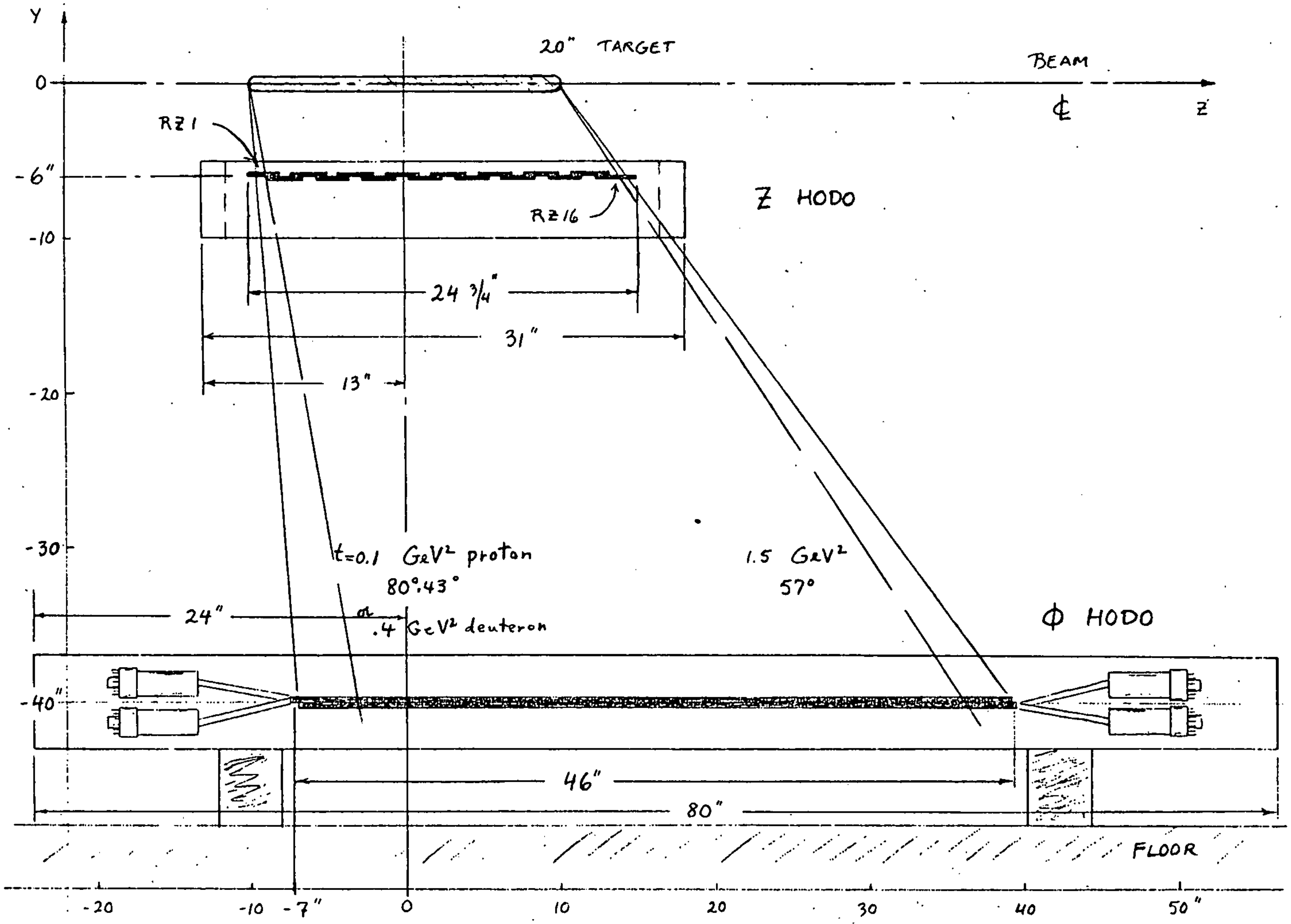

Figure 37: Recoil Hodoscope Side View

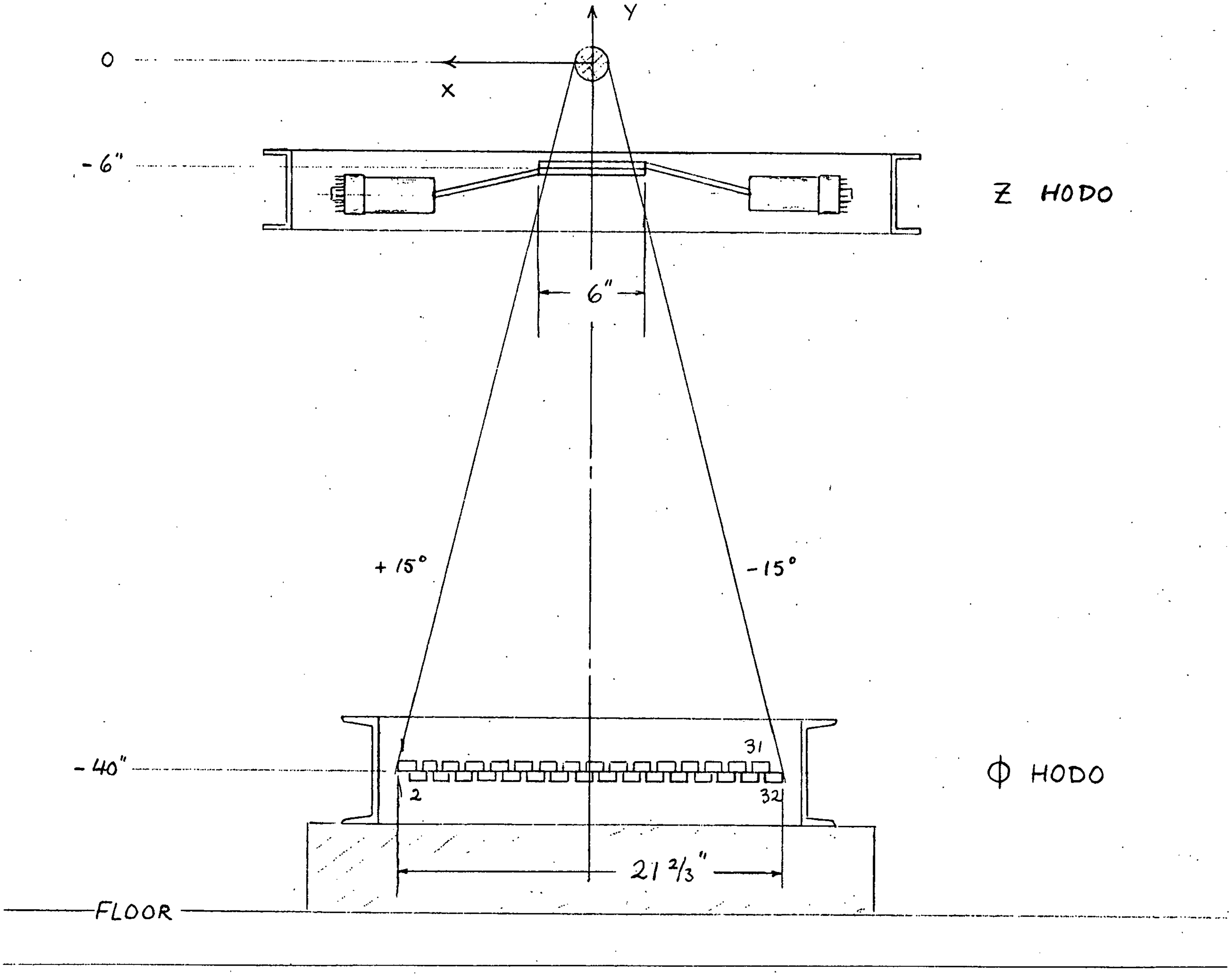

Figure 38: Recoil Hodoscope End View Looking Downstream

The Z or dE/dx detector had 100% acceptance in recoil polar angle for the t range of this thesis. Its azimuthal acceptance was ±15°. For proton targets at 50GeV and a spectrometer horizontal acceptance of ±.75 mr, recoils from events with spectrometer vertical scattering angle greater than 3.5mr are accepted. This includes all data in the thesis. For deuteron targets, however, the Fermi momentum allows the recoil to be out of the scattering plane and the ϕ acceptance is no longer 100%.

The proton-deuteron separation was to be enhanced by the independent time-of-flight measurement. We set up a TOF reconstruction essentially that of Gottschalk 1974, but were unable to use it in the analysis. For reasons not understood, the TDC was stopped early (about 5ns) for 25% of the events. That this was happening, was clearly determined by a special study using recoil protons from elastic hydrogen target events which hit bins made from the overlap of two Rϕ-detectors. For these events, there was enough information (along with the z coordinate from the Z hodoscope and the scattered particle trajectory) to check the consistency of the two TDC readings.

B.3 IDENTIFYING PARTICLES BY THEIR ENERGY LOSS

The energy loss, dE/dx, of a high energy particle in a medium due to ionization has been well studied and depends on the velocity, charge, and mass of the particle. If we know the velocity - or kinetic energy - we can then distinguish between a proton and deuteron recoiling on the basis of the energy it deposits in traversing a thickness of scintillator. The pulse height from the scintillation counter varies linearly with the energy deposited. The kinetic energy of the recoil particle is calculated from the 4-momentum transfer determined by the scattered particles as follows:

$$t = (P_1 - P_3)^2 = (P_4 - P_2)^2 \qquad \text{-4 vectors}$$

$$t = m_2{}^2 + m_4{}^2 - 2E_2 E_4 + 2\vec{P}_2 \bullet \vec{P}_4$$

for $m_2 = m_4$ and a target at rest and $E = T + m$

$$t = 2m_2{}^2 - 2m_2(T + m_2)$$

$$\text{or } T = |t|/2m_2$$

So for M = deuteron mass and m = proton mass, we have for:

1) Elastic deuteron scattering: $T = |t|/2M = |t|/4m$
2) breakup single scattering: $T = |t|/2m$
3) breakup double scattering: two scatterings at $\theta/2$ each $T = \frac{|t|/4}{2m} = \frac{|t|}{8m}$

Figure 39 shows dE/dx for a deuteron and a proton in scintillator, both recoiling in a reaction with 4-momentum transfer t. For the breakup cases these results ignore the Fermi momentum of the deuteron, since $\vec{P}_2$ was taken zero. Also, the proton in a double scattering event can be scattered with any scattering angle, provided the neutron scattering angle compensates. The value given is only for the most probable double scattering event. [See section 4.4]

If we take $\vec{P}_2 \neq 0$, we can calculate an expected kinetic energy <T> for single scattering:

$$|t| = 2m^2 - 2E_2 E_4 + 2\vec{p}_2 \cdot \vec{p}_4 \qquad (80)$$

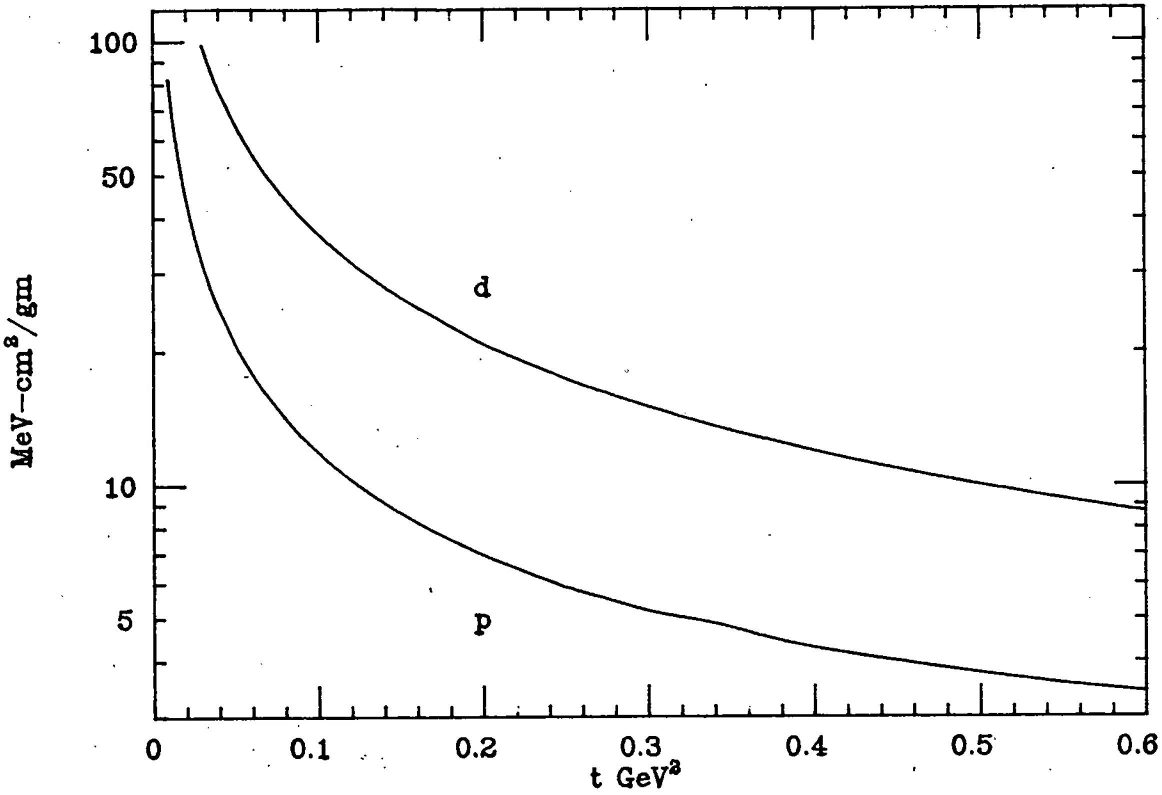

Figure 39: dE/dx vs. t for Scintillator, CH

$\vec{P}_2$ is isotropic in the lab and so $\vec{P}_2 \bullet \vec{P}_4$ will average to zero. Then

$$-t = 2Tm_2 + 2m_2 - 2m_2 + 2T_2(T+m_2)$$

$$\frac{|t|}{2m} = T + \frac{T_2 T}{m} + T_2$$

$$\langle T \rangle = \frac{\frac{|t|}{2m} - \langle T_2 \rangle}{1 + \langle T_2 \rangle / m} \qquad (81)$$

where $\langle T_2 \rangle$ is the expected Fermi kinetic energy << m since

$$p^2 = E^2 - m^2 = (E+m)(E-m) = (T+2m)T = 2mT \qquad (82)$$

for a nucleon in the deuteron:

$$\langle p_2^2 \rangle = 2m \langle T_2 \rangle \qquad (83)$$

so

$$\langle T \rangle = \frac{\frac{|t|}{2m} - \langle p_2^2 \rangle / 2m}{1 + \langle p_2^2 \rangle / 2m^2}$$

(84)

Now $\langle P_z{}^2\rangle$ for the deuteron is .012 GeV^2,② so $\langle T\rangle = (|t|-.012)/2m$, ignoring the denominator. This shift of 6 MeV was ignored in the analysis since the energy deposited by the proton is not a strong function of t for t>.08. See figure 40.

The energy loss per unit length of scintillator is, in general, given by a complicated expression. [See Rich 1954.] Also, one prefers to use the range R,

$$R(T) = \int_T^0 \frac{dE}{dE/dx} \qquad (85)$$

the distance taken to loose all the energy because:
Let T_i be the initial and T_f the final kinetic energy, i.e. $\Delta E = T_f - T_i$. Then the range with the initial kinetic energy is $R(T\ )$ and the range left on exit is $R(T_f)$. Therefore, the distance travelled was $\Delta x = R(T_i) - R(T_f)$. Since we know $T_i = |t|/2m$ and Δx, and want T_f

$$\begin{aligned} R(T_f) &= R(T_i) - \Delta x \\ T_f &= R^{-1}(R(T_i) - \Delta x) \\ \Delta E &= -(T_i - T_f) \end{aligned} \qquad (86)$$

This is the method of 'Residual Ranges'. R(T) has been tabulated for various materials and particles [Rich 1954]. We have fit their tabled data over the range of interest to the form AT^b which well describes the data and is easily inverted. The values of A and b, for T in MeV and R in gm/cm^2, used were:

---

[2] This was calculated by numerically integrating $\int \phi^*(\vec{p})\, p^2\, \phi(\vec{p})\, d\vec{p}$ for the Hulthen wave function, ϕ.

for scintillator .00182, 1.814

for hydrogen .00935, 1.840

for deuterium .01073, 1.840

tables for mylar were not available so A for scintillator was used, multiplied by the ratio of their dE/dx for a mimimum ionizing particle, 1.91/1.97.

One can also use the scaling rule

$$R_d(T_d) = \frac{M_d}{m_p} R_p\left(\frac{m_p}{M_d} T_d\right) \tag{87}$$

to get the deuteron range from the proton range table. One must be careful to calculate the energy lost in all material along the path of the recoil particle before the scintillator. For this experiment, this includes about .5 inch of liquid deuterium target and 22.5 mils mylar in the super insulation, target tube, target box window and hodoscope cover. Since the hodoscope bins are made by 1/3 overlap of adjacent counters, some particles can see twice the thickness of scintillator. The record of which hodoscope elements were hit, allows us to take this into account. The expected energy deposited in .125 inches of scintillator is shown in figure 40.

Note that this figure is quite different from the dE/dx vs. t curves [figure 39]. For very low t, the recoil particle does not escape the target and surrounding material. In the next t range, the particle deposits all its energy in the scintillator (i.e., is stopped). Finally, beyond the peak, the particle escapes the scintillator, but since the velocity in the scintillator increases as t increases, the ionization loss decreases. Be-

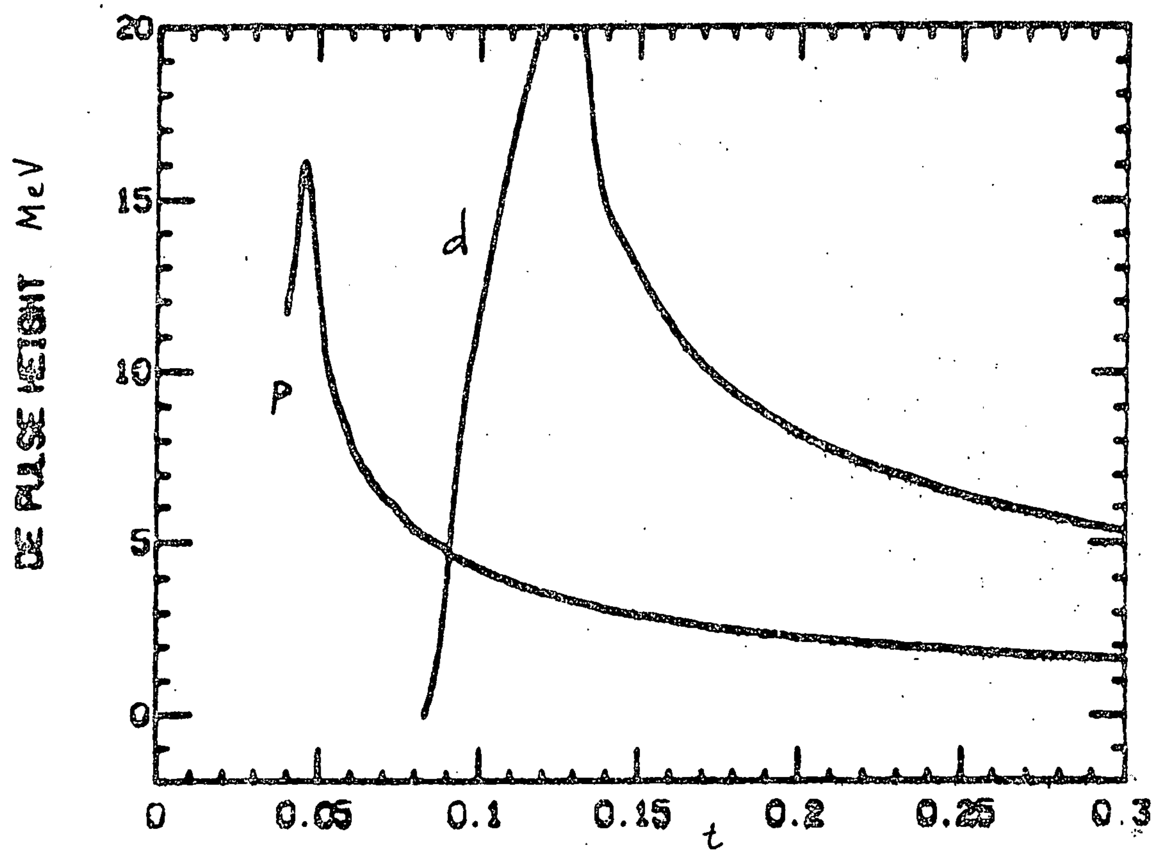

Figure 40: Expected Energy Deposited in the Scintillator

low t=.09, deuteron events will be confused with neutron events; from .09 to .12, with protons.

B.4 CALIBRATION

Protons recoiling from elastic scatters in the hydrogen target were used to calibrate the dE/dx system. A missing mass cut selected only elastic events whose recoil kinetic energy was then given by $T=|t|/2m$, t being determined by the scattering angle of the scattered particle. One calibrates the whole system (from scintillators through photo-tubes to the analog-to-digital converter) by comparing the pulse height measured as ADC counts with the expected energy deposited in MeV based on a) $T=|t|/2m$, b) the energy lost in escaping the target and surrounding material, and

c) the length of scintillator traversed. For each of the 16 hodoscope elements, about 100-200 events were used to fit for a gain and pedestal for that element:

$$\Delta E = g(PH - b) \tag{88}$$

The length of scintillator traversed included a correction accounting for the azimuthal and polar angles of the recoil particle as determined from the measured angles of the scattered particle. The failure to account for the energy loss in the target materials explains the t dependence of the gains noted by Gottschalk 1974. Since the phototube gains were not monitored during the data taking, the calibration procedure had to be done on a run-by-run basis.

The only offsets in the system were the ADC pedestal and an uncertainty in the thickness of materials surrounding the target, both common to all 16 detectors. The 16 intercepts b, were therefore averaged together to get a single intercept, B. The gains were then separately refit with the constraint b=B, i.e.

$$\Delta E = g(PH - B) \tag{89}$$

Each deuterium target run was analysed using the 16 gains and single pedestal determined by the corresponding hydrogen target run.

The resolution of the dE/dx system was about 20%. A plot of energy loss vs. t for a calibration run is shown in figure 41.

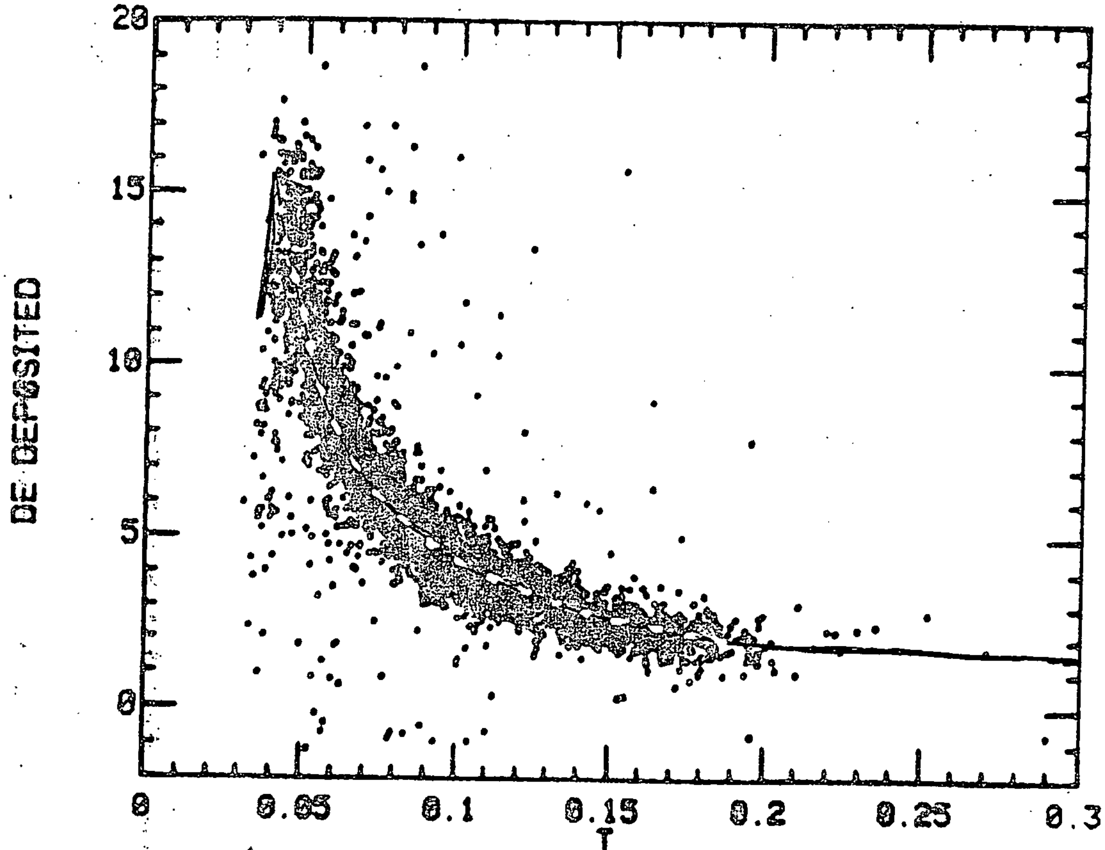

Figure 41: Energy Loss vs. t for a calibration Run

The small range of energy loss (2-5 MeV) for protons in our t range compared with the resolution, resulted in poor fits for the gains and pedestal. It was for this reason as well that the constraint of one pedestal for all 16 detectors was introduced. The consequence is that when extrapolating the fits to the pulse heights expected for deuterons (0-25 MeV), the energy loss calculated is wrong, and varies from its correct value differently for each of the 16 detectors. Deuterons with large expected energy losses indeed show considerable scatter from their predicted energy loss. Figure 42 shows a typical scatter plot of events from a single run with figure 40 superimposed. [Note: the location of the deuteron peak relative to its expected position is very sensitive to the amount of target material. The observed shift corresponds to 2 mm. of liquid hydrogen.]

B.5 THE DEUTERON SEPARATION

Figure 42 shows the energy loss vs. t for one run. Deuterons are unambiguously determined only between t=.12 and t=.17. There are several reasons for this state of affairs besides the energy resolution of the dE/dx system.

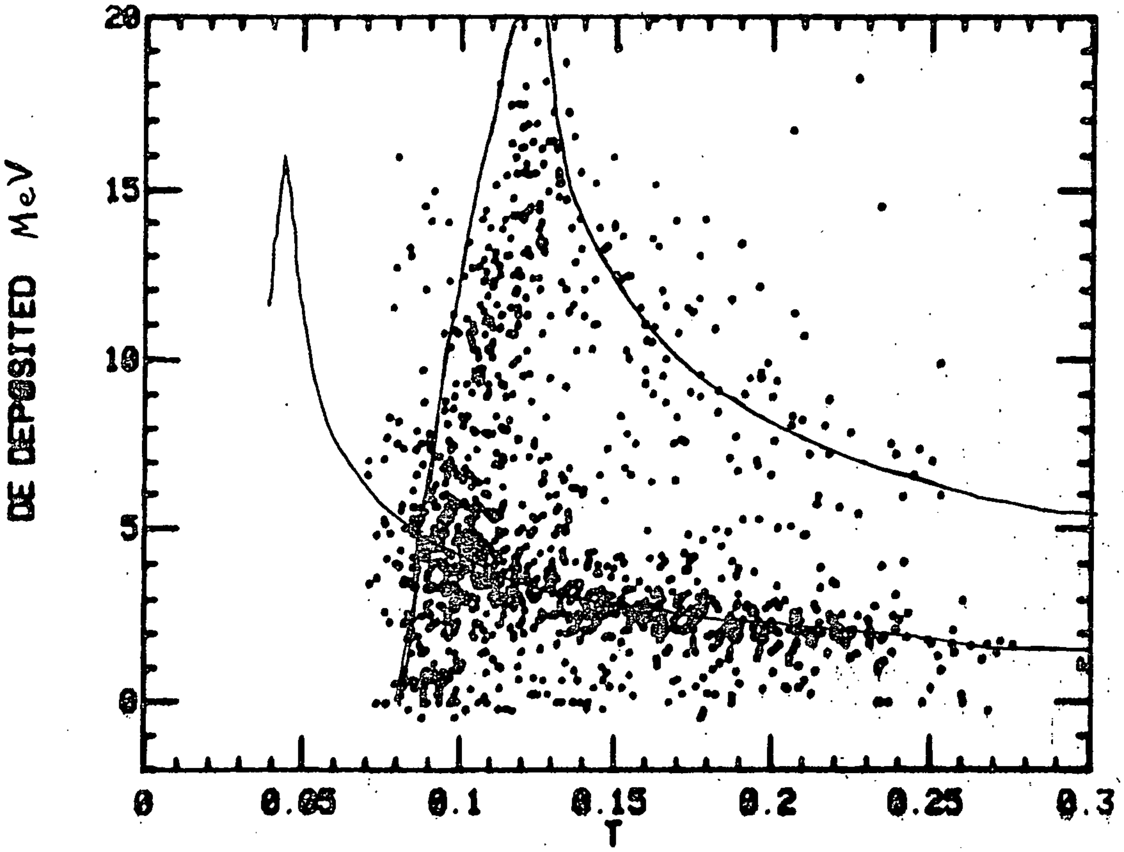

Figure 42: Energy Loss vs. t for a Deuterium Run

a) First there is the Fermi broadening of the proton kinetic energy. Figure 43 shows the result of Monte Carlo simulation using a Hulthen potential momentum distribution for the proton in the deuteron. The events are randomly distributed in t according to a cross-section, $Ae^{-8.8t}$, so this figure can be compared to the real data in figure 42. It does <u>not</u> include the experimental resolution. It does include the effect of the recoil particle's angle, which is not coplanar with the scattering on account of the Fermi momentum, and the recoil detector angular acceptance.

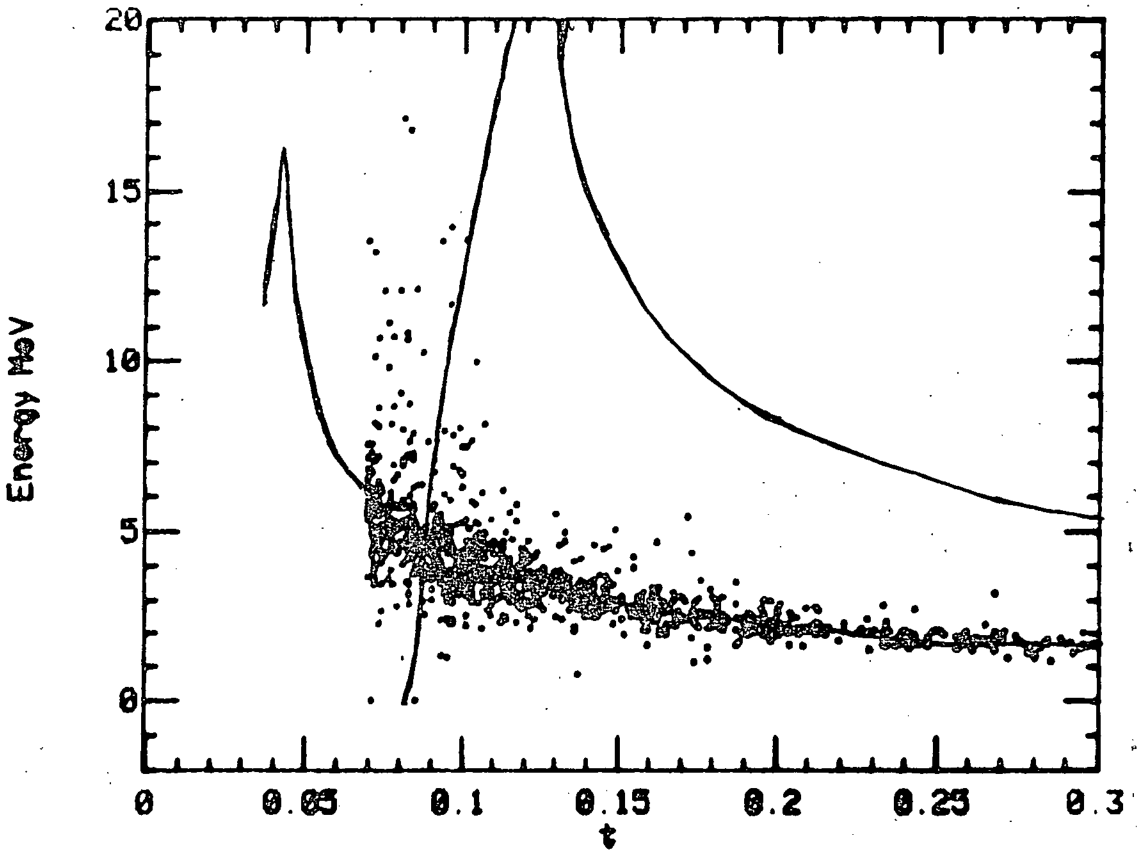

Figure 43: Fermi Broadening of Energy Loss, by Montecarlo

b) Almost half the breakup scatterings from a deuterium target are from a constituent neutron. The spectator proton is none-the-less moving due to the Fermi momentum and may find its way into the recoil detectors with a wide possibliity for its kinetic energy. This effect was not calculated since these protons should be fairly isotropic and therefore most would miss the detectors.

c) As shown in a previous chapter (The Multiple Scattering Theory), about 15% of breakup events are double scatters or single-double interference. The proton and neutron can share the recoil kinetic energy arbitrarily. The most probable event shares it equally. The expected energy loss for such protons is shown in figure 44.

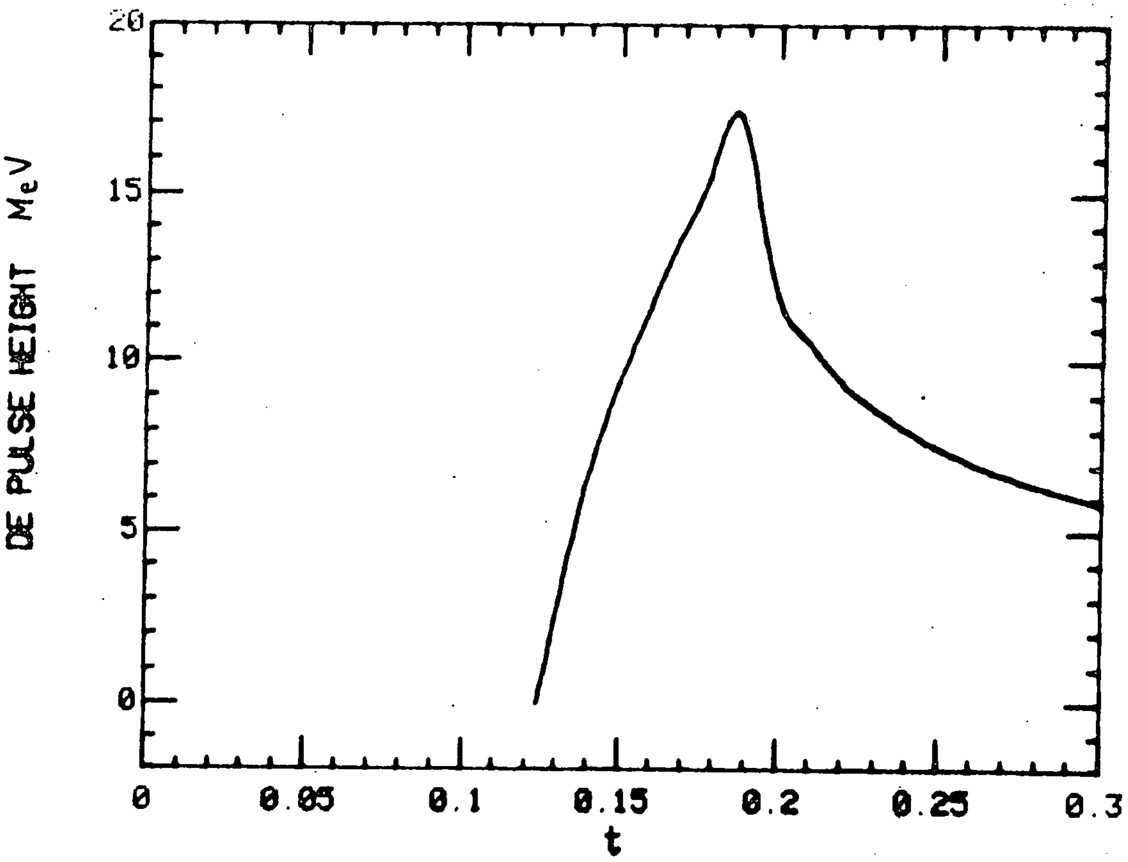

Figure 44: Energy Loss of Double Scattering Events

d) The Multiple Scattering Theory allows us to calculate the ratio of elastic deuteron scattering to breakup scattering. Figure 19 shows this ratio. At t=.2, the ratio is 1:10. Clearly we would need an excellent separation system to pick out the deuterons from this dominating 'background' of protons. If 5% of the proton signal were leaked by resolution and Fermi broadening into the deuteron signal, the deuterons would be 50% contaminated by protons. Our resolution is not this good.

e) More damning is the fact that at t=.2, the breakup single-double interference and double scattering terms are the same order of magnitude as the elastic scattering terms. Figure 44 shows that recoil protons from these events will look very much like deuterons.

In conclusion, we are left with only a band .12 < t < .16 for which deuterons can be separated from protons. Because of this, measurement of the deuteron elastic differential cross-section was not pursued.

B.6 EXTRACTION OF A NEUTRON CROSS-SECTION USING RECOIL DATA

The idea behind extracting a neutron cross-section using recoil particle information comes from the spectator approximation for deuteron scattering. If it is the neutron that interacts with the incident particle, only the neutron should have recoil kinetic energy after the collision. We then look for events with no charged particles in the recoil hodoscope. The failure of this program is the failure of the spectator approximation. The absence of a charged recoil particle can also mean a proton was struck but, due to the Fermi momentum at the time of impact, the recoil momentum

a) is too small to escape the target and surrounding material

or

b) is directed outside the recoil detector acceptance.

The fact that a charged recoil particle was seen in the detector need not mean that a neutron was <u>not</u> struck. It could also mean that

a) a proton spectator had sufficiently high Fermi momentum in the direction of the recoil detectors

or

b) a double scattering tock place.

In principle these corrections to the data could be made in the context of the Multiple Scattering Theory described earlier. In fact they are quite difficult. The closure relation [sum over all possible final recoil states] can no longer be applied because of the finite ranges of recoil kinetic energy and angular acceptance (which are also mutually dependent) over which cross-section and corrections are made[3]. It was decided that a complex Monte Carlo calculation to determine these corrections was not warranted. The only advantage of extracting the neutron cross-section from an event sample of 'neutron recoils' compared to extracting it from a sample ignoring the recoil state and using the elastic-plus-breakup formulations of the multiple scattering theory, was that half the events of the latter contain only proton cross-section information. The enrichment of neutron infor-

---

[3] The other side of the coin has been studied by Braun 1974 who looked at events <u>with</u> 'charged recoils' in a deuterium bubble chamber. Their problem was to make sure the charged recoil was indeed a spectator and not a recoiling proton. They had, however, complete angular acceptance.

mation in the former was not compensated by the uncertainty and effort in the corrections.

Appendix C

Tables of Cross-sections

π^+

t	σ_n	"Y_n"	"δY_n"	σ_D	Y_D	δY_D	σ_P	Y_P	δY_P
0.0582	13.425	20.388	2.0026	29.979	32.003	1.7086	13.708	13.738	1.0446
0.0683	12.266	16.921	1.1985	26.725	28.187	1.0358	12.652	13.106	0.60300
0.0796	11.087	14.725	0.97230	23.666	23.905	0.84910	11.576	10.760	0.47370
0.0920	9.9239	10.326	0.90502	20.815	20.186	0.76390	10.466	11.251	0.48530
0.0999	9.2473	11.749	1.1884	19.226	19.124	0.96070	9.8684	8.6520	0.69950
0.1055	8.7957	10.698	0.83412	18.202	18.296	0.71990	9.3722	8.8130	0.42130
0.1129	8.2327	7.8608	0.68869	16.937	16.503	0.52510	8.8726	9.7790	0.44560
0.1204	7.6988	8.9187	0.77729	15.771	15.972	0.66350	8.3532	8.1170	0.40490
0.1272	7.2447	7.6655	0.56380	14.790	15.018	0.44010	7.9268	8.3560	0.35240
0.1364	6.6727	6.6722	0.69314	13.580	12.704	0.58460	7.4096	6.9540	0.37240
0.1430	6.2904	6.7858	0.51859	12.779	13.150	0.40420	6.9869	7.2420	0.32490
0.1517	5.8197	5.9435	0.72741	11.807	11.961	0.61230	6.5362	6.0650	0.55700
0.1528	5.7628	6.8892	1.2104	11.689	12.145	1.0746	6.5362	6.8330	0.39270
0.1599	5.4084	5.0152	0.47198	10.964	10.730	0.35840	6.0952	6.4750	0.30710
0.1675	5.0531	4.6900	1.0339	10.243	10.785	0.86970	5.7247	6.8120	0.55900
0.1689	4.9903	4.6660	0.58181	10.115	9.0930	0.47910	5.6975	5.1300	0.33010
0.1779	4.6045	4.3777	0.43455	9.3385	9.2800	0.33130	5.3046	5.5590	0.28120
0.1862	4.2752	4.3407	0.50330	8.6782	8.5300	0.41240	4.9467	4.8030	0.28850
0.1964	3.9026	3.5592	0.38407	7.9364	7.4190	0.29250	4.5728	4.4230	0.24890
0.2055	3.5977	4.4248	0.47206	7.3300	7.9130	0.38950	4.2541	4.0160	0.26670
0.2163	3.2666	3.0248	0.38535	6.6753	6.6160	0.29110	3.9139	4.0720	0.25250
0.2251	3.0195	4.0012	0.42298	6.1862	6.8900	0.35420	3.6325	3.3400	0.23120
0.2347	2.7712	3.0870	0.52537	5.6965	6.2300	0.40750	3.3982	3.5600	0.33160
0.2461	2.5027	2.7878	0.37964	5.1660	5.3130	0.30630	3.0845	2.9040	0.22430
0.2679	2.0595	1.9628	0.34175	4.2897	4.2840	0.26930	2.5759	2.6380	0.21040
0.2909	1.6768	1.1531	0.33150	3.5299	3.3100	0.25060	2.1804	2.4180	0.21700
0.3132	1.3737	1.6846	0.42282	2.9243	3.2260	0.32630	1.8136	1.7620	0.26890

π^-

t	σ_n	"Y_n"	"δY_n"	σ_0	Y_0	δY_0	σ_p	Y_p	δY_p
0.0500	13.744	17.503	4.1931	34.478	34.348	3.5604	16.697	16.491	2.2149
0.0581	12.856	13.772	1.5266	31.288	29.721	1.2745	15.507	15.636	0.84040
0.0682	11.828	13.504	1.0857	27.922	28.658	0.92940	14.246	14.646	0.56120
0.0797	10.757	12.042	0.89241	24.703	25.292	0.77280	12.935	12.765	0.44630
0.0882	10.029	10.140	2.3052	22.622	23.268	1.9013	11.983	12.676	1.3035
0.0922	9.7034	9.6972	0.80549	21.735	21.791	0.68690	11.617	11.695	0.42070
0.0995	9.1363	8.6879	0.84109	20.210	20.426	0.68440	10.935	11.360	0.48890
0.1059	8.6664	9.0004	0.75227	18.995	19.896	0.64340	10.380	10.482	0.38980
0.1127	8.1936	8.1428	0.55786	17.790	18.053	0.45660	9.7879	9.5700	0.32050
0.1208	7.6640	7.3080	0.66904	16.484	16.558	0.56970	9.1673	8.9540	0.35080
0.1273	7.2638	6.6385	0.45995	15.512	15.473	0.37090	8.6585	8.5710	0.27200
0.1359	6.7663	5.8050	0.61279	14.332	14.135	0.51160	8.0350	8.1090	0.33730
0.1389	6.6009	6.4512	2.0177	13.943	13.364	1.6454	7.8351	6.7210	1.1678
0.1431	6.3761	4.8084	0.41567	13.421	12.897	0.32670	7.5700	7.9250	0.25700
0.1521	5.9198	5.5259	0.60820	12.375	12.554	0.51490	7.0366	6.8150	0.32370
0.1532	5.8664	4.2789	0.67943	12.253	11.328	0.53500	7.0248	6.9380	0.41880
0.1599	5.5509	4.8407	0.37714	11.541	11.413	0.30260	6.5684	6.4030	0.22510
0.1682	5.1835	3.8859	0.74336	10.721	10.215	0.61640	6.1520	6.2160	0.41550
0.1688	5.1579	4.7639	0.42451	10.664	10.441	0.34780	6.1314	5.5300	0.24340
0.1781	4.7770	3.9408	0.34830	9.8262	9.8060	0.27650	5.6755	5.7270	0.21180
0.1839	4.5538	7.0369	1.9023	9.3393	13.426	1.6624	5.4012	5.9450	0.92470
0.1862	4.4682	3.8147	0.35397	9.1530	9.2230	0.28590	5.2668	5.2740	0.20870
0.1965	4.1042	3.2169	0.32282	8.3693	8.4240	0.25380	4.8385	5.0950	0.19950
0.2055	3.8105	3.3297	0.31981	7.7413	7.9500	0.25770	4.5014	4.5010	0.18940
0.2153	3.5146	2.8124	0.32737	7.1157	7.0380	0.25580	4.1424	4.1420	0.20430
0.2256	3.2283	2.2331	0.28669	6.5136	6.3590	0.22410	3.7864	4.0680	0.17880
0.2347	2.9948	2.9176	0.43802	6.0271	6.2970	0.34800	3.5019	3.2820	0.26600
0.2471	2.7036	2.2601	0.25750	5.4231	5.5360	0.20570	3.1689	3.2040	0.15490
0.2687	2.2623	2.0316	0.23224	4.5162	4.6670	0.18590	2.6477	2.5720	0.13920
0.2916	1.8728	1.3978	0.22363	3.7236	3.6840	0.17510	2.1937	2.2530	0.13910
0.3133	1.5659	1.3040	0.27749	3.1032	3.0930	0.21720	1.8160	1.7580	0.17270

PROTONS

t	σ_n	"Y_n"	"δY_n"	σ_D	Y_D	δY_D	σ_H	Y_H	δY_H
0.0582	33.697	46.634	4.8668	77.234	79.292	4.0171	38.356	41.003	2.7475
0.0682	30.477	41.498	2.8725	67.888	69.335	2.4526	35.029	35.028	1.4954
0.0793	27.262	33.523	2.3910	59.245	59.224	2.0353	31.469	31.968	1.2547
0.0921	23.973	27.861	2.1517	50.910	49.738	1.8232	27.784	27.283	1.1427
0.1002	22.100	20.171	3.1286	46.371	42.849	2.2599	25.794	27.634	2.1636
0.1058	20.891	25.286	2.0703	43.539	46.237	1.7511	24.272	25.651	1.1044
0.1127	19.493	22.641	1.6246	40.296	38.023	1.2453	22.729	19.729	1.0434
0.1201	18.096	19.562	1.8311	37.152	37.296	1.5315	21.101	21.789	1.0037
0.1272	16.851	18.591	1.3852	34.380	34.278	1.0365	19.837	19.464	0.91900
0.1358	15.456	16.554	1.7144	31.345	32.687	1.4265	18.221	19.613	0.95100
0.1432	14.349	16.108	1.2340	28.965	28.684	0.92900	16.998	15.807	0.81230
0.1516	13.188	15.411	1.6676	26.505	27.762	1.4160	15.538	15.338	0.88090
0.1529	13.017	12.460	3.8099	26.144	25.550	3.2604	15.463	16.031	1.9711
0.1600	12.121	13.144	1.1234	24.270	24.030	0.83860	14.397	13.636	0.74750
0.1679	11.197	14.998	2.4281	22.352	27.252	2.0906	13.443	14.824	1.2350
0.1685	11.130	13.012	1.8790	22.213	23.185	1.5795	13.263	12.713	1.0177
0.1776	10.157	9.3056	1.0522	20.218	20.059	0.75750	12.206	13.076	0.73030
0.1861	9.3263	11.185	1.4655	18.524	19.490	1.2073	11.169	10.452	0.83070
0.1961	8.4351	8.1264	0.94915	16.725	16.694	0.68510	10.160	10.515	0.65690
0.2048	7.7294	9.1590	1.3929	15.306	17.345	1.1310	9.3871	9.9870	0.81310
0.2154	6.9488	4.7330	0.88648	13.749	12.162	0.61360	8.4088	9.0400	0.63980
0.2242	6.3610	6.2462	1.0952	12.578	11.341	0.89240	7.7538	6.5790	0.63490
0.2341	5.7589	4.6228	1.2579	11.388	11.766	0.88480	6.9996	8.4970	0.89410
0.2466	5.0795	6.2412	1.0963	10.046	11.272	0.90510	6.1979	6.2370	0.61860
0.2682	4.0889	5.6165	0.92956	8.0981	8.9460	0.77880	5.1245	4.3080	0.50750
0.2910	3.2520	1.4962	0.90945	6.4580	6.0790	0.64880	4.1359	5.3590	0.63730

π^- (full Range)

t	σ_n	"Y_n"	"δY_n"	σ_D	Y_D	δY_D	σ_P	Y_P	δY_P
0.0431	13.324	14.227	1.2017	36.728	36.858	0.96760	18.027	18.744	0.71270
0.0500	12.680	14.008	4.1931	33.713	34.348	3.5604	17.097	16.491	2.2149
0.0526	12.445	14.398	1.1119	32.682	33.212	0.90760	16.577	15.039	0.64240
0.0581	11.964	10.769	1.5266	30.655	29.721	1.2745	15.819	15.636	0.84040
0.0630	11.550	11.516	1.0435	29.017	29.214	0.84240	15.149	14.309	0.61580
0.0682	11.127	10.627	1.0857	27.423	28.658	0.92940	14.469	14.646	0.56120
0.0740	10.673	10.388	0.99415	25.801	26.747	0.80030	13.746	13.174	0.58980
0.0797	10.245	9.5060	0.89241	24.329	25.292	0.77280	13.071	12.765	0.44630
0.0864	9.7639	8.4098	0.90663	22.730	22.234	0.72120	12.299	11.224	0.54940
0.0882	9.6386	7.8342	2.3052	22.325	23.268	1.9013	12.062	12.676	1.3035
0.0922	9.3657	7.5292	0.80549	21.470	21.791	0.68690	11.674	11.695	0.42070
0.0995	8.8875	6.6724	0.84109	20.000	20.426	0.68440	10.955	11.360	0.48890
0.1059	8.4884	7.0249	0.75227	18.827	19.896	0.64340	10.371	10.482	0.38980
0.1127	8.0840	6.3486	0.55786	17.662	18.053	0.45660	9.7497	9.5700	0.32050
0.1208	7.6273	5.6676	0.66904	16.399	16.558	0.56970	9.1007	8.9540	0.35080
0.1273	7.2795	5.1126	0.45995	15.458	15.473	0.37090	8.5702	8.5710	0.27200
0.1359	6.8437	4.4222	0.61279	14.315	14.135	0.51160	7.9224	8.1090	0.33730
0.1389	6.6979	5.1121	2.0177	13.937	13.364	1.6454	7.7153	6.7210	1.1678
0.1431	6.4989	3.5725	0.41567	13.430	12.897	0.32670	7.4409	7.9250	0.25700
0.1521	6.0923	4.2874	0.60820	12.413	12.554	0.51490	6.8906	6.8150	0.32370
0.1532	6.0444	3.1889	0.67943	12.295	11.328	0.53500	6.8785	6.9380	0.41880
0.1599	5.7605	3.7209	0.37714	11.602	11.413	0.30260	6.4093	6.4030	0.22510
0.1682	5.4273	2.9049	0.74336	10.802	10.215	0.61640	5.9826	6.2160	0.41550
0.1688	5.4040	3.7288	0.42451	10.747	10.441	0.34780	5.9616	5.5300	0.24340
0.1781	5.0550	2.9912	0.34830	9.9288	9.8060	0.27650	5.4963	5.7270	0.21180
0.1839	4.8488	5.7251	1.9023	9.4527	13.426	1.6624	5.2173	5.9450	0.92470
0.1862	4.7694	2.9180	0.35397	9.2704	9.2230	0.28590	5.0809	5.2740	0.20870
0.1965	4.4294	2.4129	0.32282	8.5027	8.4240	0.25380	4.6473	5.0950	0.19950
0.2055	4.1523	2.5579	0.31981	7.8862	7.9500	0.25770	4.3074	4.5010	0.18940
0.2153	3.8702	2.1354	0.32737	7.2710	7.0380	0.25580	3.9468	4.1420	0.20430
0.2256	3.5943	1.6412	0.28669	6.6776	6.3590	0.22410	3.5909	4.0680	0.17880
0.2347	3.3670	2.3008	0.43802	6.1971	6.2970	0.34800	3.3078	3.2820	0.26600
0.2471	3.0803	1.7291	0.25750	5.5991	5.5360	0.20570	2.9778	3.2040	0.15490
0.2687	2.6378	1.5810	0.23224	4.6974	4.6670	0.18590	2.4650	2.5720	0.13920
0.2916	2.2379	1.0531	0.22363	3.9050	3.6840	0.17510	2.0226	2.2530	0.13910
0.2920	2.2315	1.4756	0.31493	3.8925	3.6890	0.26910	1.9907	1.8140	0.16360
0.3133	1.9151	1.0097	0.27749	3.2810	3.0930	0.21720	1.6581	1.7580	0.17270
0.3137	1.9096	1.5600	0.18948	3.2705	3.2700	0.16520	1.6334	1.3530	0.92800E-01
0.3379	1.6050	1.2914	0.15039	2.6960	2.7150	0.13070	1.3203	1.1270	0.74400E-01
0.3635	1.3356	1.0996	0.13828	2.1999	2.4410	0.11890	1.0475	1.0600	0.70600E-01
0.3895	1.1082	1.1205	0.11588	1.7910	1.9140	0.10410	0.86410	0.59700	0.50900E-01
0.4170	0.90963	0.55333	0.11111	1.4422	1.5710	0.93000E-01	0.66415	0.83900	0.60800E-01
0.4454	0.74185	0.56790	0.93390E-01	1.1540	1.1940	0.81500E-01	0.50913	0.49500	0.45600E-01
0.4737	0.60546	0.35238	0.95438E-01	0.92483	0.98400	0.79100E-01	0.39794	0.52100	0.53400E-01
0.5024	0.49272	0.26229	0.12118	0.73900	0.80700	0.95500E-01	0.30939	0.45400	0.74600E-01

BIBLIOGRAPHY

Akimov 1975, Y. Akimov et al., Proton-Deuteron Elastic Scattering at Small Momentum Transfer from 50 to 400 GeV/c, Phys. Rev. D12, 3399 (1975), D15, 2040 (1977)

Alberi 1969, G. Alberi and L. Bertocchi, Nuovo Cimento 63A, 285 (1969)

Alberi 1975, G. Alberi, L.P. Rosa and Z.D. Thome, Comment on Double-Scattering Effect in Deuteron Breakup Reactions, Phys. Rev. Let. 34, 503 (1975)

Allaby 1969, J.V. Allaby et al., On the Separation of Single and Double Scattering in Proton-Deuteron Collisions at 19.2 GeV/c, Phys. Let. B30, 549 (1969)

Amaldi 1972, U. Amaldi et al., Study of Elastic Proton-Neutron Scattering by Means of Proton-Deuteron Scattering at 24 GeV/c, Nuc. Phys. B39, 39 (1972)

Anderson 1976, R. Anderson and J. Grant, A Design of a Differential Cerenkov Counter for Use at High Momentum, Nucl. Instrum. Methods, 134 (1976)

Anelli 1971, E.F. Anelli et al., Multi-wire Proportional Chambers and Computer Interface Design, Bari Univ. 1971 (unpublished)

Atwood 1973, W.B. Atwood and G.B. West, Extraction of Asymptotic Nucleon Cross Sections from Deuterium Data, Phys. Rev. D7, 773 (1973)

Ayres 1974, D. Ayres, Single Arm Spectrometer Facility Threshold Cerenkov Counter Operating Instructions, Argonne National Laboratory Report, 1974 (unpublished)

Bartenev 1973, V. Bartenev et al., Real Part of the Proton-Proton Forward-Scattering Amplitude from 50 to 400 GeV, Phys. Rev. Let. 31, 1367 (1973)

Bellettini 1965, G. Bellettini et al., The Real Part of the Proton-Neutron Scattering Amplitude at 19.3 GeV/c, Phys. Let. 19, 341 (1965)

Benot 1972, M. Benot, J. Litt, and R. Meunier, Nucl. Instrum. Methods 105, 431 (1972)

Bertocchi 1967, L. Bertocchi, *Coherent Break up of the Deuteron*, Nuovo Cimento 50A, 1015 (1967)

Bodek 1973, A. Bodek, *Comment on the Extraction of Nucleon Cross Sections from Deuterium Data*, Phys. Rev. D8, 2331 (1973)

Bouquet 1976, A. Bouquet et al., *Problems in the Phenomenological Analysis of Cross-Section Differences...*, Nuovo Cimento A31, 411 (1976)

Bradamante 1970, F. Bradamante et al., *Pion-Deuteron Coherent Scattering at High-Energy*, Phys. Let. B31, 87 (1970)

Bradamante 1970, F. Bradamante et al., *Elastic Scattering of Protons on Deuterons at High Energy*, Phys. Let. B32, 303 (1970)

Bradamante 1971, F. Bradamante et al., *On the Separation of the Elastic Component in Double-Scattering, Collisions of High-Energy Hadrons in Deuterium* Nuc. Phys. B28, 349 (1971)

Bradamante 1971, F. Bradamante et al., *On the Comparison of High-Energy Hadron-Deuteron Scattering Data with the Glauber Model*, Nuc. Phys. B33, 165 (1971)

Braun 1974, H. Braun et al., *Study of the $\bar{p}d$->$\bar{p}pn$ and $\bar{p}n$->$\bar{p}n$ reactions at 5.55 GeV/c*, Phys. Rev. D10, 3573 (1974)

Brown 1972, K.L. Brown, *A First and Second Order Matrix Theory for the Design of Beam Transport Systems and Charged Particle Spectrometers*, Stanford Linear Accelerator Center SLAC Report 75 (unpublished)

Brown 1975, K.L. Brown and S.K. Howry, *Transport/360, A Program for the Design of Static Magnetic Beam Transport Systems*, Stanford Linear Accelerator Center SLAC Report 91 (unpublished)

Butler 1975, J.N. Butler, *Elastic Scattering of Positive Pions, Kaons, and Protons from 50 to 175 GeV/c*, Ph.D thesis, Mass. Inst. of Technology (unpublished 1975)

Carey 1971, D.C. Carey, *TURTLE, computer program for simulating charged Particle Beam Transport Systems*, FNAL Report NAL-64, December 1971

Dean 1971, Nathan W. Dean, *Explanation of Excess High-Momentum Spectators in High-Energy Deuteron-Breakup Reactions*, Phys. Rev. Let. 27, 276 (1971)

Eadie 1971 W.T. Eadie et al., *Statistical Methods in Experimental Physics*, North Holland Pub. Co., 1971

Foley 1969, K.J. Foley et al., Experimental Test of Pion-Nucleon Forward Dispersion Relations at High Energies, Phys. Rev. 181, 1775 (1969)

Franco 1966, V. Franco and R.J. Glauber, High-Energy Deuteron Cross Sections Phys. Rev. 142, 1195 (1966)

Franco 1969, V. Franco and R. J. Glauber, Effect of Quadrupole Deformation on High-Energy Scattering by Deuterons, Phys. Rev. Let. 22, 370 (1969)

Franco 1971, V. Franco, Effects of the Coulomb Field on Scattering by Deuterium, Phys. Rev. Let. 27, 1541 (1971)

Franco 1974, V. Franco and G. K. Varma, Hadron-Neutron Forward Elastic Scattering Amplitude and Hadron-Deuteron Collisions, Phys. Rev. Let. 33, 44 (1974)

Franco 1975, V. Franco and G. K. Varma, Coulomb effects in hadron-nucleus and nucleus-nucleus collisions and the hadron-neutron amplitude, Phys. Rev. C12, 225 (1975)

Franco 1977, V. Franco Extracting Hadron-Neutron Scattering Amplitudes from Hadron-Proton and Hadron-Deuteron Measurements, Phys. Rev. Let. 38, 188 (1977)

Fridman 1974, A. Fridman, The Deuteron as Target in High Energy Reactions, Inst. Nat. de Phys. Nucl et de Phys. de Particules CNR/HE 74-4 (1974)

Glauber 1955, R.J. Glauber, Cross Sections in Deuterium at High Energies, Phys. Rev. 100, 242 (1955)

Glauber 1959, R.J. Glauber, in Lectures in Theoretical Physics, edited by W. E. Brittin, et al., (Interscience Publishers Inc 1959) Vol. I, p 315

Glauber 1967, R.J. Glauber and V. Franco, High-Energy Deuteron Cross Sections: Charge-Exchange Effects, Phys. Rev. 156, 1685 (1967)

Glauber 1971, R.J. Glauber, B. Margolis, O. Kofoed-Hansen, On Momentum-Loss Spctra in Proton Scattering on Deuterium, Nuc. Phys. B30, 220 (1971)

Gottschalk 1974, B. Gottschalk, The Recoil Detector of the FNAL SAS Facility, SLAC Technical Note TN-74-15

Greben 1970, J.M. Greben, Elastic Electron Deuteron Scattering and the Deuteron Wave Function, Intern Rapport 97, 1970, Inst. for Theoretical Physics, U. of Groningen, The Netherlands

Harrington 1964, D.R. Harrington, Double Scattering Corrections to High-Energy Diffraction Scattering from Deuterons, Phys. Rev. 135, 358 (1964)

Hulthen 1957, L. Hulthen and M. Sugawara, Handbuch der Physik, ed. by S. Flugge (Springer Verlag 1957) Vol. 39, p. 1

Kofoed-Hansen 1972, O. Kofoed-Hansen, Glauber Theory Interpretation of Proton-Deuteron Scattering Data at 24 GeV/c, Nuc. Phys. B39, 61 (1972)

Kolybasov 1973, V.M. Kolybasov and M.S. Marinov (Inst. of Theoretical and Experimental Physics, Moscow), Interaction of High-Energy Particles with Deuterons, Usp. Fiz. Nauk 109, 137 (1973), in Sov. Phys.-Usp., 16, 53

Landshoff 1977, P.V. Landshoff and J.C. Polkinghorne, Fermi-Motion Corrections for Deuterium Targets, Dept. of App. Math. and Theo. Phys., U. of Cambridge, Jan. 1977 (preprint)

Litt 1973, J. Litt and R. Meunier, Cerenkov Counter Technique in High-Energy Physics, Annual Rev. of Nuc. Sci. (1973)

Massimo 1972, J.T. Massimo, B. Nelson, L.J. Levinson, SPEX General Structure, SPEX Programmers' Guide, and SPEX Users' Guide, Brown U. High Energy Group Internal Reports 123,124,125 (1972)

Massimo 1975, J.T. Massimo, L.J. Levinson, et al., Bull. Am Phys. Soc. 20, 593 (1975)

Michael 1969 C. Michael and C. Wilkin, Nuc. Phys. B11, 99 (1969)

Rich 1954, M. Rich and R. Madey, Range-Energy Tables, U. of Cal. Rad. Lab., Report UCRL-2301 (1954)

SAS Group 1977, D.S. Ayres et al., Pi±p, K±p, pp, and $p\bar{p}$ Elastic Scattering from 50 to 175 GeV/c, Phys. Rev. D15, 3105 (1977)

Sidhu 1973, D.P. Sidhu and C. Quigg, Pion-Deuteron Scattering at High Energies, Phys. Rev. D7, 755 (1973)

Sogard 1974, M. Sogard, Deuterium Memo, FNAL Expt 96 internal memo (unpublished), 1974

Sogard 1974, M. Sogard and A. Weitsch, An Absolute Bdl Calibration of B2 Magnets for the AVB System of the Single Arm Spectrometer Facility, Fermilab Report TM-517, 1974 (unpublished)

Straumann 1970, N. Straumann and C. Wilkin, Proton-Neutron Scattering, Phys. Rev. Let. 24, 479 (1970)

West 1968, G.B. West and D.R. Yennie, Coulomb Interference in High-Energy Scattering, Phys. Rev. 172, 1413 (1968)

West 1974, G. B. West, The Doppler Effect in the Extraction of Total Neutron Cross Sections from Deuterium Data with Particular Emphasis on Asymptotic Hadron and Deep Inelastic Electron Scattering, Annals of Physics 74, 464 (1972)

Wilkin 1966, C. Wilkin, Charge Independence in High-Energy Scattering from Deuterons, Phys. Rev. Let. 17, 561 (1966)